

**CONTINUOUS PRODUCTION AND IMPROVED STABILITIES OF
LUMINESCENT COLLOIDAL PEROVSKITE NANOCRYSTALS AS
NEXT-GENERATION EMITTERS**

A Dissertation
Presented to
The Academic Faculty

by

Gill Biesold

In Partial Fulfillment
of the Requirements for the Degree
Doctor of Philosophy in the
School of Materials Science and Engineering

Georgia Institute of Technology
August 2022

COPYRIGHT © 2022 BY GILL BIESOLD

**CONTINUOUS PRODUCTION AND IMPROVED STABILITIES OF
LUMINESCENT COLLOIDAL PEROVSKITE NANOCRYSTALS AS NEXT-
GENERATION EMITTERS**

Approved by:

Dr. Zhiqun Lin, Advisor
School of Materials Science and
Engineering
Georgia Institute of Technology

Dr. Juan Pablo Correa-Baena
School of Materials Science and
Engineering
Georgia Institute of Technology

Dr. Vladimir Tsukruk
School of Materials Science and
Engineering
Georgia Institute of Technology

Dr. Zhitao Kang
Georgia Tech Research Institute
Georgia Institute of Technology

Dr. Naresh Thadhani
School of Materials Science and
Engineering
Georgia Institute of Technology

Date Approved: June 17, 2022

I can't give you guts. And I can't give you heart. And tonight, hey, it was B.Y.O.G.

Bring your own guts.

- Dabo Swinney

To all those who show up big

ACKNOWLEDGEMENTS

I would first like to thank my wife Nicole Biesold for her limitless support as I worked my way through my studies. Being the spouse of a graduate student has its challenges and I am forever grateful that she empowered me to explore my curiosities to the fullest. I also want to thank my advisor Dr. Zhiqun Lin for his support, generosity, and kindness. He accepted me into his group with no experience in colloidal synthesis and was patient as I found my way. He has been an exemplary mentor throughout the entirety of my studies and is the model of what a scientist with unending curiosity should be. I would also like to thank my dissertation committee, Prof. Vladimir Tsukruk, Prof. Naresh Thadhani, Prof. Zhitao Kang, and Prof. Jose Correa-Baena. I sincerely appreciate all of the time that they have invested in me, my proposal, and my dissertation. Their feedback has been crucial to improving my thesis to the best it can be.

I also want to thank my tribe in Seattle for their continued support throughout all of the endeavors of my life. Whether it be packing the stands for a high school football game or waking up to watch my proposal at 6:00am, you have all offered me all the support and strength I could ever need. Particularly, I would like to thank Bruce and Phyllis Biesold, Terry and Dorene McTigue, and Paul and Gloria Sauro. They in particular have been instrumental at every step of my life. I would also be remiss not to mention the love and support of my parents, Elisa McGee and Todd Biesold. Thank you for encouraging me to chase my passions, even if it meant moving across the country. You both still might not know what a quantum dot is, but your support has never wavered.

I would also like to thank all the current members of the Nanostructured Functional Materials Lab, including: Shuang Liang, Mingyue Zhang, Christopher Sewell, Woosung Choi, Rachel Lawless, Shiqi Wei, and Jinyoung Choi for their assistance in research and the camaraderie in the offices. I specifically would like to acknowledge my lab mate, co-author, and friend Shuang Liang for all his contributions to my research and for keeping me sane throughout our studies. We came into the group at the same time and we are defending on the same day. Thanks for being such a great friend. Finally, I would like to thank my former group mate and mentor Dr. Young Joon Yoon. It was under his expert guidance that I learned colloidal synthesis. His precision and patience are two of the attributes that I admire and emulate most.

TABLE OF CONTENTS

ACKNOWLEDGEMENTS	v
LIST OF TABLES	x
LIST OF FIGURES	xi
LIST OF SYMBOLS AND ABBREVIATIONS	xviii
SUMMARY	xx
Chapter 1. Introduction	1
1.1 Lead Halide Perovskite	2
1.1.1 Variations of Perovskite Crystal Structures	2
1.1.2 Perovskite Nanocrystals	4
1.2 Benefits of Lead Halide Perovskite Nanocrystals	5
1.2.1 Optical Properties	5
1.2.2 Excellent Charge Carrier Dynamics	6
1.2.3 Defect Tolerance	8
1.2.4 Facile Synthesis	10
1.3 Limitations of Lead Halide Perovskite Nanocrystals	12
1.3.1 Polar Solvent and Moisture Sensitivity	12
1.3.2 Photo Instability	12
1.3.3 Thermal Instability	13
1.3.4 Colloidal Instability	14

1.3.5	Reliance on Batch Synthesis Methods	14
1.4	Employing Polymers to Enhance the Properties of Perovskite	15
1.4.1	Linear Block Copolymer Ligands	17
1.4.2	Polymer Nanoreactors	19
1.5	Conclusion	22
CHAPTER 2.	Motivation and Research Goal	24
2.1	Motivation	24
2.2	Research Objectives	26
CHAPTER 3.	Continuous Production of Highly Stable Perovskite Nanocrystals via a Dual Reactor Approach	27
3.1	Introduction	27
3.2	Experimental Details	30
3.2.1	Materials	30
3.2.2	Methods	31
3.3	Results and Discussion	39
3.4	Conclusion	55
CHAPTER 4.	Continuous Production of Ultrathin Organic-Inorganic Ruddlesden-Popper Perovskite Nanoplatelets via a Flow Reactor	57
4.1	Introduction	57
4.2	Experimental Details	61
4.2.1	Materials	61
4.2.2	Methods	62

4.3	Results and Discussion	68
4.4	Conclusion	97
CHAPTER 5. Enhancing the Stability of Ruddlesden-Popper Perovskite via Engineering Alkylammonium Cation		99
5.1	Introduction	99
5.2	Experimental Details	103
5.2.1	Materials	103
5.2.2	Methods	104
5.3	Results and Discussion	106
5.4	Conclusion	123
CHAPTER 6. General Conclusions and Future Research		124
6.1	General Conclusions	124
6.2	Future Research	129
Dissemination of the Work		133
REFERENCES		137

LIST OF TABLES

Table 1 – Reynolds number corresponding to each flowrate in flow reactor	36
Table 2 - Optical properties of CsPbBr ₃ PNCs synthesized via conventional LARP using various antisolvents.....	44
Table 3 – Reynolds number corresponding to various antisolvent injection rates	68
Table 4 – Structure and PLQY of NPLs made with different alkylammonium cations .	108
Table 5 – Summary of optical Properties of NPLs made with perfluorinated cations ...	120

LIST OF FIGURES

Figure 1 - (a) Schematic diagram of ABX_3 perovskite structure. (b) Schematic of $n=1$ Ruddlesden-Popper phase perovskite. Note that while the L cations in the diagram are linear, they can have a variety of diverse architectures.	2
Figure 2 - Chemical structures of various alkylammonium cations that have been used in RP perovskites	4
Figure 3 - (a) photograph of $CsPbX_3$ NCs under UV excitation (b) Photoluminescence spectra of $CsPbX_3$ PNCs, and (c) Absorbance and emission spectra of $CsPbX_3$ PNCs with various halide compositions (X ranging from purely Cl to Br to I) ⁴⁴	6
Figure 4 - (a) Illustration of material with band structure intolerant to defects (left) and ideal band structure of material with optimal defect tolerance. (b) Band structure of $CsPbI_3$ perovskite ⁵⁹	9
Figure 5 - Representative illustration of necessary equipment for (a) LARP ⁶⁸ and (b) hot injection ⁶⁹ PNC synthesis methods.....	11
Figure 6 - Synthetic strategy for perovskite NCs using linear amphiphilic block copolymer micelles as nanoreactors. ¹²⁰	19
Figure 7 - a) Stepwise representation of crafting “hairy” all-inorganic perovskite $CsPbBr_3$ QDs with intimately and permanently capped by PS chains via capitalizing on amphiphilic star-like PAA- <i>b</i> -PS diblock copolymers as nanoreactors. b) TEM image of PS-capped $CsPbBr_3$ QDs with diameter= 10.1 ± 0.6 nm. ¹¹³ c) Stepwise representation of the synthetic route to PS-capped $MAPbBr_3/SiO_2$ core/shell NCs and PEO-capped $MAPbBr_3/SiO_2$ core/shell NCs by exploiting star-like P4VP- <i>b</i> -PtBA- <i>b</i> -PS and P4VP- <i>b</i> -PtBA- <i>b</i> -PEO as nanoreactors, respectively. d) TEM images of PEO-capped	

MAPbBr ₃ /SiO ₂ core/shell NCs with MAPbBr ₃ core diameter of 6.1 ± 0.3 nm and SiO ₂ shell thickness of 8.9 ± 0.4 nm (top), and MAPbBr ₃ core diameter of 6.8 ± 0.3 nm and SiO ₂ shell thickness of 8.0 ± 0.3 nm (bottom). ¹³¹	21
Figure 8 - Stepwise representation of route to star-like PAA- <i>b</i> -PS diblock copolymer nanoreactor and the resulting PS-capped CsPbBr ₃ nanocrystal.....	41
Figure 9 - NMR spectra from (a) brominated β -CD, (b) star-like PtBA, (c) star-like PtBA- <i>b</i> -PS, and (d) star-like PAA- <i>b</i> -PS.....	42
Figure 10 - GPC traces for star-like PtBA and PtBA- <i>b</i> -PS.	43
Figure 11 - Schematic diagram of dual flow/nano reactor apparatus.	45
Figure 12 - (a) Effect of $Q_{toluene}$ on PLQY and (b) emission peak position of PS-capped CsPbBr ₃ PNCs via capitalizing on star-like PAA- <i>b</i> -PS as nanoreactor and OA/OAm-co-capped CsPbBr ₃ PNCs (control sample).....	47
Figure 13 - Effect of $Q_{precursor}$ on (a) PLQY, (b) emission peak position, and (c) FWHM of PS-capped CsPbBr ₃ PNCs and OA/OAm-co-capped CsPbBr ₃ PNCs (control sample), where Q_{tol} was held constant at the optimized 5000 mL/hr.....	49
Figure 14 - TEM images of (a) PS-capped CsPbBr ₃ PNCs and (b) OA/OAm-co-capped CsPbBr ₃ PNCs (control sample). Both samples were synthesized at optimized conditions ($Q_{tol} = 5000$ mL/hr and $Q_{precursor} = 60$ mL/hr).....	51
Figure 15 - Size distribution of (a) PS-capped CsPbBr ₃ PNCs and (b) OA/OAm-co-capped CsPbBr ₃ PNCs (control sample). Both samples were synthesized at optimized conditions ($Q_{tol} = 5000$ mL/hr and $Q_{precursor} = 60$ mL/hr).	51

Figure 16 - (a) Colloidal, (b) UV, and (c) thermal (at 80 °C) stabilities of PS-capped and OA/OAm-co-capped CsPbBr₃ PNCs (control sample) synthesized at optimized conditions ($Q_{tol} = 5000$ mL/hr and $Q_{precursor} = 60$ mL/hr)..... 54

Figure 17 - Schematic of (a) three-dimensional ABX₃ perovskite crystal structure, and (b) typical n=1 L₂PbX₄ Ruddlesden-Popper perovskite structure. (c) Schematic of in-house built flow reactor, where precursor solution and antisolvent are introduced separately via respective syringe pumps..... 69

Figure 18 - (a-f) TEM images of (PEA)₂PbBr₄ nanoplatelets (NPLs) synthesized in the flow reactor with a reactor tube length of 15 cm, a toluene injection rate (Q_{tol}) held constant at 1200 mL/hr, and $Q_{precursor}$ ranging from 5-30 mL/hr, , that is, (a) 5 mL/hr, (b) 10 mL/hr, (c) 15 mL/hr, (d) 20 mL/hr, (e) 25 mL/hr, and (f) 30 mL/hr, respectively. All scale bars = 2 μm. Effects of antisolvent composition and $Q_{precursor}$ on (g) PLQY, (h) emission peak position, and (i) FWHM of emission of (PEA)₂PbBr₄ NPLs..... 73

Figure 19 - TEM images of (PEA)₂PbBr₄ NPLs produced in a 15cm reactor with chlorobenzene as the antisolvent at a constant flowrate of 1200 mL/hr and precursor injection rates ranging from 5-30 mL/hr, that is, (a) 5 mL/hr, (b) 10 mL/hr, (c) 15 mL/hr, (d) 20mL/hr, (e) 25 mL/hr, and (f) 30 mL/hr, respectively. All scale bars = 2 μm..... 74

Figure 20 - TEM images of (PEA)₂PbBr₄ NPLs made in a 15cm reactor with dichloromethane as the antisolvent at a constant flowrate of 1200 mL/hr and precursor injection rates ranging from 5-30 mL/hr, that is, (a) 5 mL/hr, (b) 10 mL/hr, (c) 15 mL/hr, (d) 20mL/hr, (e) 25 mL/hr, and (f) 30 mL/hr, respectively. All scale bars = 2 μm..... 74

Figure 21 - Nanoplatelet size distribution of (PEA)₂PbBr₄ NPLs made in 15cm reactor tube with $Q_{toluene} = 1200$ mL/hr at various $Q_{precursor}$ 75

Figure 22 - Average corner to corner length and deviation of (PEA) ₂ PbBr ₄ NPLs made in 15cm reactor tube with Q _{toluene} =1200 mL/hr at various Q _{precursor}	75
Figure 23 - Nanoplatelet size distribution of (PEA) ₂ PbBr ₄ NPLs made in 15cm reactor tube with Q _{chlorobenzene} =1200 mL/hr at various Q _{precursor}	76
Figure 24 - Average corner to corner length and deviation of (PEA) ₂ PbBr ₄ NPLs made in 15cm reactor tube with Q _{chlorobenzene} =1200 mL/hr at various Q _{precursor}	77
Figure 25 - UV-vis absorbance and PL emission of (PEA) ₂ PbBr ₄ NPLs produced in 15 cm reactor with 5 mL/hr precursor injection rate and 1200 mL/hr flow of (a) toluene, (b) chlorobenzene, and (c) dichloromethane antisolvent.....	77
Figure 26 - TEM images of (PEA) ₂ PbBr ₄ NPLs produced in the flow reactor with (a) 15 cm, (b) 30 cm, (c) 60 cm reactor tubes and 1200 mL/hr toluene and 5 mL/hr precursor solution injection rates. All scale bars = 2 μm. Effects of reactor tube length (from 15-60 cm) and precursor injection rates (from 5-30 mL/hr) on (d) emission peak position, (e) FWHM, (f) PLQY of (PEA) ₂ PbBr ₄ NPLs.....	80
Figure 27 - TEM images of (PEA) ₂ PbBr ₄ NPLs produced in a 30cm reactor with toluene as the antisolvent at a constant flowrate of 1200 mL/hr and precursor injection rates ranging from 5-30 mL/hr, that is, (a) 5 mL/hr, (b) 10 mL/hr, (c) 15 mL/hr, (d) 20mL/hr, (e) 25 mL/hr, and (f) 30 mL/hr, respectively. All scale bars = 2 μm.....	81
Figure 28 - TEM images of (PEA) ₂ PbBr ₄ NPLs produced in a 60cm reactor with toluene as the antisolvent at a constant flowrate of 1200 mL/hr and precursor injection rates ranging from 5-30 mL/hr, that is, (a) 5 mL/hr, (b) 10 mL/hr, (c) 15 mL/hr, (d) 20mL/hr, (e) 25 mL/hr, and (f) 30 mL/hr, respectively.....	81

Figure 29 - (a-e) TEM images of $(\text{PEA})_2\text{PbBr}_4$ NPLs synthesized in the flow reactor at varying toluene injection rates (from 514-1200 mL/hr) with a constant precursor injection rate of 5 mL/hr. All scale bars = 2 μm . The effect of Reynolds Number on (f) PLQY, (g) emission peak position, and (h) FWHM of $(\text{PEA})_2\text{PbBr}_4$ NPLs. 85

Figure 30 - Particle size distribution of $(\text{PEA})_2\text{PbBr}_4$ NPLs made in 15 cm reactor tubes with $Q_{\text{precursor}} = 5\text{mL/hr}$ at varied toluene injection..... 86

Figure 31 - Average corner to corner length and distribution of $(\text{PEA})_2\text{PbBr}_4$ NPLs made in 15 cm reactor tubes with $Q_{\text{precursor}} = 5\text{mL/hr}$ at varied toluene injection. 86

Figure 32 - Comparison of emission peak position of a variety of trials. Chlorobenzene and dichloromethane samples were created with Q_{anti} held constant at 1200 mL/hr and 15 cm reactor tube lengths. The variable tube length trials were conducted with toluene as the antisolvent and Q_{tol} was a constant 1200 mL/hr. 88

Figure 33 - Comparison of FWHM of emission of a variety of trials. Chlorobenzene and dichloromethane samples were created with Q_{anti} held constant at 1200 mL/hr and 15 cm reactor tube lengths. The variable tube length trials were conducted with toluene as the antisolvent and Q_{tol} was a constant 1200 mL/hr. 89

Figure 34 - TEM images of (a) and (c) LARP control and (b) and (d) flow reactor (1200 mL/hr toluene and 5 mL/hr precursor) $(\text{PEA})_2\text{PbBr}_4$ and $(\text{PEA})_2\text{PbI}_4$ NPLs, respectively. All scale bars = 2 μm . (e)-(f) UV-vis absorbance and PL of (e) $(\text{PEA})_2\text{PbBr}_4$ and (f) $(\text{PEA})_2\text{PbI}_4$ NPLs, respectively. 91

Figure 35 - (a) PLQY, (b) emission peak position, and (c) FWHM of $(\text{PEA})_2\text{PbI}_4$ NPLs produced in 15 cm reactor tube with a constant 1200 mL/hr toluene (antisolvent) flowrate and precursor solution flowrates ranging from 5-30 mL/hr (see x axis). 92

Figure 36 - (a) AFM image of (PEA) ₂ PbBr ₄ NPL made in a 15cm reactor tube at Q _{tol} =1200 mL/hr and Q _{precursor} =5 mL/hr. (b) Cross-sectional analysis of the line indicated in (a).....	93
Figure 37 - TEM images of (PEA) ₂ PbBr ₄ NPLs produced with a precursor solution concentration of 0.04M PbBr ₂ and 0.08M PEABr (double concentration in DMF) in a 15cm reactor with toluene as the antisolvent at a constant flowrate of 1200 mL/hr and precursor injection rates ranging from 5-30 mL/hr, that is, (a) 5 mL/hr, (b) 10 mL/hr, (c) 15 mL/hr, (d) 20mL/hr, (e) 25 mL/hr, and (f) 30 mL/hr, respectively. All scale bars = 2 μm.	95
Figure 38- (a) PLQY, (b) emission peak position, and (c) FWHM of (PEA) ₂ PbI ₄ NPLs produced with precursor solutions of 0.02M PbBr ₂ and 0.04 PEABr (normal concentration in DMF) and 0.04M PbBr ₂ and 0.08M PEABr (double concentration in DMF) in a 15 cm reactor tube with a constant 1200 mL/hr toluene (antisolvent) flowrate and precursor solution flowrates ranging from 5-30 mL/hr (see x axis).	96
Figure 39 – General photoinitiated thiol-ene reaction mechanisms ²⁵⁵	102
Figure 40 – Characterization of BABr and BeABr cations by (A) FT-IR and (B) NMR to verify the existence of C=C double bond	109
Figure 41 - TEM images of n=1 L ₂ PbBr ₄ NPLs made with (A) BABr, (B) BeABr, (C) PEABr, and (D) VBABr	109
Figure 42 – PL of n=1 and n=2 NPLs made with (A) BABr, (B) BeABr, (C) PEABr, and (D) VBABr alkylammonium cations	110
Figure 43 – Schematic of thiol-ene crosslinking unsaturated alkylammonium cations in NPLs	111

Figure 44 – Evolution of PLQY of (BeA) ₂ PbBr ₄ and (BA) ₂ PbBr ₄ NPLs during UV exposure. NPL solution included DMPA and hexanedithiol.....	112
Figure 45 – PL of n=1 BeABr NPLs (A) before and (B) after illumination with LED and addition of ethane dithiol and DMPA.....	114
Figure 46 – Synthesis scheme for 1, 6, and 8 carbon perfluorinated cations	115
Figure 47 – NMR of BeA, perfluoro ethanethiol (PFET), and perfluoro ethane ammonium bromide	116
Figure 48 - NMR of BeA, perfluoro octanethiol (PFOT), and perfluoro octane ammonium bromide	117
Figure 49 - NMR of BeA, perfluoro decanethiol (PFDT), and perfluoro decane ammonium bromide	118
Figure 50 – PL emission spectra of n=2 NPLs made with (a) PFDABr, (b) PFOABr, (c) PFEABr, and (d) OABr cations.	121
Figure 51 – PL evolution of NPLs made with perfluorinated cations. 1 mL water dropped into 5mL NPL/toluene solution	121
Figure 52 – Evolution of (a) absolutely and (b) normalized PLQY of NPLs made with OABr and PFDABr alkylammonium cations. 1 mL of deionized water was dropped into a 5 mL NPL/toluene solution after time 0.	122

LIST OF SYMBOLS AND ABBREVIATIONS

RP	Ruddlesden-Popper
MA	Methylammonium
LED	Light emitting diode
FWHM	Full width at half maximum emission
PEA	Phenylethylammonium
BABr	Butylammonium bromide
PNC	Perovskite nanocrystal
PLQY	Photoluminescence quantum yield
DFT	Density functional theory
LARP	Ligand assisted reprecipitation
DMF	Dimethylformamide
DMSO	Dimethyl sulfoxide
PS	Polystyrene
PAA	Poly(acrylic acid)
PAA b PS	Poly(acrylic acid) block polystyrene
P4VP- <i>b</i> -PAA- <i>b</i> -PS	Poly(4-vinylpyridine) block poly(acrylic acid) block polystyrene
PEO	Poly(ethylene oxide)
ATRP	Atom transfer radical polymerization
Q	Flowrate
OA	Oleic acid
OAm	Oleylamine
BiBB	α -bromoisobutyryl bromide
NMP	1-methyl-2-pyrrolidinone
PMDETA	N,N,N',N',N''-pentamethyldiethylene triamine
THF	Tetrahydrofuran
CDCl ₃	Deuterated chloroform
DMF-d ₇	Deuterated dimethylformamide
β -CD	β -cyclodextrin
St	Styrene
Tba	<i>tert</i> butyl acrylate
Re	Reynolds Number
GPC	Gel permeation chromatography
PL	Photoluminescence
TEM	Transmission electron microscopy
PtBA	Poly(<i>tert</i> butyl acrylate)
¹ H-NMR	Proton nuclear magnetic resonance
2D	Two dimensional
OABr	Octylammonium bromide
NPLs	Nanoplatelets
DCM	Dichloromethane
FA	Formamidinium
3D	Three dimensional

PCE	Power conversion efficiency
QDs	Quantum dots
NSs	Nanosheets
NWs	Nanowires
V-18	4-vinyl-benzyl-dimethyloctadecylammonium chloride
DMPA	2,2,-dimethoxy-2-phenylacetophenone
MABr	Methylammonium bromide
BeABr	Buteneammonium bromide
VBABr	4-vinyl-benzylammonium bromide
PFDAbr	Perfluorodecane ammonium bromide
PFOABr	Perfluorooctane ammonium bromide
PFEABr	Perfluoroethane ammonium bromide
FT-IR	Fourier transform infrared spectroscopy
HDT	Hexanedithiol
PFET	Perfluoroethane thiol
PFOT	Perfluorooctane thiol
PFDT	Perfluorodecane thiol

SUMMARY

Due to their tremendous optoelectronic properties, lead halide perovskite materials have recently been extensively studied for their use in numerous applications, including as solar cells, photodetectors, scintillators, and light emitting diodes. Perovskite nanocrystals, in particular possess tremendous potential as emitters due to their room temperature solution processability, defect tolerance, widely tunable emission wavelength, narrow full width at half maximum of emission, and high photoluminescence quantum yield. Unfortunately, perovskite nanocrystals do have some notable weaknesses, such as poor stability in many ambient conditions (moisture, heat, ultraviolet light) and a reliance on batch processing techniques. Many of these strengths and weaknesses originate from the ionic nature of the ABX_3 metal halide perovskite crystal structure. For the many advantageous properties of perovskite nanocrystals to be realized in at a commercial scale, the stabilities and production rate of perovskite nanocrystals must be significantly increased. To that end, this dissertation provides three unique approaches to either increase the stability or production rate of metal halide perovskite nanocrystals. These strategies include using unique organic chemistries to rationally craft molecules that will boost stability. Additionally, the use of a flow reactor for continuous synthesis of perovskite nanocrystals is explored. Specifically, three different research projects employ different strategies to enhance stability and production, as summarized below:

First, nonlinear block copolymer nanoreactors were integrated into flow reactors to continuously manufacture highly stable perovskite nanocrystals. Star-like poly(acrylic acid)-*b*-polystyrene copolymer nanoreactors were first synthesized via sequential atom transfer radical polymerization. They were then integrated in a house-built flow reactor to

template the growth of perovskite nanocrystals. A variety of parameters were tuned to optimize synthesis, including antisolvent composition, antisolvent flowrate, and precursor solution flowrate. Due to the permanent ligation from the polymer nanoreactor, perovskite nanocrystals manufactured with this strategy display significantly enhanced colloidal, UV, and thermal stabilities over those synthesized with conventional ligands. Such scaling up of highly stable perovskite nanocrystals represents an important step towards their eventual use in many practical applications in optoelectronic materials and devices.

Second, Ruddlesden-Popper perovskite nanoplatelets were continuously manufactured via a flow reactor. Because of their enhanced quantum confinement, colloidal two-dimensional Ruddlesden-Popper (RP) perovskite nanosheets with a general formula $L_2[ABX_3]_{n-1}BX_4$ stand as a promising narrow-wavelength blue-emitting nanomaterial. A flow reactor was designed and optimized to continuously produce high-quality $n=1$ RP perovskite nanoplatelets. The effects of antisolvent composition, reactor tube length, precursor solution injection rate, and antisolvent injection rate on the morphology and optical properties of the nanoplatelets was systematically examined. The investigation suggests that flow reactors can be employed to synthesize high-quality L_2PbX_4 perovskite nanoplatelets (i.e., $n = 1$) at rates greater than 8 times that of batch synthesis. Mass-produced perovskite nanoplatelets promise a variety of potential applications in optoelectronics, including light emitting diodes, photodetectors, and solar cells.

Third, thiol-ene chemistry was used to rationally engineer alkylammonium cations for highly stable Ruddlesden-Popper perovskite nanoplatelets. The hydrophobic nature of the bulky alkylammonium cations on Ruddlesden-Popper perovskite has been shown to

increase their stability relative to conventional ABX_3 perovskite. Additional chemical alteration to these organic molecules should thus further enhance stability. In this dissertation, thiol-ene click chemistry was used in two different methods to engineer the alkylammonium cations. First, *in-situ* crosslinking of unsaturated cations to craft organic shells around individual L_2PbBr_4 nanoplatelets was attempted. Second, *ex-situ* synthesis of various superhydrophobic perfluorinated alkylammonium cations was performed. The properties and stabilities of nanoplatelets made with increasing degrees of perfluorination were studied, and it was found that increasing the number of fluorinated carbons in the alkylammonium cations resulted in greater water stability. This study demonstrates how unique chemistries can be used to craft perovskite materials that can meet the stability demands of broad applications.

Through these three projects, this dissertation shows that the stability and production rate of perovskite nanocrystals can be increased towards that needed for widespread adoption. Encouragingly, the strategies presented are widely applicable and do not necessitate difficult experimental conditions. Thus, future studies can build on the fundamental science explored in this dissertation to further push perovskite nanocrystals to reach their tremendous potential.

CHAPTER 1. INTRODUCTION

Metal halide perovskite materials have recently garnered significant research interest due to their outstanding optoelectronic properties. Perovskite materials generally have the formula ABX_3 , where A is a monovalent cation (i.e. Cs^+ , MA^+ , FA^+), B is a divalent cation (i.e. Pb^{2+} , Sn^{2+} , Bi^{2+} , etc.), and X is a halide anion (I, Br, Cl). The halide ions create corner sharing BX_6 octahedra around the divalent B^{2+} cations, and the A^+ cation occupies the cubo-octahedral cavity within the corner shared BX_6 octahedral framework (as shown in **Figure 1a**).

Though inorganic lead halide perovskites ($CsPbX_3$, X=Cl, Br, I) were first discovered in the 19th century,¹ it took until the 1950s to elucidate their crystal structure and semiconductive properties.² This material enjoyed relative obscurity until 2009 when Kojima *et al.* incorporated $CH_3NH_3PbBr_3$ ($MAPbBr_3$) into a sensitized solar cell and obtained a solar energy conversion of 3.8%.³ Since then, the solar conversion efficiency of perovskite solar cells has dramatically increased, reaching greater than 25%.⁴ Much of the successes of this material can be traced to its unique properties, including long carrier diffusion lengths,⁵⁻⁶ high carrier mobilities,⁷ long range and balanced electron and hole transport,⁸ low trap density,⁹ multiphoton high absorption coefficient,¹⁰⁻¹¹ and direct and tunable bandgaps.¹² These properties have led to applications greater than photovoltaics, such as photodetectors,¹³⁻¹⁶ light emitting diodes (LEDs), and lasers.¹⁷⁻²⁰

1.1 Lead Halide Perovskite

1.1.1 Variations of Perovskite Crystal Structures

While traditional perovskite possesses the ABX_3 structure outlined above, there are various other forms of perovskite. A particularly interesting phase, and a focus in later parts of this dissertation, is the Ruddlesden-Popper (RP) phase. RP perovskite is formed when a bulky monovalent cation is substituted in the A site. If the cation is sufficiently large, it will inhibit the formation of 3D perovskite structure, limiting the crystal to corner-sharing octahedral layers. The resulting RP perovskite has the formula $L_2(ABX_3)_{1-n}BX_4$, with n being the number of layers of BX_6 octahedra (as illustrated in **Figure 1b**). Monolayer RP perovskites experience significantly increased quantum confinement, which drastically alters their optical properties, including blue shifting emission/absorption and narrowing full width at half maximum of emission (FWHM).²¹⁻²² Additionally, these organic/inorganic hybrid RP perovskites possess superior ambient stability to conventional PNCs due to the ionically-bound bulky alkylammonium cations.²³ The hydrophobic nature of these cations inhibits the diffusion of moisture through to the inorganic perovskite lattice, thereby enhancing stability.

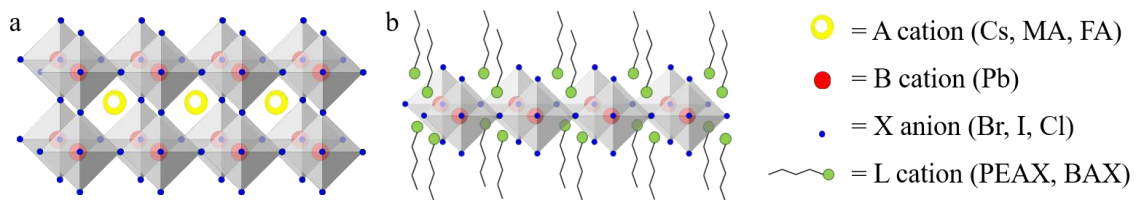


Figure 1 - (a) Schematic diagram of ABX_3 perovskite structure. (b) Schematic of $n=1$ Ruddlesden-Popper phase perovskite. Note that while the L cations in the diagram are linear, they can have a variety of diverse architectures.

A variety of alkylammonium cations have been used to craft RP perovskite, a list of which is provided in the **Figure 2**.²⁴ Short alkylammonium cations has been found to allow for only corner sharing of the PbX_6 octahedra, while longer cations have been found to result in both corner and face sharing of the PbX_6 octahedra.²⁵ Phenylethylammonium (PEA) and butylammonium (BA) are among the most popular choices of cation, because they are sufficiently short to promote only corner sharing octahedra. Notably, there is a lower limit to the length of the cations, as they must contain at least four carbons (longer than propyl ammonium) in the backbone to prohibit electronic coupling between the inorganic atomic layers.²⁶⁻²⁷

Organic spacer cation	Molecular structure
PEA ^[18]	
n-BA ^[22]	
iso-BA ^[20]	
n-C6H13NH3 ^[41]	
(FC7H4NH3) ^[44]	
n-C8H17NH3 ^[42]	
OA ^[46]	
POEA ^[47]	
NMA ^[48]	
NAAB ^[50]	
DMEN ^[51]	
DMAPA ^[51]	
DMABA ^[51]	
Bd ^[52]	
Hd ^[52]	
Od ^[52]	
EDBE ^[53]	
Ava ^[55]	

Figure 2 - Chemical structures of various alkylammonium cations that have been used in RP perovskites

1.1.2 Perovskite Nanocrystals

While bulk perovskite has proven to be a powerful material for the above listed applications, the focus of this study will be on perovskite nanocrystals (PNCs). PNCs possess many of the valuable attributes of bulk perovskite but have the additional benefit of being easily solution processed. This has enabled the use PNCs in a wide range of applications unavailable to bulk perovskite, including interfacial band engineering layer in photovoltaics²⁸, fillings holes and cracks in thin film perovskite photodetectors²⁹, boosting the efficiency of solar cells by down converting UV light³⁰, adjusting emitted light from

blue chip LEDs³¹, chemical detection³², x-ray scintillation³³, hydrogen generation³⁴, anti counterfeiting³⁵, and bioimaging.³⁶

1.2 Benefits of Lead Halide Perovskite Nanocrystals

1.2.1 Optical Properties

The optical properties of PNCs are one of their most attractive attributes, and in particular, their emissive performance makes them prime candidates for next-generation emitters. PNCs possess a high photoluminescence quantum yield (PLQY), narrow full width at half maximum emission (FWHM), and highly tunable emission wavelengths.^{12,37-40} These properties enable them to cover the entire visible light spectrum with bright and pure light. PLQYs near unity have been reported for MAPbBr₃ PNCs.³⁸⁻⁴⁰ As shown in **Figure 3 a & b**, the peak emission wavelength of PNCs can be tuned by altering the halide composition. This facile composition-based emission tuning is a unique benefit for PNCs, as conventional semiconductor quantum dots rely solely on quantum confinement to alter emission wavelengths. **Figure 3c** further illustrates how the absorption of PNCs can be altered by tuning their composition. Additionally, PNCs can be easily synthesized in solution at room temperature, which furthers their promise as low-cost emitters for future usage.⁴¹⁻⁴³

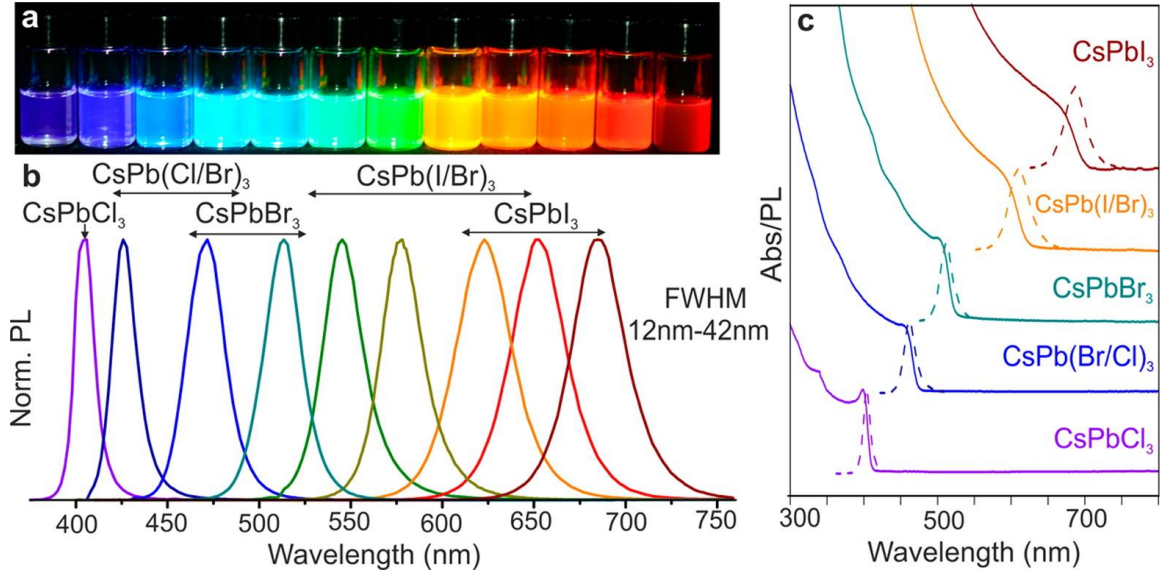


Figure 3 - (a) photograph of CsPbX₃ NCs under UV excitation (b) Photoluminescence spectra of CsPbX₃ PNCs, and (c) Absorbance and emission spectra of CsPbX₃ PNCs with various halide compositions (X ranging from purely Cl to Br to I)⁴⁴

1.2.2 Excellent Charge Carrier Dynamics

Perovskite materials are also noted for their beneficial charge carrier dynamics. Optically excited charge carriers in perovskite materials are either freely diffused or excitonically bound, mainly determined by the exciton binding energy, carrier density, and temperature.⁴⁵ The generation, transport and recombination of charge carriers depends significantly on the composition, crystal structure, size, and defects of perovskites.⁴⁶ Free charge carriers move with diffusion coefficients ($D_{n,p}$) in the absence of external fields, and drift with mobility ($\mu_{n,p}$) in a non-zero electric field related through the Einstein relation:

$$\mu_{n,p} = eD_{n,p}/k_B T$$

Equation 1 – Einstein Relation

where e is the absolute value of electron charge, k_B is the Boltzmann constant and T is the temperature. $D_{n,p}$ and $\mu_{n,p}$ are related to the electronic band structure of perovskite through the carriers' effective mass (m^{eff}) which is correlated to spin-orbital coupling, chemical composition, and crystal size.⁴⁵⁻⁴⁶ The $D_{n,p}$ and $\mu_{n,p}$ in perovskites have been proven to be modest compared with other high-quality semiconductors due to scattering by the presence of defects and lattice vibrations.⁴⁶⁻⁴⁹ Before recombination, charge carriers have been found to exhibit an average recombination life time (τ) determined by the radiative and non-radiative recombination rates, which are correlated to the carrier density, trap density, and many other factors.⁴⁶ τ and $\mu_{n,p}$ are correlated to the diffusion length (L_D) of charge carriers via following equation:

$$L_D = \left(\frac{k_B T \mu_{n,p} \tau}{e} \right)^{1/2} = (D_{n,p} \tau)^{1/2}$$

Equation 2 – Diffusion length of charge carriers in perovskite materials

where high $\mu_{n,p}$ and long τ proportionally increase the L_D . The long L_D in perovskites has been found to contribute to their efficient charge transport in photovoltaic applications.⁴⁵

The charge carrier recombination dynamics of perovskites are governed by monomolecular, bimolecular, and Auger recombination via following rate equation:⁴⁵

$$-\frac{dn}{dt} = k_1 n + k_2 n^2 + k_3 n^3$$

Equation 3 – Recombination dynamics of perovskite materials

where k_1 , k_2 , k_3 are the rate constants of monomolecular, bimolecular and Auger recombination, respectively, and n is the carrier concentration. These recombination

pathways collectively determine the τ and affect the L_D .⁴⁵ The monomolecular recombination of charge carriers, also known as trap-assisted recombination, is largely governed by the energy, density, and distributions of trap states, and is highly influenced by the purity and crystallinity of perovskites.⁵⁰⁻⁵² The monomolecular recombination rate is proportional to the trap density within perovskites.⁵⁰⁻⁵¹ On the other hand, the bimolecular recombination in perovskites is primarily determined by the electronic band structure, and thus the chemical composition of perovskites. Compositional engineering of perovskites has been shown to alter their spin-orbital coupling and electronic band structure, which can enable efficient spatial separation of charge carriers, extremely low bimolecular recombination, and long L_D exceeding one micron in polycrystalline perovskite films.⁵¹ The last pathway of carrier recombination, Auger recombination, is usually dominant at high charge carrier concentration and manifests as a phase-specific characteristic, which is prevalent in the orthorhombic phase at low temperature and rare in tetragonal and cubic phases at high temperature.⁵⁰ The high charge-collection efficiency and open-circuit voltage in perovskite-based photovoltaics has been attributed to low trap densities and recombination rates, and prolonged τ .⁵³

1.2.3 Defect Tolerance

A particularly unique property of PNCs is their spectacular defect tolerance. In traditional semiconductors (i.e. CdSe, CdS, InAs, etc.), the presence of defects can drastically affect the material's optoelectronic properties.⁵⁴ For example, in CdSe, the removal/displacement of a Cd ion results in a trap state from localized nonbinding or weakly bonding Se orbitals.^{37, 55} These orbitals fall deep within the bandgap, resulting in traps that severely diminish the optical properties. Trap states are usually formed because

the bandgap is between bonding valence band and antibonding conduction band states. Conversely, metal halide PNCs have demonstrated higher defect tolerance than conventional semiconducting QDs.⁵⁶⁻⁵⁷ Their ability to retain pristine electronic band structure in the presence of a high concentration of defects is attributed to their unique electronic band structure in which bonding-antibonding interactions exist within their conduction and valence bands.⁵⁸ Energy level splitting caused by strong spin-orbital coupling effects favorably broadens the conduction bands and increases the possibility of defect states located within conduction bands (**Figure 4 a & b**).⁵⁹ Density functional theory (DFT) calculations have corroborated that vacancies, interstitial atoms, and surface states do not induce defect states within perovskites' bandgap.⁶⁰⁻⁶² Notably, because of their defect-tolerant nature, PNCs possess outstanding optical properties without the need for surface passivation, high purity, high temperature, or equipment-intensive vacuum synthesis, all of which are critical for conventional QDs.

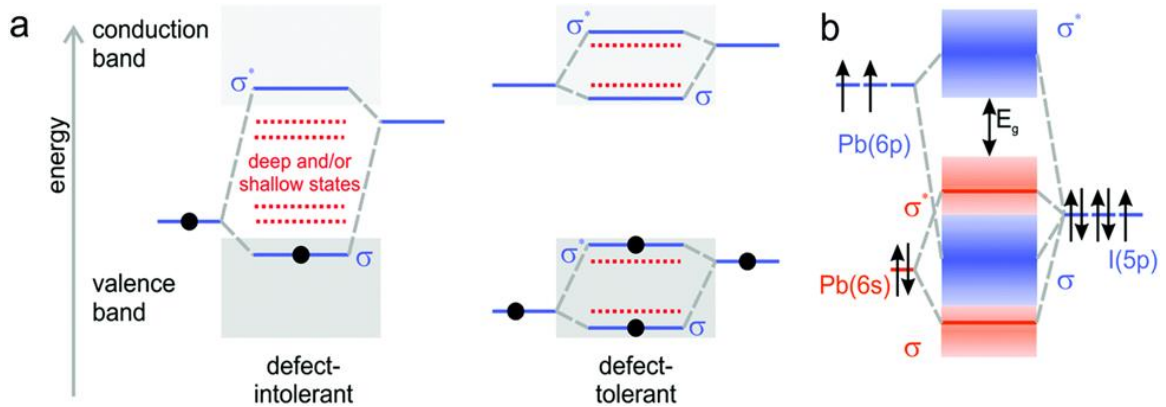


Figure 4 - (a) Illustration of material with band structure intolerant to defects (left) and ideal band structure of material with optimal defect tolerance. (b) Band structure of CsPbI₃ perovskite⁵⁹

1.2.4 Facile Synthesis

Another major benefit of PNCs is their facile synthesis. PNCs are generally manufactured via the ligand-assisted reprecipitation (LARP) method. The LARP technique is the most common and most appealing because it can be conducted at ambient temperature and atmosphere.^{41-42, 59, 63} In LARP, perovskite precursors and amphiphilic ligands dissolved in a polar solvent (i.e. DMF or DMSO) are dropped into a vigorously stirred antisolvent (i.e. toluene). Upon mixing with the antisolvent, the crystals precipitate and the organic ligands populate the surface. (**Figure 5a**) These ligands ensure the colloidal stability of the nanocrystals in the nonpolar solvent, preventing them from precipitating out. Because of the ability to be produced at room temperature, PNCs have great promise for continuous manufacturing, which will be detailed later.⁶⁴ This low temperature synthesis stands in stark contrast to conventional semiconductor NCs which require high temperature synthesis. This high temperature is needed to ensure the formation of highly crystalline NCs with few defects, which as stated above can drastically decrease the optical properties of conventional semiconductor quantum dots.^{37, 55}

While not necessary, PNCs can also be synthesized with the hot injection method (**Figure 5b**). In typical hot injection processes, the lead halide precursor (PbX_2), ligands (oleylamine, oleic acid), and high temperature organic solvent (i.e. 1-octadecene) are heated to ~ 150 C, at which point a monovalent cation oleate (i.e. cesium oleate) is injected.⁶⁵ This technique is generally only used for fully inorganic PNCs (i.e. CsPbX_3) and not for hybrid organic inorganic varieties (i.e. FAPbX_3 , MAPbX_3).⁶⁶ It is worth noting that hot injection of perovskite NCs can occur at lower temperatures (~ 150 C) and requires

significantly less growth time (~2 seconds) than that needed for conventional semiconductor NCs (~300 C and minutes, respectively).⁶⁷

Notably, while both LARP and hot injection of perovskite nanocrystals are relatively simple compared to other legacy nanomaterial synthesis procedures, they are both still batch processes. For PNCs to reach their potential, a move away from batch towards continuous production is necessary. The room temperature and ambient conditions synthesis of PNCs suggests that continuous synthesis can be accomplished. Later portions of this thesis will discuss continuous production of PNCs in much greater detail.

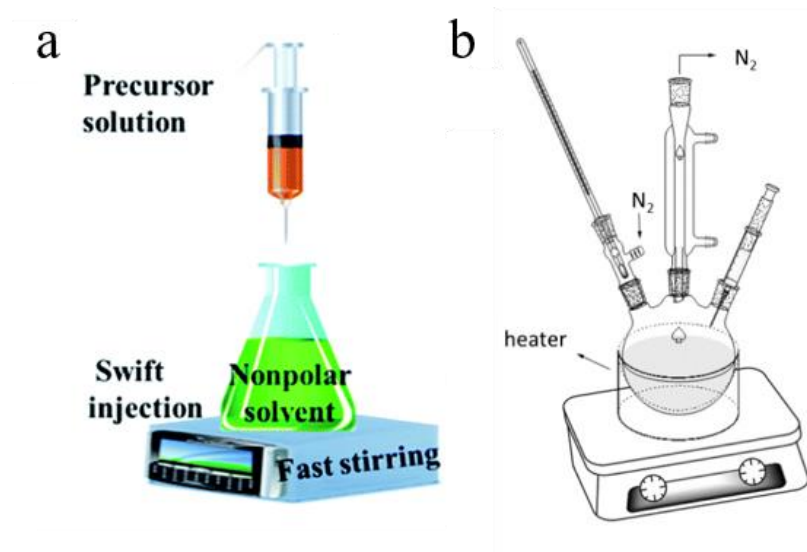


Figure 5 - Representative illustration of necessary equipment for (a) LARP⁶⁸ and (b) hot injection⁶⁹ PNC synthesis methods

1.3 Limitations of Lead Halide Perovskite Nanocrystals

While PNCs have been demonstrated to possess significant advantages, they also have many potential challenges to their future widespread deployment. Of particular concern is lead halide perovskite's instability to many conditions found in the ambient environment (i.e. moisture, heat, UV, etc.). This inherent instability becomes particularly problematic for perovskite nanocrystals because of their increased surface to volume ratio.³⁷ The following subsections will detail these instabilities, their root causes, and also touch on other challenges not related to stability.

1.3.1 Polar Solvent and Moisture Sensitivity

PNC's instability towards polar solvents and moisture might be the largest obstacle preventing their widespread use. Lead halide perovskite's extreme sensitivity towards polar solvents can be traced to their ionic crystal nature and large surface energy.⁷⁰ The relatively soft intrinsically ionic structure of PNCs differs significantly from the rigid covalent crystal lattices of metal chalcogenide and pnictides⁷⁰. This soft ionic crystal (and its low crystal lattice energy) results in a high solubility for perovskite in nearly all polar solvents. In practice, this solubility allows for the dissolution/disintegration of perovskite into these solvents, which quenches any beneficial optical properties.

1.3.2 Photo Instability

Because most PNC devices rely on photoluminescence, the photo instability of PNCs stands as a particularly troubling challenge. Illumination of metal halide perovskite has been shown to lead to many deleterious effects⁷¹, including phase segregation⁷²⁻⁷³,

lattice expansion⁷⁴⁻⁷⁵, and ion migration⁷⁶⁻⁷⁷. Additionally, prolonged UV exposure has also been shown to sharply reduce the photoluminescent emission of PNCs. This PL quenching has been attributed to the loss of ligands from the surface from continuous UV irradiation⁷⁸. This loss of surface ligands results in growth/agglomeration of PNCs and a substantial increase in the number of surface defects, both of which boost non-radiative recombination rates⁷⁹⁻⁸⁰. Additionally, prolonged UV exposure has been shown to photo-oxidize Pb atoms in PNCs, thereby quenching emission⁸¹. This study observed the formation of PbCO₃ and PbO phases on the surface of PNCs. These new oxidized phases acted as nonradiative recombination centers, which quenched PL properties. Clearly, for PNCs to achieve their potential, their photostability must be improved.

1.3.3 Thermal Instability

The thermal properties of metal halide perovskite differ significantly from the well-studied perovskite oxides. Perovskite oxides are known for their numerous applications (including catalysis, random access memory, ferromagnets, etc.), and much of their properties can be attributed to their thermally-stable rigid crystal structure³⁷. Conversely, metal halide perovskite possesses lower charge on their halide ions (-1 vs. -2), which results in a crystal lattice energy $\frac{1}{4}$ that of perovskite oxides (as calculated by the Glasser generalization of the Kapustinskii equation)⁸². This reduced crystal lattice energy manifests as a significant reduction in melting temperature. For example, CsPbBr₃ and CsPbI₃ melt at 570 °C⁸³ and 460 °C⁸⁴, respectively while CaTiO₃ melts at 2000 °C³⁷. This decreased melting point is especially significant for PNCs, because nanosized materials have been demonstrated to possess a depressed melting point, compared to bulk materials⁸⁵.

1.3.4 Colloidal Instability

Perovskite nanocrystals also suffer from relatively poor colloidal stability. Their poor colloidal stability has been attributed to the highly dynamic nature of the bonds between the PNC surface and the ligands conventionally used in synthesis (i.e. oleic acid, oleylamine)⁸⁶. These dynamically bound ligands adsorb and desorb relatively quickly, which can leave surface defects or reduced solubility in organic solvents. In contrast, conventional semiconductor nanocrystals (CdSe, PbS, etc.) generally possess ligands that are either covalently attached or strongly bound⁸⁷. As such, PNCs are unable to undergo many solution processes that are common for other semiconductor. As an example, even precipitating conventionally ligated PNCs with nonpolar hexane has been shown to lead to ligand desorption, agglomeration, and loss of photoluminescence⁸⁸. Thus, for the full potential of their easy solution synthesis and processing to be fully realized, the colloidal stability of perovskite nanocrystals must be improved.

1.3.5 Reliance on Batch Synthesis Methods

As noted in *Section 1.2.4*, the synthesis of PNCs requires relatively milder conditions than conventional semiconductor nanocrystals (i.e. lower temperatures and ambient atmospheres). While these milder conditions generally make synthesis of PNCs easier than conventional semiconductor nanocrystals, most PNC synthesis is conducted via batch techniques like LARP and hot injection. These techniques yield high quality PNCs, but batch manufacturing has many inherent disadvantages. One of these disadvantages is the difficulty in scaling up batch techniques. Precisely controlling synthetic parameters like temperature, stirring rate, mixing, and precursor injection position are crucially important

to ensure consistency in the final product⁶⁹. As the volume of reactors increases to accommodate the needs of mass production, controlling these important parameters becomes practically challenging. For example, maintaining a consistent temperature and stirring rate in lab scale reactors (~10 mL) is simple, but precise control over vats over 100 L becomes difficult. Because these parameters cannot be accurately controlled, the properties of the PNCs can vary from batch to batch, which obviously is unacceptable for commercial applications. Batch synthesis has the additional negative of being intermittent in nature. Because of this, batch synthesis occurs in spurts of a finite quantity. Conversely, ideal industrial synthesis occurs in a continuous manner, where the production is only hindered by the flowrates of the solvents. Some initial exploration into manufacturing PNCs in continuous flow reactors has been explored⁸⁹⁻⁹⁵, but significant more study is needed to enable the reliable synthesis of high quality PNCs. These limitations are, frankly, more of an engineering problem than a question of fundamental science, but nonetheless they stand as an obstacle towards consistent mass production of PNCs.

1.4 Employing Polymers to Enhance the Properties of Perovskite

Despite recent significant advances in metal halide PNCs research, their instability remains a daunting issue that limits their widespread application.⁹⁶ Exposure to light, elevated temperature, moisture, and other polar solvents can easily destroy the crystal structure of perovskite materials.⁹⁷⁻⁹⁸ In addition, metal halide PNCs also experience inevitable agglomeration when transitioning from a liquid state to solid state during processing for technological applications, which may lead to the reduced performance of as-prepared optoelectronic devices.⁹⁹⁻¹⁰⁰ Polymers have been widely employed to eliminate the issues described above by producing PNC/polymer nanocomposites.¹⁰⁰⁻¹⁰⁴ In this

context, polymers possess a myriad of unique advantageous attributes, such as the ability to chemically interact with perovskites,¹⁰⁵ the capability of passivating the surface defects of PNCs,¹⁰⁶ favorable mechanical properties,¹⁰⁷ lightweight, solution processability,¹⁰⁸ low diffusion rates of oxygen and moisture,¹⁰⁹ high chemical resistance,¹¹⁰ and are often transparent in the visible wavelength region. In addition, conjugated polymers can facilitate favorable band energy level alignment,¹¹¹ which facilitates charge separation at the PNCs/conjugated polymer interface and increases the lifetime of charge carriers.¹¹¹⁻¹¹² PNC/polymer nanocomposites simultaneously bestow enhanced control over the size and morphology of PNCs,¹¹³ improved stability,¹¹⁰ decreased agglomeration of PNCs in the solid state,¹¹⁴ and efficient charge separation. In addition to the enhanced optoelectronic properties, devices made from these nanocomposites possess processing flexibility, stretchability, and self-healing properties inherited from the polymers.^{110, 115-116}

The large surface area to volume ratio of NCs results in high surface energies that promote aggregation of NCs. As noted above, capping ligands, such as small organic molecules and polymers, have been widely utilized in the colloidal synthesis of metal halide PNCs to stabilize their surface. The interaction between the small organic molecule capping agents and PNCs is, however, primarily through weak, noncovalent, dynamic bonding^{70, 86} which can easily be broken by high temperature and UV irradiation. Variation in ion strength and solvent composition have also been found to degrade PNCs.^{98, 117} Therefore, encapsulating PNCs with polymeric capping ligands (with stronger binding than conventional small organic molecular capping ligands) has been introduced as an alternative.¹¹⁸ Chemically anchoring polymers onto PNCs can also eliminate phase

separation between polymers and PNCs due to their strong chemical interactions, which yields starkly different samples than physical mixing.

The above-mentioned synthetic approaches often require the addition of conventional small organic molecule ligands to control the uniformity of size and morphology of PNCs. Notably, polymerizable and polymer capping ligands bind to PNC surfaces through a similar mechanism as conventional small organic molecule ligands. Therefore, the dynamic dissociation of ligands from PNCs surfaces remains an inevitable challenge that limits the stability of PNCs under high humidity and temperature.¹¹⁹ To this end, *in-situ* synthesis of PNCs using linear polymer micelles as nanoreactors has been developed as an alternative approach.¹²⁰

1.4.1 Linear Block Copolymer Ligands

Recently, the amphiphilic block copolymer polystyrene-*block*-poly-2-vinylpyridine (PS-*b*-P2VP) has been demonstrated to self-assemble into a reverse micelle structure in nonpolar solvents, with the P2VP and PS blocks as the core and shell, respectively. This reverse micellar structure was then utilized to craft PNCs. Perovskite precursors were mixed with PS-*b*-P2VP copolymers in nonpolar solvents, where the internal P2VP block efficiently bound to the metal precursors (i.e. cesium bromide and lead bromide) through the coordination interaction between the pyridine groups of P2VP and the metal moieties of precursors. This selective loading of the metal precursors into the reverse micelles was found to lead to nucleation and growth of CsPbBr₃ NCs, as shown in **Figure 6**.¹²⁰⁻
¹²¹_ENREF_113 Moreover, the outside PS blocks were demonstrated to sterically stabilize the metal precursors during crystal nucleation and growth, enhancing the colloidal stability

of CsPbBr₃ NCs after the reaction, and protecting the formed CsPbBr₃ NCs from moisture and polar solvents (e.g. methanol and ethanol).^{109, 120}

Because the size and morphology of the as-prepared CsPbBr₃ PNCs can easily be controlled by tuning the size and structure of the self-assembled PS-*b*-P2VP micelles, no additional small organic molecule ligands are needed.¹²⁰ This technique has also been found to eliminate ligand dissociation due to the covalent bond between the outer PS block and the inner P2VP block. Both all-inorganic (e.g. CsPbX₃) and organic-inorganic hybrid PNCs (e.g. MAPbI₃) have been synthesized using linear block copolymer nanoreactors.¹²²⁻¹²³

The dynamic instability of conventional linear polymeric micelles has proven to be a challenge in using them to craft PNCs.¹²⁴ As noted above, these micelles are thermodynamic aggregates of multiple amphiphilic molecules above critical micelle concentration, so their size and shape depend heavily on temperature, solvent properties, solution concentration, pH, and other experimental conditions.¹²⁵⁻¹²⁷ Even small variations in those parameters during PNCs synthesis can result in the dissociation of micellar structure, which leads to poor control over PNC size and morphology. Moreover, nanocomposites prepared from this approach often encapsulate multiple PNCs within one polymer micelle, which may be deleterious for biomedical applications where cellular uptake is more feasible for smaller NCs, or in optoelectronic devices that require uniform NCs dispersion.¹²⁸⁻¹²⁹

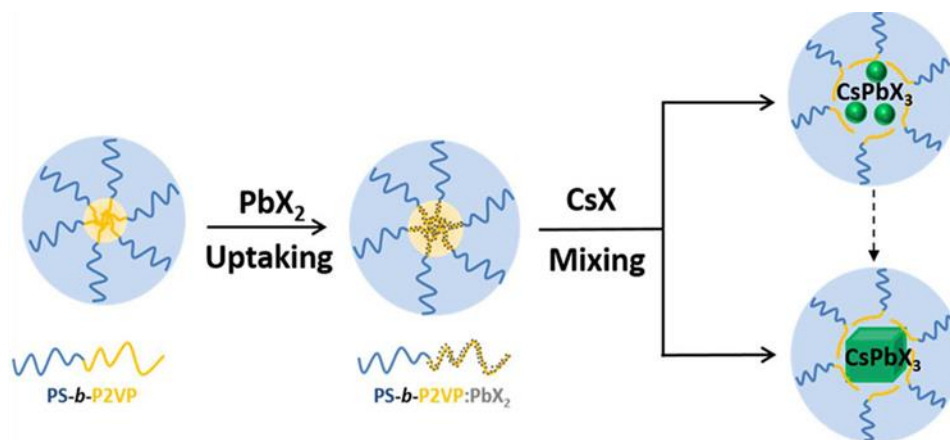


Figure 6 - Synthetic strategy for perovskite NCs using linear amphiphilic block copolymer micelles as nanoreactors.¹²⁰

1.4.2 Polymer Nanoreactors

Recently, an unconventional strategy for crafting PNCs that capitalizes on unimolecular star-shaped block copolymer micelle nanoreactors has been developed.^{113, 130-132} The amphiphilic multiarm block copolymer poly(acrylic acid)-*block*-polystyrene (PAA-*b*-PS) was synthesized by sequential ATRP, with the hydrophilic PAA block in the core and the hydrophobic PS block as the shell. The unimolecular nature of the nanoreactors endow them with enhanced spherical micellar structural stability than conventional self-assembled linear block copolymers (**Figure 7a**). Perovskite precursors have been found to selectively bind to the inner PAA blocks of the star-shaped copolymers via strong coordination with the carboxylic groups of the PAA blocks. The loaded perovskite metal precursors can then easily form covalently ligated PNCs within the nanoreactor via a facile and rapid coprecipitation reaction (**Figure 7b**). Because the PNCs are confined within the micelles, their size and size distribution can be precisely tuned by controlling the molecular weight and polydispersity of each block of the nanoreactor,

which is easily achieved during ATRP of the monomers (i.e. *tert*-butyl acrylate and styrene). Because the outer PS blocks are covalently connected to the inner PAA blocks, they are permanently capped on the surface of PNCs which prevents aggregation and endows the PNCs with remarkable stability, which will be discussed in the following section.

Enhanced protection of the final PNCs can be achieved by further functionalization and engineering of the star-shaped block copolymer nanoreactors. The addition of a small amount of divinylbenzene as a cross-linker during the ATRP reaction of styrene has been found to yield partially cross-linked PS that forms a denser protective layer on the surface of CsPbBr₃ PNCs.¹³⁰ In addition to diblock star-shaped amphiphilic copolymer nanoreactors, multiarm star-shaped triblock copolymers, namely poly(4-vinylpyridine)-*block*-poly(acrylic acid)-*block*-polystyrene (P4VP-*b*-PAA-*b*-PS), have been synthesized to craft PAA-*b*-PS-ligated PNCs (i.e. MAPbBr₃ NCs) via similar techniques and mechanisms as noted above (**Figure 7c**).¹³¹ A passivating SiO₂ shell was then formed around MAPbBr₃ NCs via the *in-situ* hydrolysis of tetramethyl orthosilicate in the compartment occupied by the outer PAA blocks (**Figure 7d**). Water soluble poly(ethylene oxide)-ligated (PEO-ligated) dual-shelled MAPbBr₃ NCs were also formed by the substitution of hydrophobic PS to hydrophilic PEO through a click reaction.¹³¹ Hollow perovskite NCs with PS chains covalently tethered to their surface were crafted by tailoring the composition of multiarm star-shaped triblock copolymer from P4VP-*b*-PAA-*b*-PS to PS-*b*-PAA-*b*-PS.¹³²

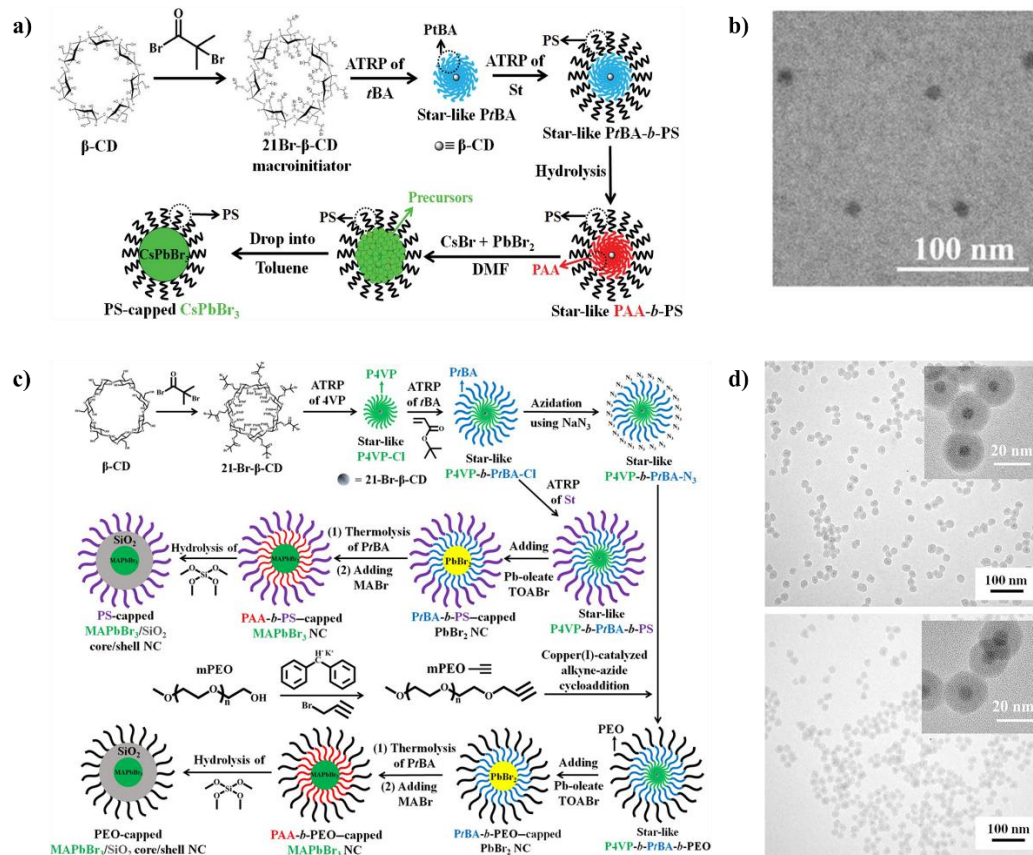


Figure 7 - a) Stepwise representation of crafting “hairy” all-inorganic perovskite CsPbBr₃ QDs with intimately and permanently capped by PS chains via capitalizing on amphiphilic star-like PAA-*b*-PS diblock copolymers as nanoreactors. b) TEM image of PS-capped CsPbBr₃ QDs with diameter = 10.1 ± 0.6 nm.¹¹³ c) Stepwise representation of the synthetic route to PS-capped MAPbBr₃/SiO₂ core/shell NCs and PEO-capped MAPbBr₃/SiO₂ core/shell NCs by exploiting star-like P4VP-*b*-PtBA-*b*-PS and P4VP-*b*-PtBA-*b*-PEO as nanoreactors, respectively. d) TEM images of PEO-capped MAPbBr₃/SiO₂ core/shell NCs with MAPbBr₃ core diameter of 6.1 ± 0.3 nm and SiO₂ shell thickness of 8.9 ± 0.4 nm (top), and MAPbBr₃ core diameter of 6.8 ± 0.3 nm and SiO₂ shell thickness of 8.0 ± 0.3 nm (bottom).¹³¹

1.5 Conclusion

This chapter has illustrated the benefits and challenges of perovskite nanomaterials. Though lead halide perovskite has recently been identified for its tremendous optoelectronic properties, its inability to maintain performance in standard ambient operating conditions severely hinders any real-world applications. For perovskite to reach its immense potential outside of the laboratory, its various instabilities (i.e. photo, thermal, colloidal, moisture) must first be remedied. Integrating polymers and organic molecules with perovskite has emerged as one promising strategy to increase relevant stabilities. Specifically, the use of block copolymer templates and the synthesis of organic/inorganic hybrid Ruddlesden-Popper perovskite has been found to increase the stability of PNCs. These techniques take advantage of the hydrophobicity of organic molecules, which can prevent diffusion of moisture to the delicate perovskite crystal.

Additionally, this chapter noted the advantages and disadvantages of common synthetic routes of PNCs. Most reported PNCs are synthesized via batch techniques like hot injection and LARP. Though PNCs require less stringent conditions than conventional semiconductor nanocrystal synthesis (lower reaction temperature, better oxygen tolerance, etc.), the batch nature of both LARP and hot injection is undesirable for commercial applications. Batch processes are harder to scale up due to practical concerns of dealing with large volumes and inherently will possess high variability batch to batch. Because scaling up is critical for commercialization of PNCs, a transition away from simple batch techniques towards continuous production methods is urgently needed. Therefore, this dissertation explores room temperature continuous

production methods by constructing a continuous flow reactor based on the LARP technique.

CHAPTER 2. MOTIVATION AND RESEARCH GOAL

2.1 Motivation

As discussed in detail above, PNCs possess many properties that could be of great value to numerous optoelectronic applications. The usage of PNCs as next generation emitters stands as a particularly appealing option, due to their outstanding optical properties and room temperature synthesis. Unfortunately, this potential cannot be realized until the environmental stability of PNCs is improved, and their synthetic techniques extend beyond lab-scale batch techniques. *Herein, the central motivation for this study is to move PNCs towards widespread usage by improving the production rate and stability of both 3D and 2D PNCs.*

Moving beyond batch synthesis is critical for future broad applications of PNCs. Synthesis of PNCs via flow reactors are promising for continuous production because, unlike batch synthesis, they are predicated on the constant flowrate of solutions to spur the desired reaction. PNCs are uniquely positioned for flow reactor manufacturing because they can be synthesized at room temperature. A modified LARP technique can be used, where the precursor solution and antisolvent meet in the reactor tube, and their mixing is accomplished by fluid dynamics between the antisolvent and precursor solution. While facile in theory, the effect of many parameters (i.e. solvent flowrates, precursor concentrations, solvent compositions) on the performance of PNCs is unknown. Study of the effects of these parameters is critical. To be a competitive synthesis method, the reaction conditions need to be optimized, and the resultant PNCs must have performance comparable to that from legacy batch techniques.

Improving the environmental stability of PNCs stands as another major barrier to their widespread application. As discussed in **Section 1.4**, the integration of PNCs with various polymers has proven to effectively boost stability. Specifically, the use of nonlinear block copolymer templates has been demonstrated to be an effective method of synthesizing highly stable PNCs^{88, 133}. These studies have, however, been restricted to batch synthesis of PNCs. Combining the benefits of polymer integration with the benefits of flow reactors to continuously craft highly stable PNCs is an area that is rich for further study. By exploring this field, two obstacles (poor stability and batch production) for widespread PNC application can be remedied simultaneously. This represents a crucial step forward towards more practical PNC materials.

While the polymer nanoreactor described above has been shown to increase PNC stability, other methods of increasing PNC stability are also urgently needed. Ruddlesden-Popper perovskite, with its ionically bound amphiphilic cations, generally possesses a relatively higher environmental stability than that of ABX_3 , but persistent moisture remains a serious concern. Functionalizing the normally fully saturated alkylammonium cations represents an exciting strategy to further boost the stabilities of RP PNCs. By starting with alkylammonium cations that possess unsaturated outermost bonds, a variety of end groups can be incorporated. In-situ growing/crosslinking organic molecular shells around RP PNCs via thiol-ene chemistry is one opportunity. Once cross linked, the hydrophobic organic shell will inhibit diffusion of moisture into the inner ionic crystal, which should prevent degradation. Additionally, engineering unique alkylammonium cations before NPL synthesis represents another strategy. By starting with the same unsaturated alkylammonium cations, cations with various functionalities can be synthesized ex-situ,

and then used to craft RP perovskite NPLs. Perfluorinated alkylammonium cations are a particularly enticing candidate due to their well-documented super hydrophobicity. Theoretically, however, many other functionalities could be adopted, including stimuli responsive varieties.

Therefore, the overall goal of this dissertation is to move perovskite nanocrystals towards commercial viability by increasing their stability and production rate via utilizing innovative organic synthesis and continuous flow reactors.

2.2 Research Objectives

- (1) Continuous synthesis of highly-stable colloidal three-dimensional perovskite nanocrystals by incorporating β -CD derived unimolecular micelle templates into a flow reactor
- (2) Continuous synthesis of stable organic/inorganic two-dimensional Ruddlesden-Popper perovskite nanoplatelets via a flow reactor
- (3) Enhancement of stability and functionality of two-dimensional Ruddlesden-Popper perovskite via engineering of the bulky alkylammonium cation

CHAPTER 3. CONTINUOUS PRODUCTION OF HIGHLY STABLE PEROVSKITE NANOCRYSTALS VIA A DUAL REACTOR APPROACH

Biesold, G. M., Liang, S., Wagner, B. K., Kang, Z., & Lin, Z. (2022). *ACS Applied Nanomaterials*, (under review)

3.1 Introduction

Metal halide perovskite, with the general structure ABX_3 , has recently been recognized for its tremendous potential in optoelectronic applications, including LEDs¹³⁴⁻¹³⁵, photodetectors^{13, 136}, scintillators¹³⁷⁻¹³⁸, solar cells¹³⁹⁻¹⁴¹, etc. Lead halide perovskite nanocrystals (PNCs) have been demonstrated to possess an array of intriguing optical properties¹⁴², including a high photoluminescence quantum yield (PLQY)¹⁴³⁻¹⁴⁵, narrow full width at half max of emission (FWHM)^{37, 146}, widely tunable emission wavelength^{137, 147}, and high defect tolerance^{58, 148}. Additionally, PNCs can be synthesized at room temperature under ambient conditions^{41-42, 149}, which stands in stark contrast to the air-free and high temperature synthesis conditions needed for conventional semiconductor quantum dots (i.e. CdSe¹⁵⁰, PbSe¹⁵¹, CdTe¹⁵²). Despite these encouraging properties, their widespread use remains hindered by their poor overall stability and their reliance on batch processing techniques. In particular, PNCs demonstrate poor moisture¹⁵³, thermal¹⁵⁴, and UV¹⁵⁵ stabilities. PNCs also often suffer from poor colloidal stability due to the dynamic bonding nature of conventional ligands (usually oleic acid and oleylamine)⁸⁶. Additionally, PNCs are most often synthesized through batch techniques (e.g. hot injection⁶⁵ and ligand assisted reprecipitation (LARP)^{42, 156}), and while these methods produce high-quality PNCs, a shift towards continuous manufacturing is needed to realize their commercial potential.

Numerous methods have been used to increase the stability of PNCs, including incorporation of PNCs in silica⁵⁹, alumina¹⁵⁷, zinc stearate¹⁵⁸. Integrating PNCs with a variety of polymer matrixes has also been demonstrated to improve stability¹⁵⁹. One of the most promising techniques to synthesize highly stable colloidal PNCs is to capitalize on amphiphilic star-like block copolymers as templates¹⁶⁰⁻¹⁶². These nanoreactors are comprised of inner poly(acrylic acid) (PAA) and outer polystyrene (PS) blocks. The inner PAA blocks can coordinate with perovskite precursors to template nanocrystal growth, while the outer PS blocks enable solubility in organic solvents. Notably, these PS chains are permanently ligated to the surface of the nanocrystals via their covalent bonded with the inner PAA blocks¹⁶³. The permanence of these ligated chains imparts better colloidal stability than that is afforded by the dynamically bound ligands in conventional colloidal synthesis¹⁶⁴.

To promote perovskite nanomaterials towards commercialization, progress beyond batch synthesis is highly desirable. Some pioneering works have developed continuous manufacturing techniques. CsPbX₃¹⁶⁵⁻¹⁶⁶ and FAPbX₃¹⁶⁷ PNCs have been synthesized using microfluidic flow systems, where precursor solutions were mixed in droplets dispersed in an inert oil medium. Cs₄PbBr₆ PNCs with excellent optical properties were synthesized using an apparatus consisting of concentric rotating cylinders that resulted in Couette-Taylor flow¹⁶⁸. MAPbX₃ PNCs have also been synthesized using conventional flow reactors^{92, 169}. In a previous work, we developed a flow reactor system to synthesize high PLQY 2D (PEA)₂PbX₄ (PEA=phenylethylammonium, X= Br, I) Ruddlesden-Popper perovskite nanoplatelets⁸⁹. Notably, while all these continuous production methods can manufacture high-quality PNCs, the final products still suffer from perovskite's

characteristic poor environmental stabilities. Thus, the continuous production of stable PNCs remains an urgent need, and the integration of novel star-like block copolymer nanoreactors into flow reactors offers an exciting solution to this end.

Herein, we demonstrate the continuous synthesis of highly stable PNCs by incorporating amphiphilic star-like block copolymer nanoreactors into a continuous flow reactor. Such amphiphilic star-shaped block copolymers are first synthesized by sequential atom transfer radical polymerization (ATRP) of brominated β -cyclodextrin macroinitiators. These nanoreactors are then loaded with perovskite precursors and introduced into a house-built flow reactor. The synthesis of PNCs was then optimized by first surveying the ideal antisolvent for high quality PNC formation. The injection flowrate of that antisolvent ($Q_{\text{antisolvent}}$) was then optimized at a fixed precursor solution injection rate ($Q_{\text{precursor}}$). Subsequently, an ideal $Q_{\text{precursor}}$ was determined by varying $Q_{\text{precursor}}$ with $Q_{\text{antisolvent}}$ held constant. Finally, the optical properties, morphology, and stabilities of the templated PNCs were compared to continuously-produced PNCs synthesized from conventional oleic acid and oleylamine (OA/OAm) ligands. Notably, the templated PNCs displayed a similar PLQY to and significantly enhanced colloidal, UV, and thermal stabilities over the control OA/OAm-co-capped PNCs.

3.2 Experimental Details

3.2.1 Materials

Toluene (ACS, VWR), dichloromethane (ACS, VWR), chlorobenzene (ACS, Beantown Chemical), chloroform (ACS, VWR), hexane (ACS, VWR), anhydrous dimethylformamide (DMF, Millipore), lead bromide (99.99%, TCI), cesium bromide (99.9%, STREM Chemicals), oleic acid (90%, Alfa Aesar), oleylamine (Technical grade, Sigma Aldrich), dichloromethane (>99.5%), α -bromoisobutyryl bromide (BiBB, 98%), anisole (99%), 2-butanone (99.0%), anhydrous dimethylformamide (DMF, >99.8%) anhydrous 1-methyl-2-pyrrolidinone (NMP, 99.5%), N,N,N',N',N''-pentamethyldiethylene triamine (PMDETA, 99%), trifluoroacetic acid (TFA, 99.9%), aluminum oxide powder (activated, neutral, ~325 mesh), tetrahydrofuran (THF, 99.0%), acetone (99.5%), deuterated chloroform (CDCl₃, 99.96%), and deuterated dimethylformamide (DMF-d₇, 99.5%) were purchased from Sigma-Aldrich and used as received.

Before bromination the β -cyclodextrin (β -CD, >97.0%, Sigma-Aldrich) were dried under vacuum for 48 hours at 60°C and azeotropically distilled in toluene for 2 hr at 120°C. Copper (I) bromide (CuBr, 98%, Sigma-Aldrich) was stirred in acetic acid for 2 hr, filtered, washed with ethanol and diethyl ether, and dried in vacuum at room temperature overnight. Styrene (St, 99.9%, Sigma-Aldrich), *tert*-butyl acrylate (*t*BA, 98%, Sigma-Aldrich) were distilled over CaH₂ under reduced pressure prior to use.

3.2.2 Methods

Synthesis of Heptakis[2,4,6-tri-O-(2-bromo-2-methylpropionyl)]- β -cyclodextrin (i.e., Br- β -CD macroinitiator): Purified β -CD (2.5 mmol) was first dissolved in 40 ml anhydrous NMP at 0°C. BiBB (105 mmol) was then added dropwise to the β -CD NMP solution and stirred for 1 hr. The reaction solution was then stirred at room temperature for an additional 24 hr to ensure completion. Next, the solution was diluted with 100 ml dichloromethane and washed with saturated NaHCO₃ aqueous solution and deionized water for at least three times, respectively. The product was recovered from the solution via rotary evaporation. The product was then re-dissolved in acetone, and the Br- β -CD acetone solution was added into water for crystallization to remove impurities. The precipitant was then dissolved in dichloromethane, dried with anhydrous MgSO₄, and filtered. All solvents were then removed via rotary evaporation to yield the final solid product.

Synthesis of hydrophobic star-like poly(*tert*-butyl acrylate) (star-like PtBA): The Br- β -CD was then used as a macroinitiator for atom transfer radical polymerization (ATRP) of *t*BA. Specifically, Br- β -CD, CuBr, PMDETA, 2-butanone, purified *t*BA (in the molar ratio= 1:1:1.5:1500:1500) were mixed in an ampoule, degassed by three freeze-pump-thaw cycles in liquid nitrogen, and placed in oil bath preheated at 60°C for a desired time. The polymerization was stopped by quenching in liquid nitrogen and exposure to ambient air. The reaction solution was then diluted with acetone, passed through a neutral activated aluminum oxide column to remove the copper catalyst, and precipitated with a

methanol/water (volume ratio= 1:1) mixture to obtain the final product. The completed star-like PtBA was then dried in a vacuum at room temperature for 48 hr.

Synthesis of hydrophobic star-like poly(tert-butyl acrylate)-block-polystyrene (star-like PtBA-b-PS): The star-like PtBA was then used as a macroinitiator to grow PS via ATRP. Star-like PtBA, CuBr, PMDETA, St and anisole (molar ratio=1:1:1.5:1200:2000) were mixed in an ampoule, degassed by three freeze-pump-thaw cycles in liquid nitrogen, and polymerized at 90°C for specific period of time. Afterwards, the reaction was quenched by immersing in liquid nitrogen and exposing to ambient air. The reaction solution was then diluted with THF, and passed through a neutral, activated aluminum oxide column to remove the copper catalyst. Subsequently, the final product was purified by precipitation with cold methanol and dried at 40°C under vacuum for 48 hours.

Synthesis of amphiphilic star-like poly(acrylic acid)-block-polystyrene (Star-like PAA-b-PS): To convert the PtBA to PAA, 200 mg star-like PtBA-b-PS diblock copolymers were added into 100 ml anhydrous dichloromethane and 2 ml TFA. The solution was then stirred for 24 hr at room temperature to ensure the hydrolysis of the PtBA. After hydrolysis, rotary evaporation was used to remove excess TFA, and a white-powder like product was obtained. This powder was then re-dissolved in DMF, precipitated with cold methanol, filtered, and dried at room temperature in vacuum overnight.

Construction of flow reactor

To create the flow reactor, 1.6 mm inner diameter PTFE tubing (from SCAT Europe) was cut to the 15cm. It was then fitted onto one end of a polypropylene/polyethylene tapered Y connector (VWR). Two pieces of PTFE tubing with one end adapted to female Luer Lock fitting (Hamilton Company) were then attached to the other two ends of the tapered connector. The female Luer Lock fittings allowed for facile connection to the syringes that contained the precursor (10mL BD) and crystallization (50mL Chemglass borosilicate) solvents, which were dispersed by the Single Syringe Pump (Fisherbrand). A schematic diagram of the flow reactor can be seen in **Figure S1**.

The same precursor solutions were used for all trials. The templated precursor solution was created by dissolving 10mg PAA-*b*-PS nanoreactor, 0.1mmol CsBr (20mg), and 0.1mmol PbBr₂ (36mg) in 20mL DMF. The control precursor solution was created by dissolving 0.1mmol CsBr (20mg), and 0.1mmol PbBr₂ (36mg), 0.5mL oleic acid, and 50 μL oleylamine in 20mL DMF.

Both control and templated PNCs were synthesized by loading the syringes with the solvents and flowing each at the desired rate. The completed PNCs were collected from the end of the reactor tube. The resulting CsPbBr₃ PNCs were then purified by centrifugation at 13k RPM for 10 minutes. The supernatant was collected, while any aggregates that had precipitated were discarded.

Calculation of Reynolds Number: The Reynolds number (Re) for all flowrates calculated using the equation below.

$$Re = \frac{\rho Q D}{\mu A}$$

Equation 4 – Reynolds number calculation

ρ = Density of fluid [kg/m³]

Q = Flowrate [m³/s]

D = Inner diameter of tube [m]

μ = Dynamic viscosity of liquid [Pa*s]

A = Cross sectional area of tube [m²]

Constants:

$$\rho = 867 \text{ kg/m}^3$$

$$D = 0.0016 \text{ m}$$

$$\mu = 5.83\text{E-}4 \text{ Pa s}$$

$$A = \pi (D/2)^2 = \pi (0.0008)^2 = 2.01\text{E-}6 \text{ m}^2$$

Conversion of Variable Flowrates:

$$Q = 5060 \text{ mL/hr} = 1.41\text{E-}6 \text{ m}^3/\text{s}$$

$$Q = 4060 \text{ mL/hr} = 1.13\text{E-}6 \text{ m}^3/\text{s}$$

$$Q = 3060 \text{ mL/hr} = 8.50\text{E-}7 \text{ m}^3/\text{s}$$

$$Q = 2060 \text{ mL/hr} = 5.72\text{E-}7 \text{ m}^3/\text{s}$$

$$Q = 1060 \text{ mL/hr} = 2.94\text{E-}7 \text{ m}^3/\text{s}$$

As an example, Re for total flowrate of 5060 mL/hr is given as follows:

$$Re = (870 \text{ kg/m}^3)(1.41\text{E-}6 \text{ m}^3/\text{s})(0.0016 \text{ m}) / (5.60\text{E-}4 \text{ Pa*s})(2.01\text{E-}6 \text{ m}^2) = 1662$$

Table 1 – Reynolds number corresponding to each flowrate in flow reactor

Total Flow ($Q_{\text{precursor}}+Q_{\text{tol}}$) (mL/hr)	<i>Re</i>
5060	1662
4060	1334
3060	1005
2060	677
1060	348

Calculation of radius of gyration of PAA block

$$\langle Rg^2 \rangle = \frac{Nb^2}{6} \left(\frac{3-\frac{2}{f}}{f} \right)$$

Equation 5 - Calculation of radius of gyration of PAA block¹⁷⁰

N is degree of polymerization of star-like PAA calculated from M_n f is the number of arms.

b is Kuhn length (0.69nm for PAA).¹⁷¹

$$N = \frac{273,000 \frac{g}{mol}}{72.06 \frac{g}{mol}} = 3788$$

$$\langle Rg^2 \rangle = \frac{3788 * (0.69nm)^2}{6} * \frac{3 - \frac{2}{21}}{21}$$

$$\langle Rg \rangle = 6.45 \text{ nm}$$

$$D = 12.9 \text{ nm}$$

Calculation of yield of (mass/time) of the dual-reactor system

The amount of synthesized CsPbBr₃ PNCs is calculated by determining the volume of all PNCs synthesized within the nanoreactor and then converting to mass using the density of CsPbBr₃. An explanation of each value is given below.

$$0.010g * \frac{mol}{651,000g} * \frac{1}{20mL} * \frac{60mL}{hr} * \frac{6.02*10^{23}}{mol} * \frac{4}{3}\pi(6.4 * 10^{-9}m)^3 * \left(\frac{4.55g}{cm^3}\right) * \left(\frac{100cm}{m}\right)^3 =$$

0.139 g/hr

Equation 6 – Calculation of yield of combined flow/nanoreactor

Mass of nanoreactor added / molar mass of PAA-*b*-PS nanoreactor / added volume of DMF * antisolvent flowrate * Avogadro's number * expected volume of each CsPbBr₃ PNC * density of CsPbBr₃ * unit conversion = expected yield

Note: Density of CsPbBr₃ is reported as 4.42 g/cm³.¹⁷²

Characterization

The molecular weights and polydispersity indexes of polymers were measured by gel permeation chromatography (GPC) equipped with a G1362A refractive detector and a G1314A variable wavelength detector, one 5 μm LP gel column (500 Å, molecular range: 500~2×10⁴ g/mol) and one 5 μm LP gel mixed bed column (molecular range: 200~3×10⁶ g/mol), and THF as mobile phase with a rate of 1.0 ml/min at 35°C. The GPC was

calibrated with monodisperse linear PS as standard. $^1\text{H-NMR}$ were measured using Varian mercury 400 nuclear magnetic resonance spectroscopy with either CDCl_3 or DMF-d_7 as solvent.

The photoluminescence (PL) spectra of the CsPbBr_3 PNCs was obtained by a PerkinElmer LS 55 fluorescence spectrometer with a 365nm excitation light. The absolute photoluminescence quantum yield (PLQY) was measured with a Hamamatsu Quantaaurus QY Plus with an excitation wavelength of 365 nm. The absorbance of the PNCs from 800-300 nm was examined with a Shimadzu UV-2600. The morphologies of the PNCs were investigated with a JEOL CX-II transmission electron microscope (TEM) operated at 100 keV.

3.3 Results and Discussion

As noted above, the use of amphiphilic star-like block copolymer nanoreactors is key to achieving highly stable PNCs. The nanoreactors were synthesized using methods from previous literature^{160-161, 173}, and detailed procedures to synthesize the star-like block copolymers are available in the **Section 5.2**. **Figure 8** depicts the route to PNCs by capitalizing on amphiphilic star-like block copolymer as nanoreactor. First, ATRP macroinitiators were synthesized by brominating β -cyclodextrin (β -CD) with α -bromoisobutyryl bromide (BiBB). Because β -CD possesses seven glucose subunits (and each of those has 3 OH groups), the final brominated β -CD will have 21 bromine terminals for ATRP initiation. Blocks of poly(*tert*-butyl acrylate) (*Pt*BA) were then grown via ATRP (upper third panel; **Figure 8**). Once the *Pt*BA blocks were grafted, polystyrene (PS) blocks were subsequently grown from the inner *Pt*BA blocks (upper right panel; **Figure 8**).

Afterwards, the inner *Pt*BA was hydrolyzed to form poly(acrylic acid) (PAA) (lower right panel; **Figure 8**). This step is necessary as PAA cannot be directly synthesized via ATRP because the carboxyl groups in PAA coordinate too strongly with the necessary copper catalyst, preventing any significant chain growth¹⁷⁴. The carboxyl groups on the inner PAA blocks have also been demonstrated to coordinate with metal moieties in nanocrystal precursors^{160-161, 164, 174-175}, which enables facile NC formation within the compartment occupied by PAA blocks of star-like PAA-*b*-PS block copolymer as nanoreactor. Proton nuclear magnetic resonance (¹H-NMR) spectra of each step of the process are shown in **Figure 9 a-d**. Characteristic peaks are visible for each new functionality at each step in the process: in **b** *t*BA peak is visible at 1.5ppm, in **c** styrene peaks are present at 6.3 to 7.3 ppm, and in **d** the creation of PAA is represented by the removal of the *t*BA peak at 1.5ppm and the present of hydroxy peaks at 12ppm. Gel permeation chromatography (GPC) traces in **Figure 10** further suggest successful synthesis as the polymer has been confirmed to increase in size. The complete 21 arm star-like polymer nanoreactors were then dissolved in DMF with perovskite precursors (i.e., PbBr₂ and CsBr) and stirred to allow for coordination of the precursors with the carboxylic acid groups in the PAA. Once loaded, PNCs can easily be produced (i.e., PS-capped PNC; lower left panel, **Figure 8**) by adding the nanoreactor/perovskite precursor solution (i.e., perovskite precursors-loaded nanoreactor; lower central panel, **Figure 8**) into a nonpolar antisolvent (e.g. toluene), spurring crystallization in a modified ligand-assisted reprecipitation (LARP) technique.

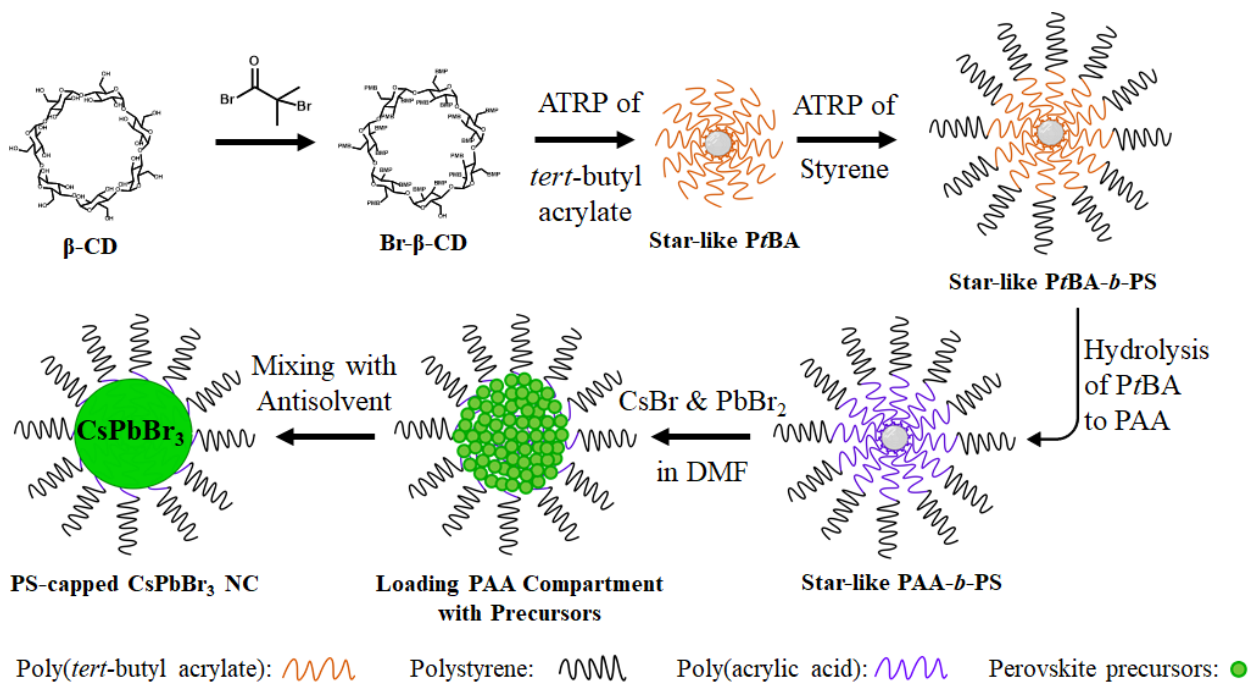


Figure 8 - Stepwise representation of route to star-like PAA-*b*-PS diblock copolymer nanoreactor and the resulting PS-capped CsPbBr₃ nanocrystal.

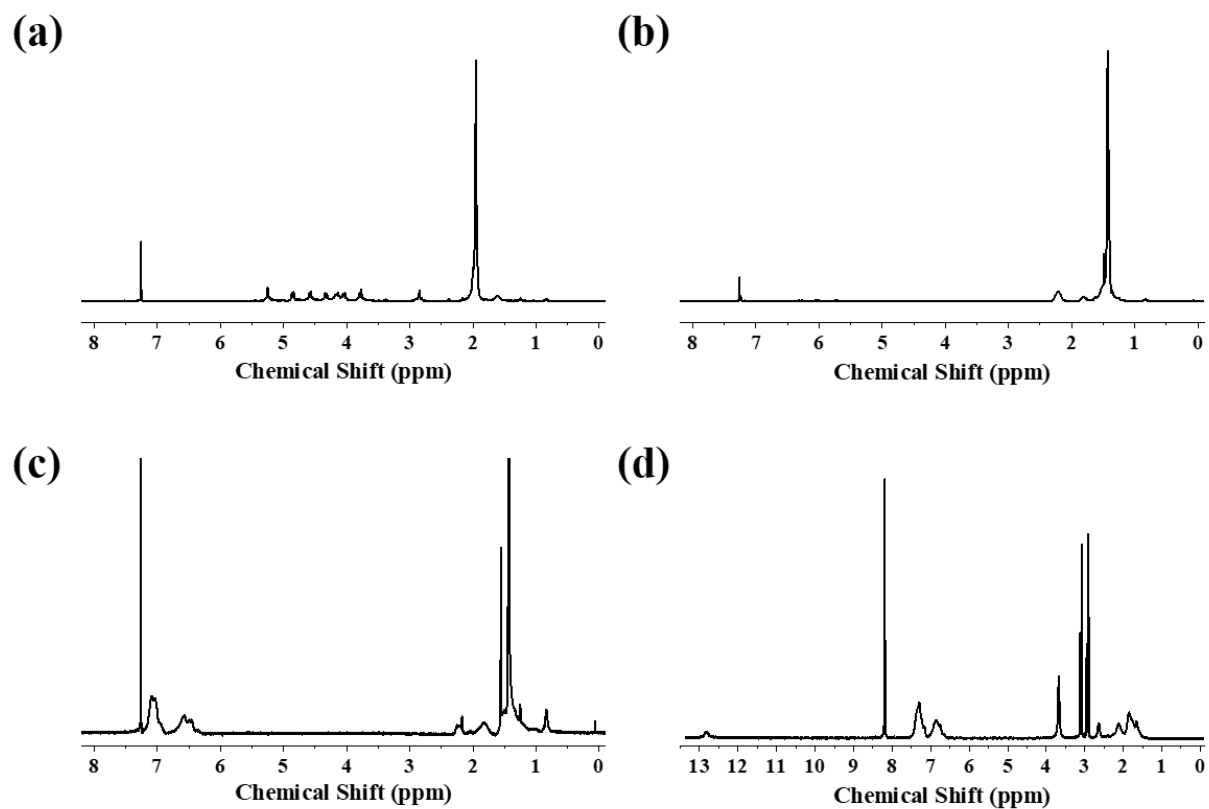


Figure 9 - NMR spectra from (a) brominated β -CD, (b) star-like PtBA, (c) star-like PtBA-*b*-PS, and (d) star-like PAA-*b*-PS.

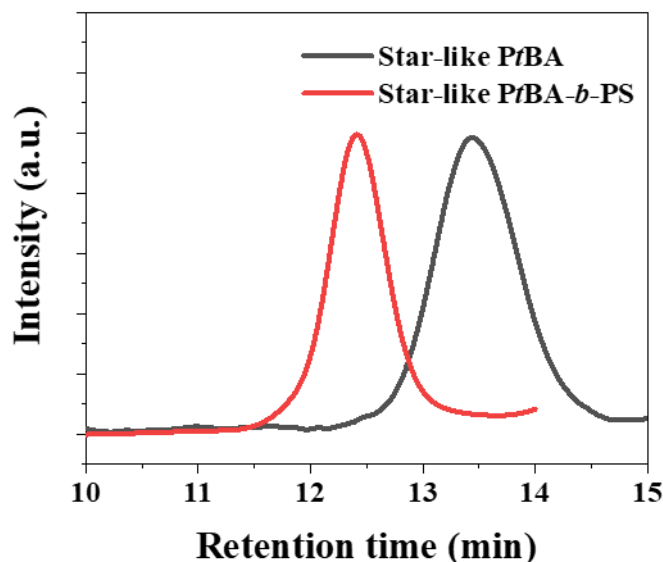


Figure 10 - GPC traces for star-like PtBA and PtBA-*b*-PS.

A variety of solvents were explored to determine the ideal antisolvent for PNC synthesis (i.e., CsPbBr₃). Using a modified LARP technique (noted above), 50 μ L preloaded nanoreactor solution was dropped into 10 mL vigorously stirring toluene, chlorobenzene, dichloromethane, chloroform, and hexane. The optical properties of the CsPbBr₃ PNCs yielded from this technique were then compared, as seen in **Table 2**. Using toluene as an antisolvent resulted in PNCs with the highest PLQY, followed by chlorobenzene and chloroform/dichloromethane. Using hexane as an antisolvent did not yield PNCs with any detectable emission. The vastly different properties from each antisolvent can be attributed to the polarity of solvent and interaction the outer PS ligands. The ionic crystal nature of perovskite renders them susceptible to be degraded in the presence of polar solvents¹⁷⁶, leading to the observed drop in PLQY with increasing polarity of solvents (from toluene (9.9) to chlorobenzene (18.8) to dichloromethane (30.9)/chloroform (25.9))¹⁷⁷. The lack of photoluminescent performance from PNCs made

with hexane can be ascribed to the fact that PS is insoluble in hexane¹⁷⁸. For the covalently-bonded outermost polymer block to be effective as permanent ligands, a favorable interaction with the solvent is necessary. As PS is not soluble in hexane, no colloidal nanoparticles could form, only aggregates of perovskite precursors. This small scale exploration verified that toluene is the best solvent to employ going forward in the flow reactor for continuous synthesis.

Table 2 - Optical properties of CsPbBr₃ PNCs synthesized via conventional LARP using various antisolvents.

Solvent	Solvent Polarity	PLQY (%)	Emission Peak (nm)
Toluene	9.9	51.3	507
Chlorobenzene	18.8	9.4	502
Dichloromethane	30.9	0.5	515
Chloroform	25.9	0.5	507
Hexane	0.9	0	-

To enable continuous production of CsPbBr₃ PNCs, a house-built flow reactor was constructed, as was reported in our previous work⁸⁹. A diagram of the flow reactor is depicted in **Figure 11**. It consists of two syringe pumps, with Luer lock PTFE tubing connected to the ends of the syringes (one for the precursor solution and another for the antisolvent), and a Y-connector that facilitates mixing of the two solutions. The operating

principal of this flow reactor is similar to that of LARP, yet instead of a magnetic stir bar, the mixing is accomplished by the flow dynamics at the Y-connector.

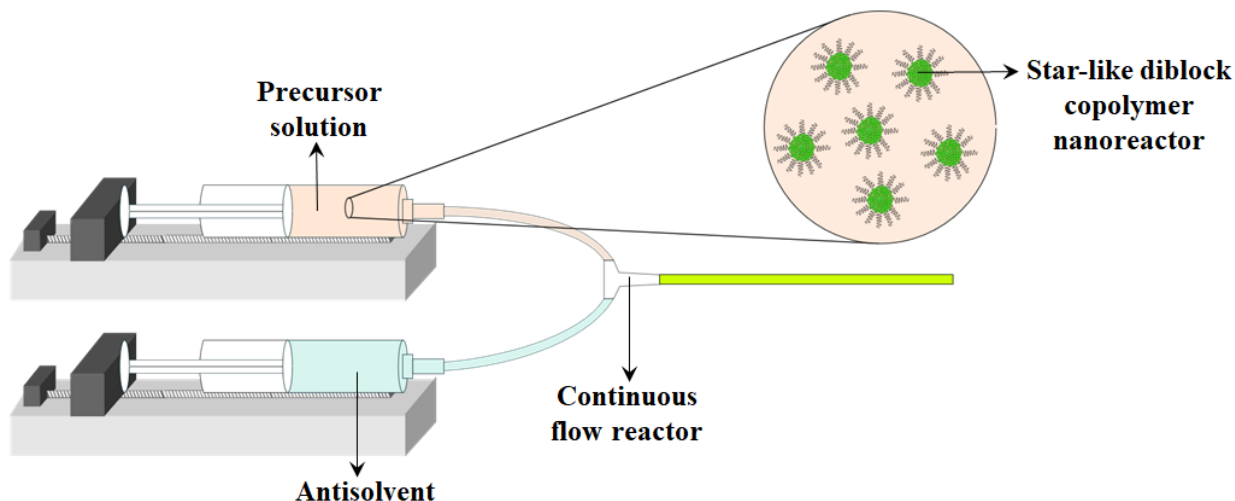


Figure 11 - Schematic diagram of dual flow/nano reactor apparatus.

After toluene was selected as the preferred antisolvent, the toluene flowrate (Q_{tol}) for both nanoreactor-enabled PNCs (i.e., PS-capped CsPbBr₃) and conventional ligand-assisted PNCs (i.e., OA/OAm-co-capped CsPbBr₃ as control sample; see *Experimental Section* in *Supporting Information*) was optimized by varying Q_{tol} and holding $Q_{precursor}$ at a constant 60mL/hr. For both types of CsPbBr₃ PNCs, a monotonic increase in PLQY was seen Q_{tol} increased from 1000 to 5000 mL/hr (**Figure 12a**). This increased PLQY can probably be attributed to the enhanced mixing of the precursors and antisolvent that occurs at higher flowrates of toluene. The rising flowrates result in an increase in the corresponding Reynolds number from 394 (for $Q_{tol} = 1000$ mL/hr) to 1662 (for $Q_{tol} = 5000$ mL/hr). The complete calculation of Reynolds number is shown in **Equation 4** and **Table 1**. The transition from laminar Poiseuille flow to turbulent flow in circular tubes is generally accepted to occur at a critical Reynolds number between 1,800 and 2,300¹⁷⁹⁻¹⁸⁰.

While the Reynolds number at the max flowrate still falls within the laminar flow range ($Re = 1,662 < 1,800$), the increasing flow has thus been found to promote better mixing¹⁸¹. It is notable that the conventionally-ligated PNCs (i.e., OA/OAm-co-capped CsPbBr₃) display a higher average PLQY than those synthesized with the nanoreactor. This is likely due to presence of the PAA blocks inside the template-grown PNCs.¹⁶¹ While these PAA chains are necessary for the formation of PNCs within the nanoreactor (due to their coordination with perovskite precursors), their presence could also introduce defects into the crystal structure, thus hindering PLQY¹⁶¹. The emission peak position of PS-capped PNCs was unaffected by Q_{tot} , whereas the OA/OAm-co-capped PNCs showed a general trend of decreasing peak position with increasing Q_{tot} (**Figure 12b**). The constant emission peak of PS-capped PNCs can be attributed to the good size control that the star-like PAA-*b*-PS nanoreactors enable. Because only the PAA blocks coordinate with the perovskite precursors, the size of the PNC is dictated by the length of the inner PAA blocks. The constant emission wavelength of PS-capped PNCs stands in contrast to conventional OA/OAm-co-capped PNCs, which show a general increase in emission peak position as Q_{tot} decreased. This red-shifted emission of OA/OAm-co-capped PNCs could be ascribed to an increase of defects in PNCs synthesized at lower flowrates. As discussed above, higher flowrates promote better mixing¹⁸¹, thus yielding more crystalline PNCs which lack defects that are known to promote red-shifting of emission¹⁸²⁻¹⁸³. We note that OA/OAm-co-capped PNCs made at $Q_{tot}=1000$ mL/hr do not match the trend seen for $Q_{tot}=2000$ though 5000 mL/hr. This difference may be due to the extremely low mixing that occurs at $Q_{tot}=1000$ mL/hr ($Re=394$).

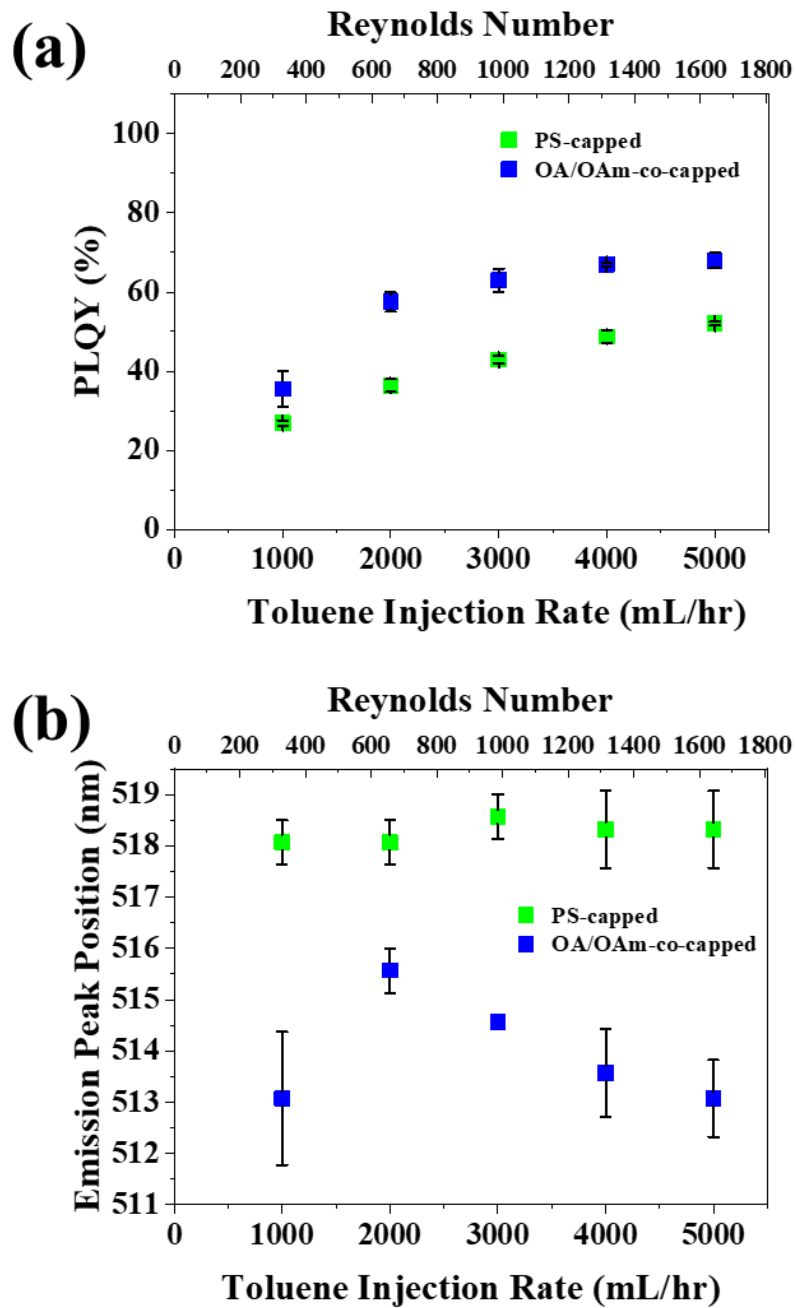


Figure 12 - (a) Effect of $Q_{toluene}$ on PLQY and (b) emission peak position of PS-capped CsPbBr₃ PNCs via capitalizing on star-like PAA-*b*-PS as nanoreactor and OA/OAm-co-capped CsPbBr₃ PNCs (control sample).

Following the highest Q_{tol} determined to be the most beneficial, we optimized $Q_{precursor}$. To this end, $Q_{precursor}$ was varied from 10 to 60 mL/hr, while keeping Q_{tol} constant at 5000 mL/hr. Varying $Q_{precursor}$ exerted little effect on the PLQY of either PS-capped or OA/OAm-co-capped CsPbBr₃ PNCs (**Figure 13a**). A relatively stable PLQY near 60% was evidenced for both template-grown and control PNCs, signifying that altering the precursor to antisolvent ratio has little impact on the crystal quality. The emission peak position of PS-capped PNCs was constant at all tested $Q_{precursor}$, yet the emission peak of OA/OAm-co-capped PNCs was seen to increase with increasing $Q_{precursor}$ (**Figure 13b**). This is likely due to the increasing precursor to antisolvent ratio, which favors larger PNCs, leading to less quantum-confinement. The full width of half maximum (FWHM) of the template-grown and control PNCs was relatively unaffected by altering $Q_{precursor}$ (**Figure 13c**). This suggests that the crystal quality of the PNCs was also unaffected, which is consistent with the stable PLQY observed.

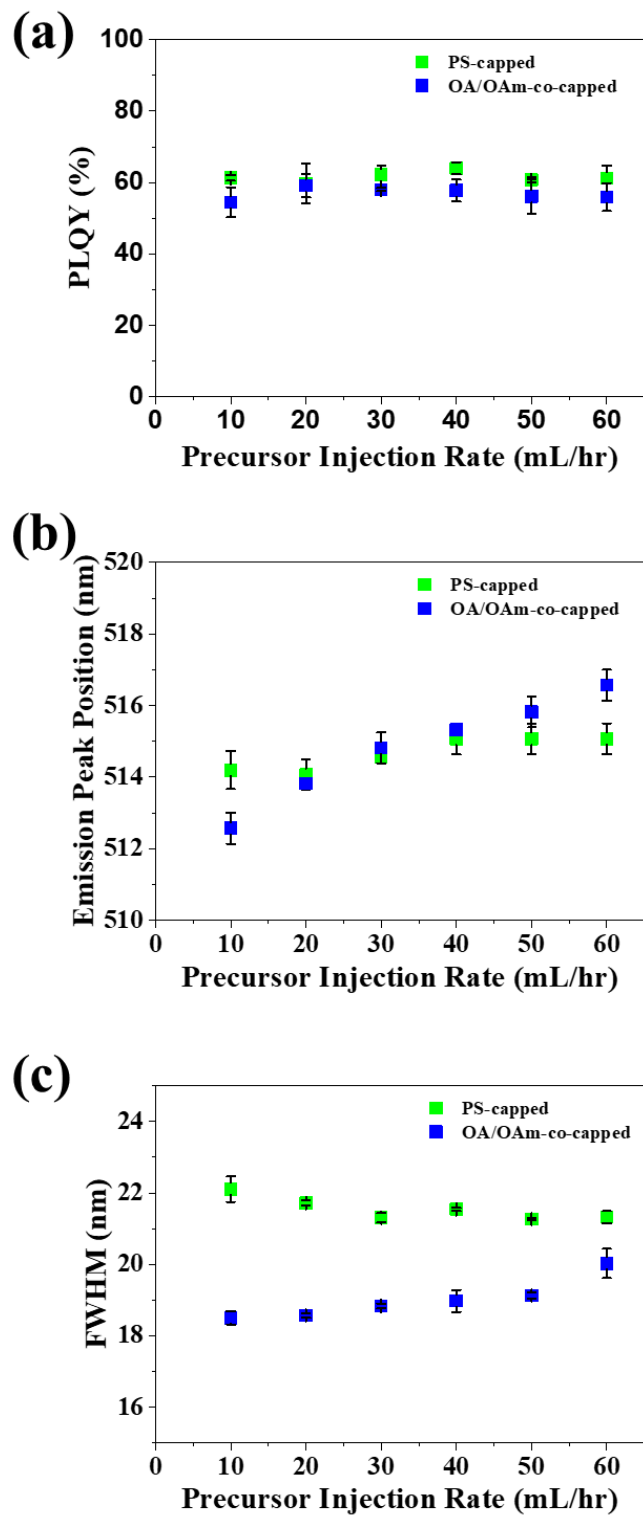


Figure 13 - Effect of $Q_{precursor}$ on (a) PLQY, (b) emission peak position, and (c) FWHM of PS-capped CsPbBr₃ PNCs and OA/OAm-co-capped CsPbBr₃ PNCs (control sample), where Q_{tol} was held constant at the optimized 5000 mL/hr.

With the optimized conditions (i.e., $Q_{tot}=5000$ mL/hr and $Q_{precursor}=60$ mL/hr to maximize production) for continuous production of PNCs identified, they were used to synthesize CsPbBr₃ PNCs for further characterization and stability testing. TEM images show that the PS-capped PNCs possessed an average diameter of 13.5nm (**Figure 14a**, **Figure 15a**), in good agreement with the calculated diameter using the equation developed in our prior work (**Equation 5**; the calculated radius of gyration R_g of star-like PAA blocks is 12.9 nm)¹⁷⁰. It is notable that past studies using the nanoreactor have shown that the equation often underestimates the size of the formed nanocrystals¹⁶¹. Notably, PS-capped PNCs formed by via the nanoreactor strategy are significantly smaller on average (13.5nm) than those formed with conventional OA and OAm ligands (22nm) (**Figure 14b**, **Figure 15b**), even though the amount of perovskite precursors and other experimental methods are identical. This manifests that the star-like PAA-*b*-PS nanoreactor restricts growth of PNC below that which may otherwise be favored. A control experiment was also conducted in which a solution of perovskite precursors (CsBr and PbBr₃) was loaded into the flow reactor without the presence of any organic ligands (i.e., no OA and OAm as well as no star-like PAA-*b*-PS nanoreactor). No luminescence was detected for the ligand-free CsPbBr₃. This offers further proof to suggest that any luminescent performance from template-grown PNCs can clearly be attributed to CsPbBr₃ formed within the nanoreactor.

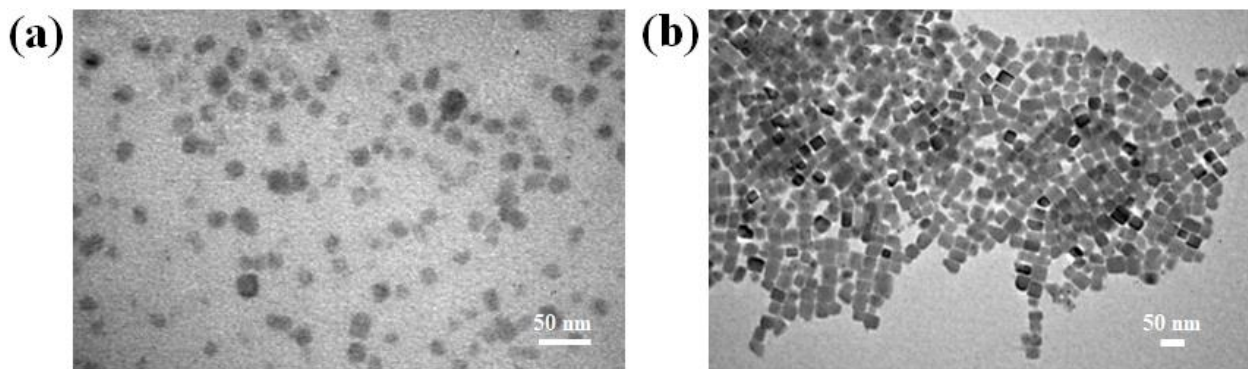


Figure 14 - TEM images of (a) PS-capped CsPbBr₃ PNCs and (b) OA/OAm-co-capped CsPbBr₃ PNCs (control sample). Both samples were synthesized at optimized conditions ($Q_{tol} = 5000$ mL/hr and $Q_{precursor} = 60$ mL/hr).

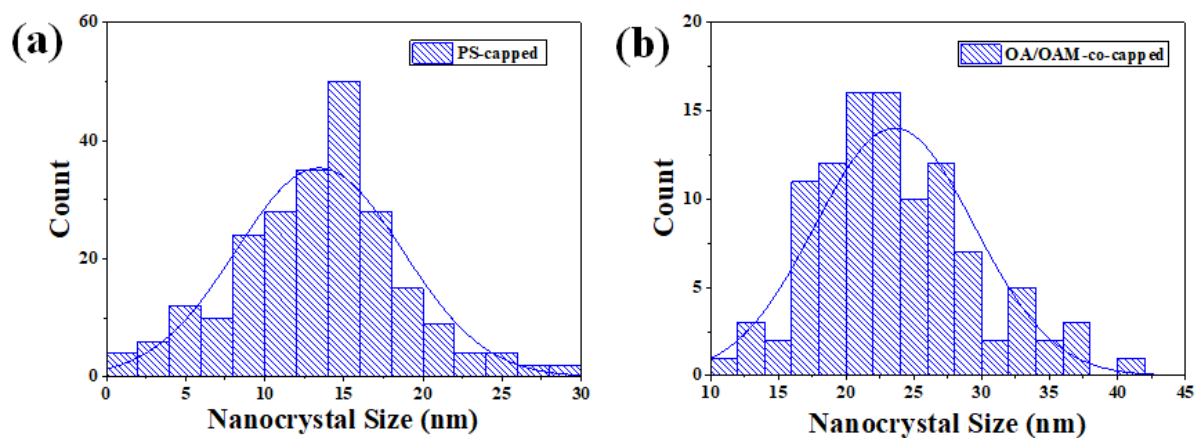


Figure 15 - Size distribution of (a) PS-capped CsPbBr₃ PNCs and (b) OA/OAm-co-capped CsPbBr₃ PNCs (control sample). Both samples were synthesized at optimized conditions ($Q_{tol} = 5000$ mL/hr and $Q_{precursor} = 60$ mL/hr).

The colloidal, UV, and thermal stabilities of control and templated CsPbBr₃ PNCs were then examined. In colloidal stability testing, the templated PNCs exhibited nearly no PLQY deterioration over more than 100 days, while the control falls to 20% normalized PLQY (**Figure 16a**). The significantly enhanced colloidal stability of the templated PNCs is due to their strongly ligated outer PS chains that are originally covalently bound to inner PAA chains. Conventional OA and OAm ligands are only dynamically bound to the surface of the PNC, and over time they can dissociate, leading to PNC agglomeration and quenching of luminescence⁸⁶. This is seen in the sharp decline of PLQY with time. Template-grown PNCs, on the other hand, have PS chains intimately and firmly ligated, ensuring that they maintain their colloidal nature and thus avoiding agglomeration and preserving their excellent optoelectronic properties. To probe UV stability, both control and templated samples were exposed to 365nm UV radiation for 48 hr. The control OA/OAm-co-capped PNCs experienced a significant PLQY degradation in 24 hr, while the templated PNCs retained ~80% of their initial PLQY (**Figure 16b**). The decrease in optoelectronic performance can be ascribed to UV-induced photo-oxidation of Pb in PNCs¹⁸⁴. The superior UV stability of the templated PNCs is likely owing to the outer PS chains on the nanoreactor. The aromatic groups in the chains are known to absorb UV light, which spares the inner perovskite from deleterious effects of UV irradiation¹⁸⁵. To delve into their thermal stability, the PNCs were exposed to 80 °C for an extended time. The templated PNCs maintained ~70% of their initial PLQY after 5 hr at elevated temperature, while the control decreased to ~40% after 1 hr, and then to ~10% after 5 hr (**Figure 16c**). The considerable increase in PLQY retention can be ascribed to the strongly ligated PS chains on the surface of PNC as discussed above. Unlike the dynamic OA and OAm ligands

on the control PNCs, such intimately and vigorously tethered PS chains do not dissociate at elevated temperature, thereby rendering the templated PNCs to maintain their form and ensure high PLQY¹⁸⁶.

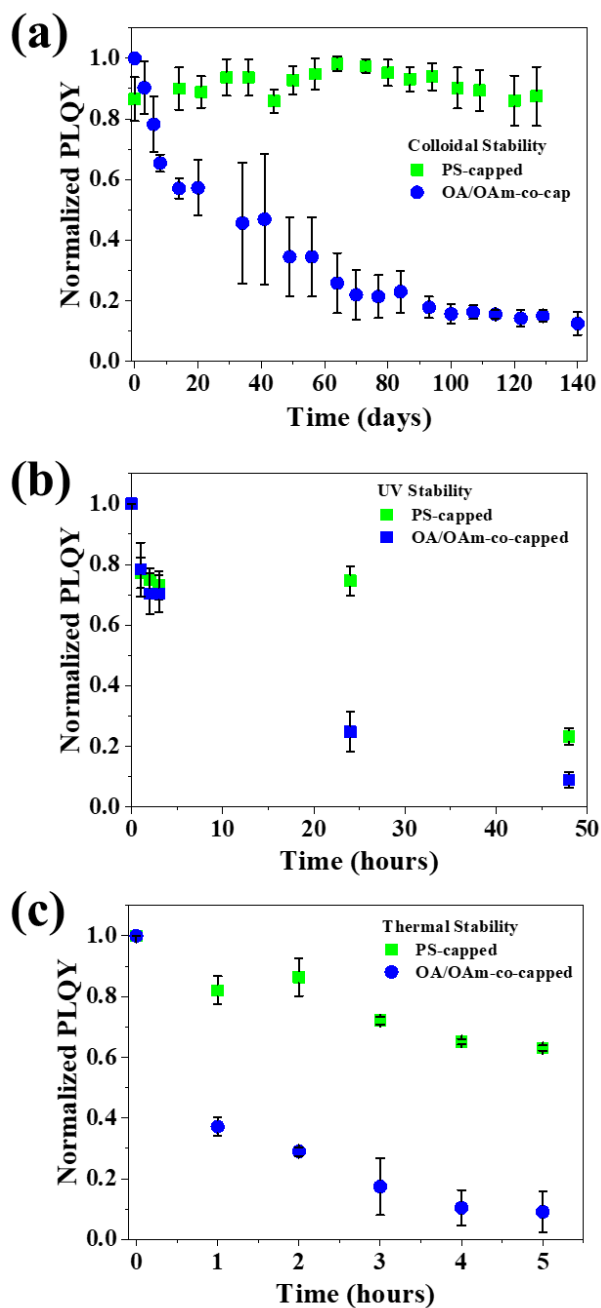


Figure 16 - (a) Colloidal, (b) UV, and (c) thermal (at 80 °C) stabilities of PS-capped and OA/OAm-co-capped CsPbBr₃ PNCs (control sample) synthesized at optimized conditions ($Q_{tol} = 5000$ mL/hr and $Q_{precursor} = 60$ mL/hr).

The yield of continuous manufacturing methods is a critical metric that informs the amount of a target material synthesized per time. In our dual-reactor technique (star-like

block copolymer nanoreactors inside a flow reactor), the final yield (mass/min) is dependent on the concentration of nanoreactors and perovskite precursors present in the precursor solution. Precursor solutions with higher concentrations of loaded nanoreactors will result in higher yields, whereas lower nanoreactor concentrations will lead to lower yields. In the trials in our study, the concentration of nanoreactors in the precursor solution was kept at a constant 10mg per 20mL DMF (perovskite precursors were added in slight excess). At this constant concentration, the calculated yield of CsPbBr₃ PNCs is 0.139 g/hr (see **Equation 6** in **Section 3.2**). This yield is similar to that previously reported for continuous production of perovskite (0.154 g/hr)⁸⁹ and is significantly more than previously reported batch conversion methods (0.019 g/hr)⁸⁹. Notably, the yield of this system scales linearly with the concentration of nanoreactors (**Equation 6** in **Section 3.2**). This linear dependence suggests that the yield of the system can be greatly boosted simply by increasing the concentration of loaded nanoreactors. Furthermore, varying the concentration of loaded nanoreactors in the precursor solution will impose insignificant effect on the optical properties on the final PNCs because little change in optical properties was observed as the precursor solution injection rate increased six times (**Figure 13a-c**).

3.4 Conclusion

In summary, we have demonstrated the continuous synthesis of highly stable PNCs by incorporating amphiphilic star-like block copolymer nanoreactors into a house-built flow reactor. The antisolvent composition, antisolvent flowrate, and precursor solution flowrate were each systematically optimized to render peak performance of the resultant nanocrystals. Importantly, toluene as an antisolvent, maximized antisolvent flowrate, and 60 mL/hr precursor solution flowrate were identified to the ideal parameters. The colloidal,

UV, and thermal stabilities of template-grown, PS-capped PNCs produced with these parameters were found to be vastly superior to that of PNCs made with conventional OA and OAm ligands. The strongly and firmly bound PS chains on the surface of PNCs account for enhanced stabilities over those of control samples where OA and OAm ligands are dynamically bonded to the surface. Such a dual-reactor system (nano and flow reactors) enables the markedly improved stabilities of PNCs from the nanoreactor in conjunction with the scaling up rendered by a continuous flow reactor, representing a crucial step towards commercialization of PNCs as it overcomes two of the great challenges facing this unique class of material. Future work can be centered on expanding the compositions and emission wavelengths of PNC emitters via this dual-reactor system.

CHAPTER 4. CONTINUOUS PRODUCTION OF ULTRATHIN ORGANIC-INORGANIC RUDDLESDEN-POPPER PEROVSKITE NANOPLATELETS VIA A FLOW REACTOR

Biesold, G. M., Liang, S., Wagner, B. K., Kang, Z., & Lin, Z. (2021). *Nanoscale*, 13(30), 13108-13115.

4.1 Introduction

Due to their unique optoelectronic properties, colloidal semiconductor nanocrystals represent an exciting class of nanomaterials with a multitude of applications. Perovskite nanocrystals, with the general structure ABX_3 (where A = monovalent cation (e.g., $CH_3NH_3^+$, $CH_5N_2^+$, Cs^+ , etc.), B = bivalent cation (e.g., Pb^{2+} , Sn^{2+} , etc.), and X = halide anion (Cl^- , Br^- , or I^-))¹⁴², are particularly intriguing owing to their defect tolerance,¹⁴⁸ high photoluminescence quantum yield,^{38-40, 145} narrow emission bandwidth,^{37, 146} and direct and easily-tunable bandgap.¹² These outstanding optoelectronic properties have led to a diverse array of applications, including solar cells,¹⁸⁷⁻¹⁹⁰ light emitting diodes,^{162, 191} and photodetectors.¹³⁻¹⁴ Two dimensional (2D) and quasi-2D organic-inorganic Ruddlesden-Popper (RP) perovskites have recently emerged as an intriguing subclass of perovskites. RP perovskites, with the general formula $L_2[ABX_3]_{n-1}BX_4$ (where L=bulky alkylammonium cation (e.g., phenylethylammonium (PEA),¹⁹² butylammonium (BA),¹⁹³ octylammonium (OA),¹⁹⁴ etc.), are formed when bulky organic spacer cations (i.e., L) are placed at the monovalent A cation site.¹⁹⁵⁻¹⁹⁶ A variety of L have been employed, including linear (e.g., BA¹⁹³ and OA¹⁹⁴), phenyl (e.g., PEA¹⁹² and 1-naphthylmethylammonium¹⁹⁷), and bication (e.g., diammonium butane¹⁹⁸ and diammonium octane¹⁹⁸) architectures. As L is too large to fit within the ABX_3 structure, it necessitates the formation of thin nanosheets. The thickness of RP perovskite is defined as n, which equals the number of layers of corner

sharing octahedra. As n decreases, RP perovskites experience enhanced quantum confinement, which results in a dramatically blue-shifted emission^{194, 199} and an ultra-narrow full width at half max (FWHM).¹⁹⁹ The PLQY of perovskite NCs has, however, been found to decrease with decreasing thickness.^{194, 200} Notably, even with this decreased PLQY, the blue emission of (PEA)₂PbBr₄ NCs is greater than that of Cl-containing perovskites (<10%).²⁰¹ The blue-shifted emission is of particular interest, as blue-emitting 3D perovskites (e.g., ABX₃) are known to suffer from poor stability and possess suboptimal photoluminescence (PL) characteristics.²⁰²⁻²⁰⁴ Compared to 3D perovskites, RP perovskites possess a larger exciton binding energy due to low dielectric screening from the organic cation in conjunction with the confinement of electrons and holes within the 2D inorganic lattice.²⁰⁵⁻²⁰⁷ Additionally, the hydrophobic nature of the ionically-bound L affords enhanced environmental stability to the 2D RP perovskites.^{206, 208} For example, (PEA)₂FA _{$n-1$} Sn _{n} I _{$3n+1$} -based solar cells maintained their full power conversion efficiency after over 100 hr. in air without encapsulation.²⁰⁹ As such, 2D RP perovskites have been implemented for a diverse set of optoelectronic applications, including solar cells,^{153, 210} LEDs,²¹¹⁻²¹² and photodetectors.^{16, 213-214}

While perovskites have demonstrated great promise for numerous applications, currently perovskite nanocrystals are often created via batch synthetic techniques such as ligand-assisted reprecipitation (LARP)¹⁵⁶ and hot injection.⁶⁵ For perovskite NCs to reach their potential for widespread use, large-scale continuous production is highly desirable.²¹⁵⁻²¹⁶ Successes in the use of flow reactors for the continuous production of a variety of other semiconductor NCs^{93, 217} have spurred some study into the use of flow reactors to synthesize 3D perovskite NCs. Recently, microfluidic flow systems have been used to

probe the formation mechanisms of CsPbX₃^{165, 218-219} and FAPbX₃²²⁰ NCs. In these studies, precursor solutions were isolated into droplets within an inert oil medium, which enabled complete mixing within a confined area. Using these microfluidic droplets, crystal growth for lead halide perovskites was shown to be complete within seconds of precursor mixing.²¹⁹ A Couette-Taylor flow system was also utilized to produce Cs₄PbBr₆ NCs.¹⁶⁸ In this study, a precursor solution was combined with an antisolvent within the flow created between two spinning concentric cylinders.¹⁶⁸ This Couette-Taylor flow system was found to yield NCs with narrow FWHM and high photoluminescence quantum yield (PLQY) compared to those synthesized via conventional batch LARP approach. Notably, conventional flow reactor systems have also been explored. MAPbX₃ NCs were produced by continuously flowing two precursor solutions together.²¹⁷ The resulting NCs were, however, only stable for up to an hour in their native solvent. A PTFE microreactor was used to continuously create CsPbX₃ NCs. This strategy was able to create NCs with emission spanning 750-700nm, yet required the use of a convection micromixer and elevated temperature.²²¹ A 3D printed nozzle was incorporated into a flow reactor to enhance mixing and craft MAPbX₃ NCs.²²² Interestingly, as demonstrated by both experimental and simulation results, by adding the precursor solution into the antisolvent through a narrowed 3D-printed nozzle, crystallization was improved, which in turn enhanced the PL properties of the NCs.²²²

Herein, we report the continuous manufacturing of high-quality (as defined by PLQY, FWHM, and emission peak position comparable to those previously reported) 2D RP perovskite NCs (i.e., (PEA)₂PbX₄ nanoplatelets (NPLs); X = Br and I; n = 1) via a house-built flow reactor. To our knowledge, no previous study has reported the continuous

production of 2D RP NPLs. It is noteworthy that our flow reactor is able to produce NCs at rates over 15 times that previously reported.²²² Additionally, the relatively simple construction enables its widespread use without specialized equipment, unlike reactors that need relatively complex Couette-Taylor¹⁶⁸ or convection micromixer²²¹ apparatus. Furthermore, our flow reactor utilizes only two liquids, that is, the precursor solution and the antisolvent. This stands in sharp contrast to microfluidic platforms that necessitate the use of a third immiscible solvent as the media to separate reactor droplets.^{165, 218-220} It is also notable that by introducing only two liquids, our flow reactor products can be used directly after synthesis, thereby dispensing with the need for removal of the third immiscible solvent, which is important for future industrial production. The effects of antisolvent composition, reactor tube length (l), antisolvent flowrate (Q_{anti}), and precursor solution flowrate ($Q_{precursor}$) on the PL properties (i.e., PLQY, FWHM of emission, emission peak position, absorbance, etc.) and morphology of $(\text{PEA})_2\text{PbX}_4$ NPLs produced by flow reactor were elucidated. The antisolvent composition was witnessed to exert the greatest influence on the PL properties of the as-synthesized NPLs, with increasing polarity of the solvents leading to a consistent drop in PLQY. Reactor tube length and $Q_{precursor}$ were also identified to impact PLQY, with shorter reactor tubes and lower $Q_{precursor}$ generally resulting in better optoelectronic properties. Q_{anti} was not found to significantly affect the final NPLs. The optimized parameters yielded NPLs with absolute PLQYs of 18.5% for $(\text{PEA})_2\text{PbBr}_4$ and 1.5% for $(\text{PEA})_2\text{PbI}_4$, which are comparable to those reported for LARP synthesis.^{194, 213, 223-224} 2D perovskites have been observed to possess lower PLQY than their 3D counterparts due to fast free exciton quenching via exciton–phonon coupling.²²⁵ The flow reactor enables production rates of 0.1542 g/hr for $(\text{PEA})_2\text{PbBr}_4$,

which is at least eight times greater than that from batch synthesis. While flow reactors have been reported for 3D ABX_3 perovskites, to our knowledge, this is the first study on the continuous production of 2D RP perovskite NPLs. As such, it represents an important endeavor towards commercialization of this class of nanomaterials and offers a promise for the continuous production of other layered perovskites.

4.2 Experimental Details

4.2.1 Materials

All materials were used as received. Toluene (ACS, VWR), dichloromethane (ACS, VWR), chlorobenzene (ACS, Beantown Chemical), anhydrous dimethylformamide (DMF, Millipore), lead bromide (99.99%, TCI), lead iodide (99.9985%, Alfa Aesar), phenylethylamine (99%, Alfa Aesar), hydrobromic acid (48 wt%, Alfa Aesar), hydroiodic acid (57 wt%, Beantown Chemical), 1-octylamine (99%, Alfa Aesar), diethyl ether (ACS, Millipore Sigma), ethanol (200 proof, Koptec), phenylethylammonium bromide, phenylethylammonium iodide (synthesis details follow)

Phenylethylammonium halide (PEAX) was synthesized in a previously-reported method.¹⁹⁴ In short, excess halide acids were dropped into an ethanol/phenylethylamine mixture at 0 C. The mixture was then washed with diethyl ether three times, recrystallized with ethanol, and dried in a vacuum oven before use.

4.2.2 Methods

Flow reactor setup

To create the flow reactor, 1.6 mm inner diameter PTFE tubing (from SCAT Europe) was cut to the desired reactor tube length (15, 30, or 60 cm). It was then fitted onto one end of a polypropylene/polyethylene tapered connector (orifice size 3mm, VWR). Two pieces of PTFE tubing (inner diameter 1.6 mm) with one end adapted to female Luer Lock fitting (Hamilton Company) were then attached to the other two ends of the tapered connector. The female Luer Lock fittings allowed for facile connection to BD syringes that contained the precursor and crystallization solvents, which were dispersed by the Single Syringe Pump (Fisherbrand). A schematic diagram of the flow reactor can be seen in **Figure 17c**.

The same precursor solution was used for all trials except for those testing concentration effect of the precursor solution (described below). The general precursor solution was created by dissolving 0.4 mmol PbX_2 (X= Br, I), 0.8 mmol PEAX, and 12 μL octylamine in 10 mL DMF. The small amount of octylamine was added to passivate any surface defects on the NPLs. The concentration effect precursor solution was made by dissolving 0.8 mmol PbX_2 , 1.6 mmol PEAX, and 24 μL octylamine in 10 mL DMF.

Investigation of each parameter

The synthesis of perovskite nanoplatelets in the flow reactor was optimized by systematically tuning the following parameters.

Antisolvent: To isolate the effect of antisolvent, a 15 cm reactor tube and two Luer Lock fitted tubes were connected to the Y adaptor. One syringe was filled with precursor solution (described above) and the other syringe was filled with the antisolvent (either toluene, dichloromethane, or chlorobenzene). The precursor solution was then allowed to flow at 30 mL/hr until it reached the Y connector, at which point the antisolvent was introduced to flow at 1200 mL/hr. The final solution was collected from the end of the 15 cm reactor tube. The antisolvent syringe was removed and the reactor was rinsed with 10 mL of the antisolvent. This procedure was repeated two times for $Q_{precursor} = 30$ mL/hr. Each other $Q_{precursor}$ (5, 10, 15, 20, 25, and 30 mL/hr) was then tested 3 times. This entire procedure was followed for each antisolvent (chlorobenzene, dichloromethane, and toluene)

Reactor tube length: To elucidate the effect of reactor tube length, a 15 cm reactor tube and two Luer Lock fitted tubes were connected to the Y adaptor. One syringe was filled with precursor solution (described above) and the other syringe was filled with the toluene (antisolvent). The precursor solution was then allowed to flow at 30 mL/hr until it reached the Y connector, at which point the antisolvent was allowed to flow at 1200 mL/hr. The final solution was collected from the end of the 15 cm reactor tube. The antisolvent syringe

was removed and the reactor was rinsed with 10 mL of the antisolvent. This procedure was repeated two times for $Q_{precursor} = 30$ mL/hr. Each other $Q_{precursor}$ (5, 10, 15, 20, 25, and 30 mL/hr) was then tested 3 times. The entire procedure was then repeated after the reactor was replaced with a 30 and 60 cm tube.

Antisolvent flowrate: To investigate the effect of antisolvent flowrate, a 15 cm reactor tube and two Luer Lock fitted tubes were connected to the Y adaptor. One syringe was filled with precursor solution (described above) and the other syringe was filled with toluene (antisolvent). The precursor solution was then enabled to flow at 5 mL/hr until it reached the Y connector, at which point the antisolvent was flowed at 1200 mL/hr. The final solution was collected from the end of the 15 cm reactor tube. The antisolvent syringe was removed and the reactor was rinsed with 10 mL of the antisolvent. This procedure was repeated three times for each Q_{tol} (1200, 900, 720, 600, 514 mL/hr).

Precursor concentration:

To isolate the effect of precursor solution concentration, a 15 cm reactor tube and two Luer Lock fitted tubes were connected to the Y adaptor. One syringe was filled with the concentrated precursor solution (described above) and the other syringe was filled with toluene. The precursor solution was then allowed to flow at 30 mL/hr until it reached the Y connector, at which point the toluene was introduced to flow at 1200 mL/hr. The final solution was collected from the end of the 15 cm reactor tube. The toluene syringe was

removed and the reactor was rinsed with 10 mL of toluene. This procedure was repeated two times for $Q_{precursor} = 30$ mL/hr. Each other $Q_{precursor}$ (5, 10, 15, 20, 25, and 30 mL/hr) was then tested 3 times.

Characterization

The photoluminescence (PL) spectra of each 2D RP perovskite NPL was obtained by a PerkinElmer LS 55 fluorescence spectrometer with a 365nm excitation light. The absolute photoluminescence quantum yield (PLQY) was measured with a Hamamatsu Quantaurus QY Plus with an excitation wavelength of 365 nm. The absorbance of the NPLs was examined by 800-300 nm with a Shimadzu UV-2600. The morphologies of the as-prepared NPLs were investigated with a JEOL CX-II transmission electron microscope (TEM) operated at 100 keV. Atomic force microscopy was conducted with a Bruker Dimension Icon; operated in tapping mode. Samples for AFM were made by drop casting NPL solution onto a silicon substrate. We note that x-ray diffraction studies were not conducted because the monolayer structure of $n=1$ perovskites lacks sufficient periodicity to yield relevant results.¹⁹⁴

Estimation of batch synthesis production rate

Precursor solution composition:

0.8 mmol PEABr = 0.1617 g

0.4 mmol $\text{PbBr}_2 = 0.1468 \text{ g}$

10 mL DMF

Total weight per volume = $0.3085 \text{ g} / 10 \text{ mL} = 0.03085 \text{ g/mL}$

LARP synthesis ratio: 10 mL toluene: 10 uL precursor solution (10 uL = 0.010 mL)

Weight per batch: $0.010 \text{ mL} * 0.03085 \text{ g/mL} = 0.0003 \text{ g}$

*Assume 1 batch takes 60 seconds *

$0.0003 \text{ g} / 60 \text{ s} * (60 \text{ s} / \text{min}) * (60 \text{ min} / \text{hr}) = \underline{\underline{0.0185 \text{ g/hr}}}$

Equation 7 – Estimation of yield of batch synthesis

Calculation of production rate of continuous flow reactor

Precursor solution composition:

0.8 mmol PEABr = 0.1617 g

0.4 mmol $\text{PbBr}_2 = 0.1468 \text{ g}$

10 mL DMF

Total weight per volume = $0.3085 \text{ g} / 10 \text{ mL} = 0.03085 \text{ g/mL}$

Optimized Precursor Solution Injection Rate: 5 mL/hr

Therefore, half mass is distributed per hour, yield would be **0.1542 g/hr**

Equation 8 – Calculation of yield of continuous flow reactor

Reynolds Number Calculation

$$Re = \frac{\rho Q D}{\mu A}$$

Equation 9 – Reynolds Number Calculation

ρ = Density of fluid [kg/m³]

μ = Dynamic viscosity of liquid [Pa*s]

Q = Flowrate [m³/s]

A = Cross sectional area of tube [m²]

D = Inner diameter of tube [m]

Constants

ρ = **870 kg/m³**

μ = **5.60E-4 Pa s**

D = **0.0016 m**

A = $\pi(D/2)^2 = \pi(0.0008)^2 = \mathbf{2.01E-6 m^2}$

Variable Flowrates:

1205 mL/hr = **3.35E-7 m³/s**

519 mL/hr = 1.44E-7 m³/s

905 mL/hr = 2.54E-7 m³/s

725 mL/hr = 2.01E-7 m³/s

605 mL/hr = 1.68E-7 m³/s

Determination of Re for total flowrate of 1205 mL/hr

$$Re = (870 \text{ kg/m}^3)(3.35\text{E-}7 \text{ m}^3/\text{s})(0.0016 \text{ m}) / (5.60\text{E-}4 \text{ Pa}\cdot\text{s})(2.01\text{E-}6 \text{ m}^2) = \underline{393}$$

The Reynolds number for all flowrates was calculated using the above equation. The results are provided in the table below.

Table 3 – Reynolds number corresponding to various antisolvent injection rates

Total Flow [mL/hr]	Re
1205	393
905	295
725	236
605	197
519	169

4.3 Results and Discussion

Figure 17 a-b depict the chemical structures of 3D ABX₃ and 2D L₂PbX₄ perovskite, respectively. The bulky organic cation, L, possesses a linear structure, where L cations can have diverse structures (i.e., phenyl rings, branches, and other functionalities).^{192-194, 197-198,}

²⁰⁶ To facilitate the continuous synthesis of high-quality 2D (PEA)₂PbX₄ perovskite NPLs, a custom flow reactor was built in house, as illustrated in **Figure 17c**. Full details of its

construction can be found in the *Experimental Section* in the Supporting Information. Briefly, three PTFE tubes (3.2 mm inner diameter) were attached to a Y adaptor (3mm orifice size). Two ends were fitted to syringe pumps and the other was left open. Precursor solution and antisolvent were then pumped through the tubing, combining in the Y adaptor and then the final product was collected at the end of the open tube. To optimize the synthesis of $(\text{PEA})_2\text{PbX}_4$ NPLs, four parameters were tuned in the flow reactor, that is, antisolvent composition, reactor tube length, antisolvent flowrate, and precursor solution flowrate.

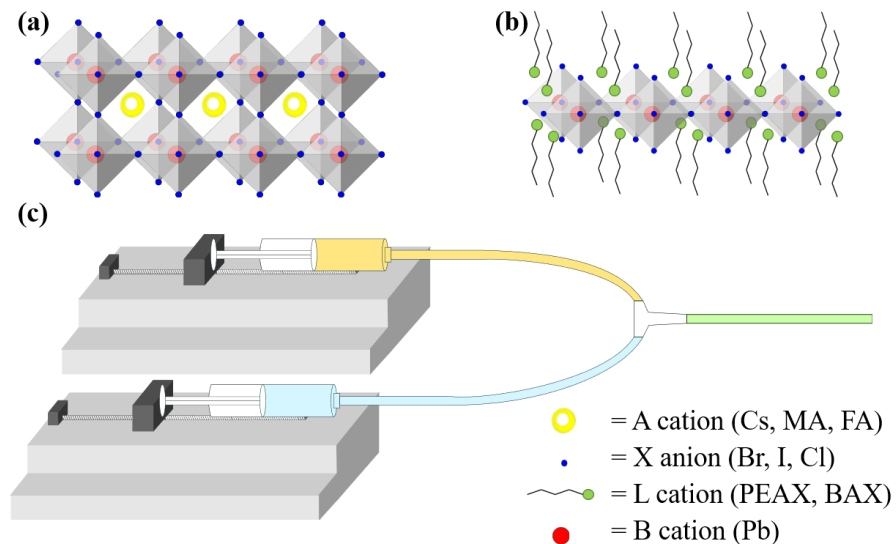


Figure 17 - Schematic of (a) three-dimensional ABX_3 perovskite crystal structure, and (b) typical $n=1$ L_2PbX_4 Ruddlesden-Popper perovskite structure. (c) Schematic of in-house built flow reactor, where precursor solution and antisolvent are introduced separately via respective syringe pumps.

I. Investigation into the Effect of Antisolvent

The first parameter that was tailored was antisolvent composition. In a typical LARP synthesis of perovskite NPLs, a solution of perovskite precursors (i.e., PEAX and PbX₂) dissolved in a polar solvent (e.g., dimethylformamide or dimethyl sulfoxide) is dropped into a vigorously stirred antisolvent that instantaneously triggers crystallization of the perovskite.¹⁵⁶ In contrast, the flow reactor uses a modified LARP technique, where instead of precursor solution being dropped into a stirring antisolvent, the precursor solution is pumped into a reactor tube while simultaneously pumping abundant antisolvent. The flow in the tube is then responsible for mixing the solution, rather than stirring in batch synthesis. In our study, following previously-reported LARP techniques, toluene, dichloromethane (DCM), and chlorobenzene were chosen as antisolvents in the flow reactor.²²⁶ These three solvents were selected to isolate the effects of their structure and polarity on the final NPLs. Toluene and chlorobenzene are chemically identical except for the substitution of Cl for a methyl group. Comparison of NPLs synthesized with these two solvents renders evaluation of how the introduction of a single Cl group alters NPLs. Furthermore, dichloromethane was adopted as it offers a relatively higher polarity and the absence of a phenyl ring. To examine the effect of antisolvent composition, the antisolvent flowrate (Q_{anti}) was set to a constant 1200 mL/hr, the reactor tube length fixed as 15 cm, and the precursor solution flowrate ($Q_{precursor}$) varied from 5 to 30 mL/hr. Transmission electron microscopy (TEM) images of (PEA)₂PbBr₄ NPLs produced with toluene antisolvent are shown in **Figure 18a-f**. TEM images of the chlorobenzene and dichloromethane trials can be seen in **Figure 19a-f** and **Figure 20a-f**, respectively. The NPL size distribution and average corner to corner length of NPLs made from both toluene

and chlorobenzene can be seen in **Figure 21/**Figure 22 (toluene) and **Figure 23/**Figure 24 (chlorobenzene). The average size and distribution of toluene NPLs was generally found to decrease with decreasing $Q_{\text{precursor}}$, which could be attributed to the relatively smaller amounts of precursors available for crystallization at low $Q_{\text{precursor}}$ flowrates (**Figure 22**). Notably, this trend was not seen for the average size and distribution of chlorobenzene crafted NPLs, which had a relatively constant average size of 2 μm (**Figure 24**). This could be due to the higher saturation limit of chlorobenzene, which would allow for more dissolution of the perovskite precursors.²²⁶ We note that trends between morphology and $Q_{\text{precursor}}$ are difficult to determine in DCM trials because of the potential decomposition of NPLs caused by DCM, as discussed below. As such, no NPL size measurements were taken for DCM samples. Interestingly, antisolvent composition was found to dramatically affect the quality of the produced $(\text{PEA})_2\text{PbBr}_4$ NPLs, as evidenced by the decreasing PLQY (**Figure 18g**). NPLs crafted with solvents of a relative lower polarity were seen to exhibit higher PLQY. The relative polarities for toluene, chlorobenzene, and dichloromethane are 0.09, 0.188, and 0.309, respectively.²²⁶⁻²²⁷ It is commonly reported that, because of their ionic nature, perovskite NCs can easily be degraded by polar solvents.^{148, 228} Thus, NPLs synthesized in relatively more polar solvents could be degraded, which would negatively impact their PLQY. This degradation can qualitatively be seen in differences of morphology of the NPLs. The TEM images of NPLs formed from toluene (**Figure 18a-f**) reveal more uniform NPLs compared to those of NPLs formed from chlorobenzene (**Figure 19a-f**) and DCM (**Figure 20a-f**). The samples made from DCM manifested clear degradation and often no NPL morphologies, which could be expected from its highest relative polarity. Antisolvent composition was found to have little effect

on the emission wavelength or FWHM of NPLs (**Figure 18h & i**), which is consistent with the fact that only $n=1$ $(\text{PEA})_2\text{PbBr}_4$ NPLs can form in the system, given the restrictive precursors.¹⁹⁹ The monolayer nature (and thus strong quantum confinement) of the NPLs ensured that the peak emission wavelength of all samples remained constant, as discussed later. This was further verified by absorbance and photoluminescence spectroscopy. **Figure 25** clearly show the absorbance and emission from the NPLs remains unchanged regardless of the composition antisolvent.

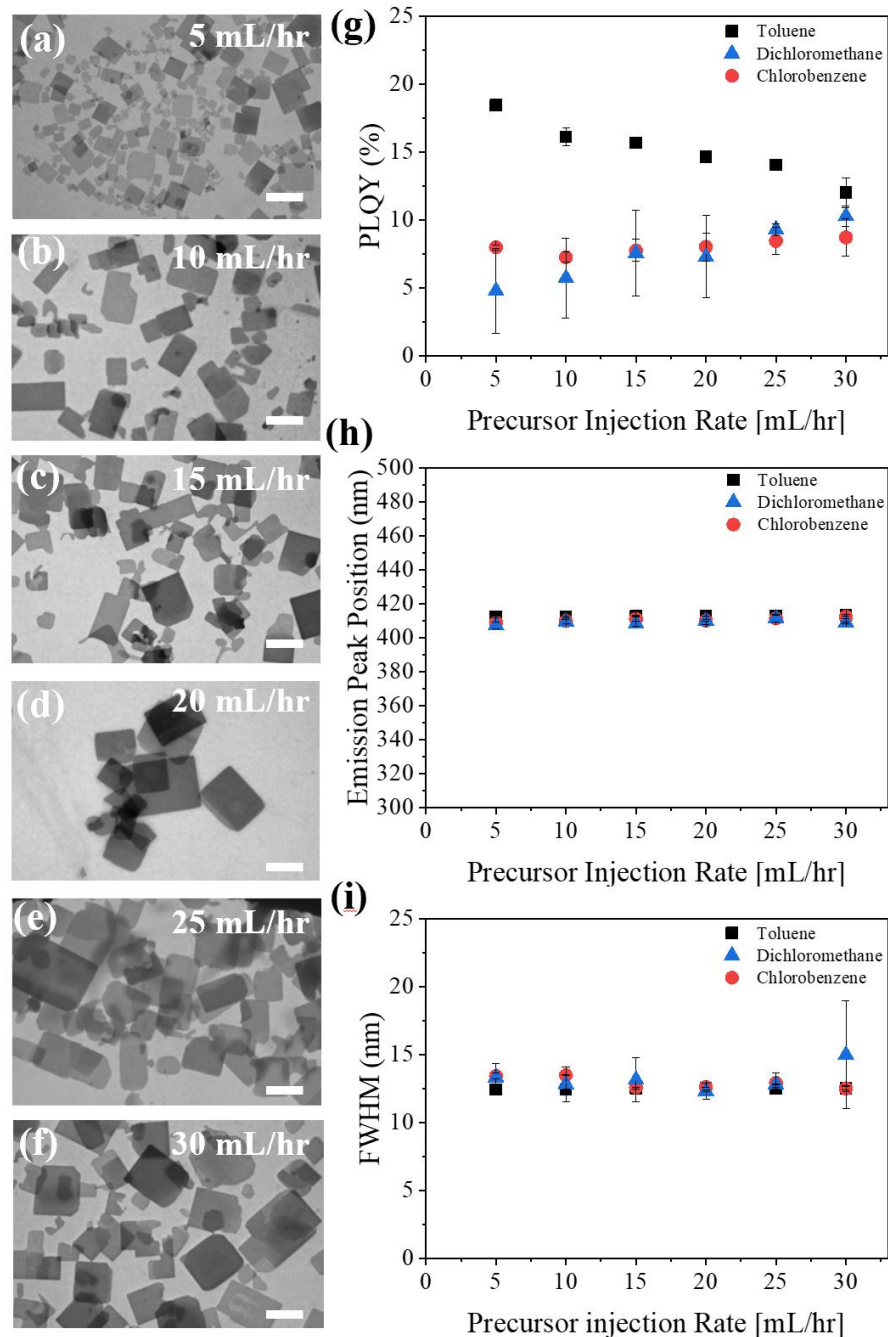


Figure 18 - (a-f) TEM images of $(\text{PEA})_2\text{PbBr}_4$ nanoplatelets (NPLs) synthesized in the flow reactor with a reactor tube length of 15 cm, a toluene injection rate (Q_{tol}) held constant at 1200 mL/hr, and $Q_{\text{precursor}}$ ranging from 5-30 mL/hr, that is, (a) 5 mL/hr, (b) 10 mL/hr, (c) 15 mL/hr, (d) 20 mL/hr, (e) 25 mL/hr, and (f) 30 mL/hr, respectively. All scale bars = 2 μm . Effects of antisolvent composition and $Q_{\text{precursor}}$ on (g) PLQY, (h) emission peak position, and (i) FWHM of emission of $(\text{PEA})_2\text{PbBr}_4$ NPLs.

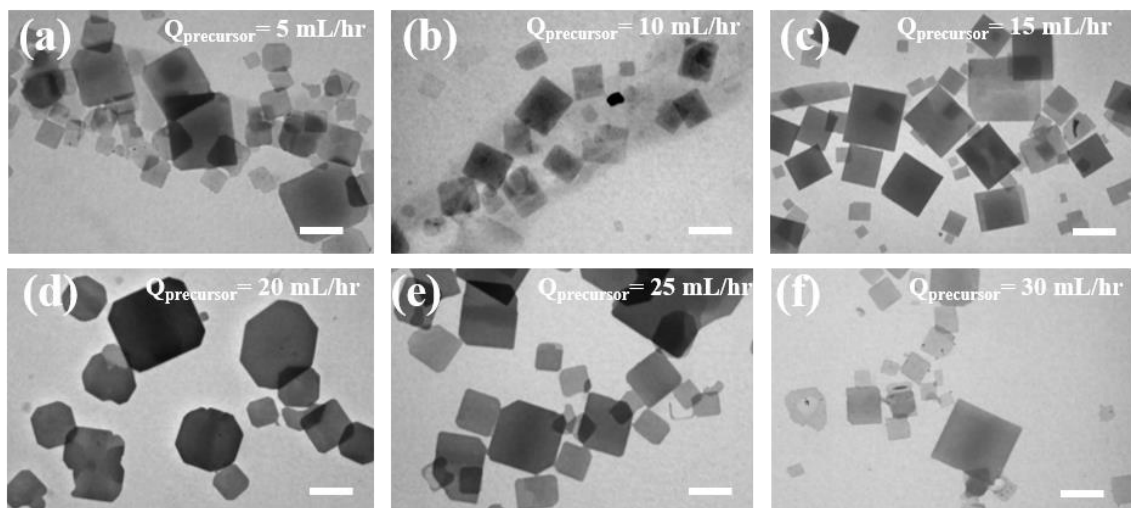


Figure 19 - TEM images of $(\text{PEA})_2\text{PbBr}_4$ NPLs produced in a 15cm reactor with chlorobenzene as the antisolvent at a constant flowrate of 1200 mL/hr and precursor injection rates ranging from 5-30 mL/hr, that is, (a) 5 mL/hr, (b) 10 mL/hr, (c) 15 mL/hr, (d) 20mL/hr, (e) 25 mL/hr, and (f) 30 mL/hr, respectively. All scale bars = 2 μm .

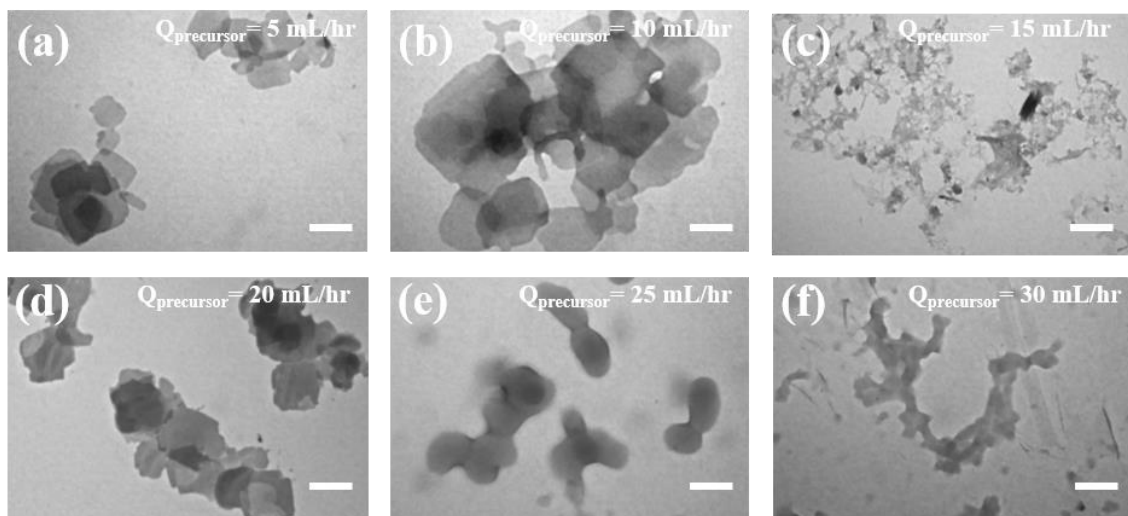


Figure 20 - TEM images of $(\text{PEA})_2\text{PbBr}_4$ NPLs made in a 15cm reactor with dichloromethane as the antisolvent at a constant flowrate of 1200 mL/hr and precursor injection rates ranging from 5-30 mL/hr, that is, (a) 5 mL/hr, (b) 10 mL/hr, (c) 15 mL/hr, (d) 20mL/hr, (e) 25 mL/hr, and (f) 30 mL/hr, respectively. All scale bars = 2 μm .

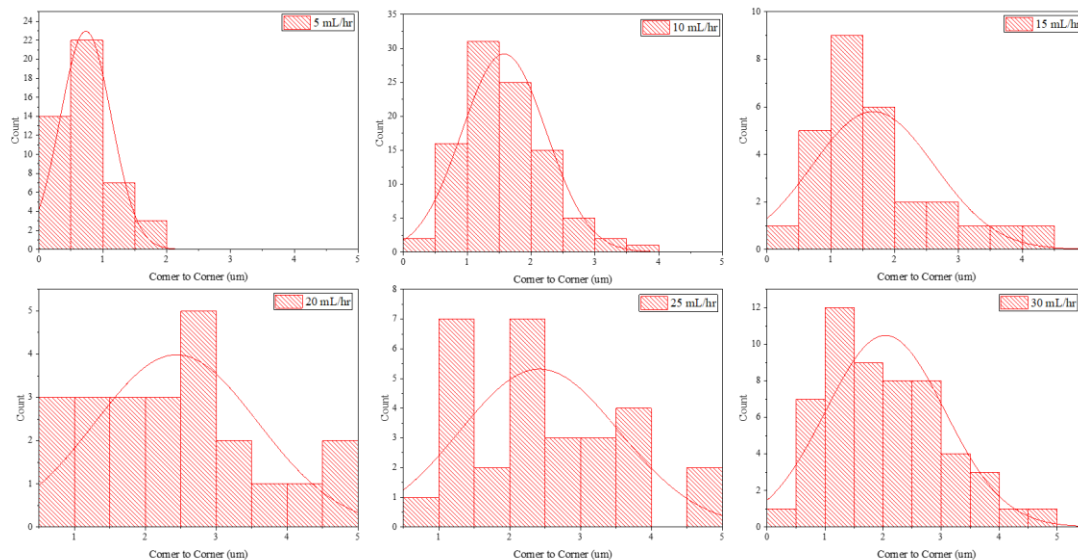


Figure 21 - Nanoplatelet size distribution of $(\text{PEA})_2\text{PbBr}_4$ NPLs made in 15cm reactor tube with $Q_{\text{toluene}}=1200$ mL/hr at various $Q_{\text{precursor}}$.

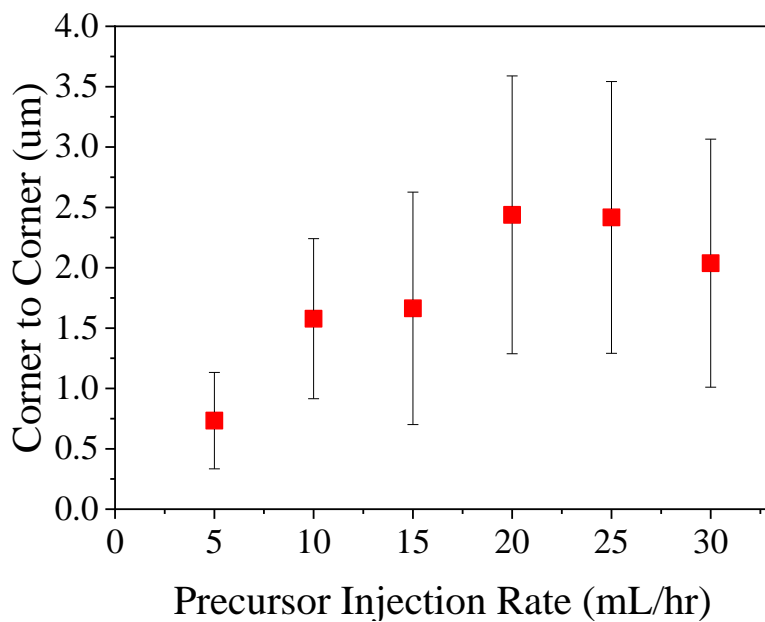


Figure 22 - Average corner to corner length and deviation of $(\text{PEA})_2\text{PbBr}_4$ NPLs made in 15cm reactor tube with $Q_{\text{toluene}}=1200$ mL/hr at various $Q_{\text{precursor}}$.

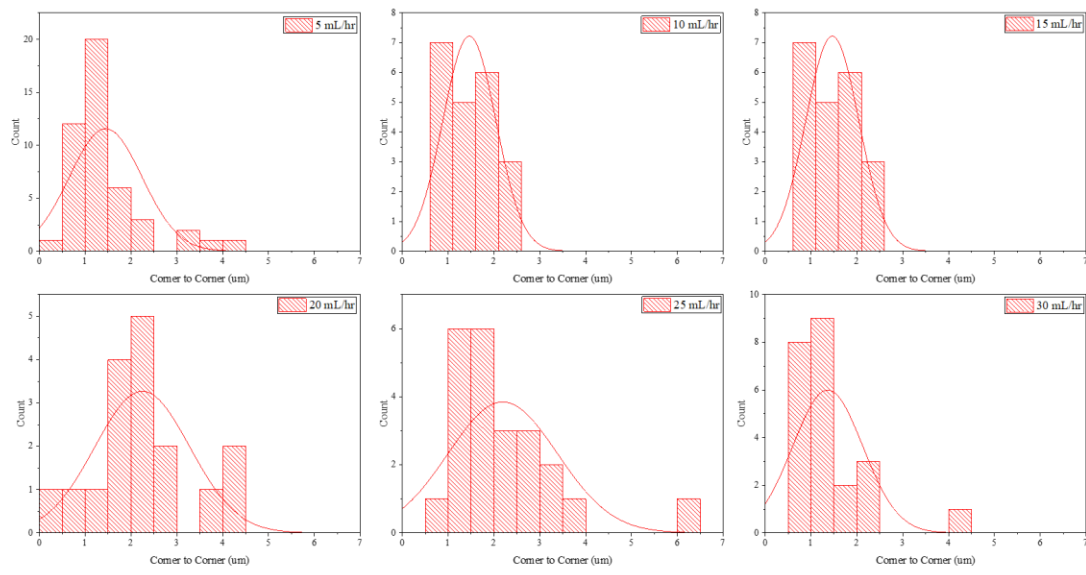


Figure 23 - Nanoplatelet size distribution of $(\text{PEA})_2\text{PbBr}_4$ NPLs made in 15cm reactor tube with $Q_{\text{chlorobenzene}}=1200 \text{ mL/hr}$ at various $Q_{\text{precursor}}$.

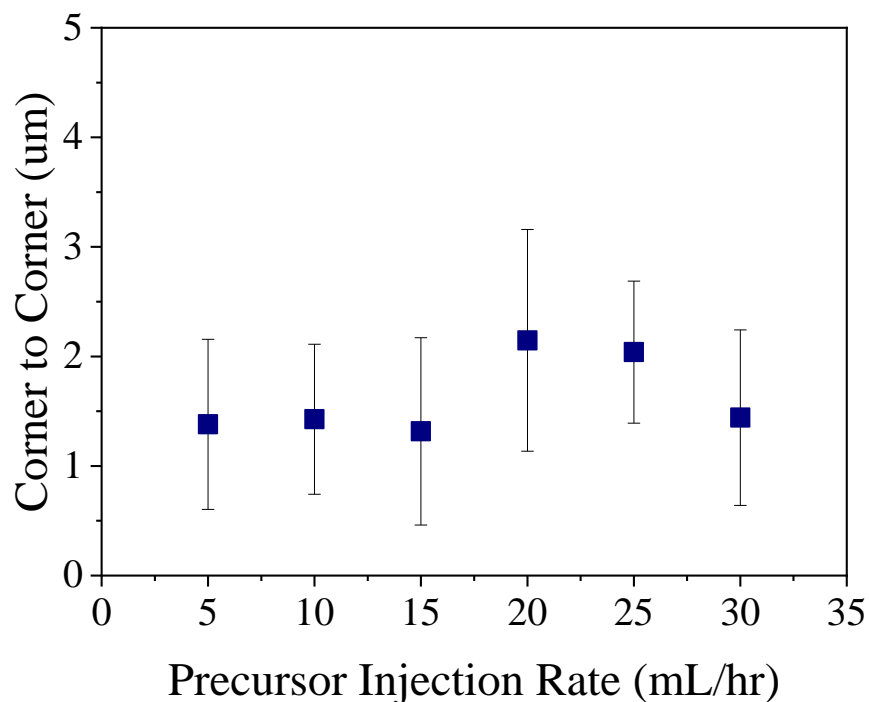


Figure 24 - Average corner to corner length and deviation of $(\text{PEA})_2\text{PbBr}_4$ NPLs made in 15cm reactor tube with $Q_{\text{chlorobenzene}}=1200$ mL/hr at various $Q_{\text{precursor}}$.

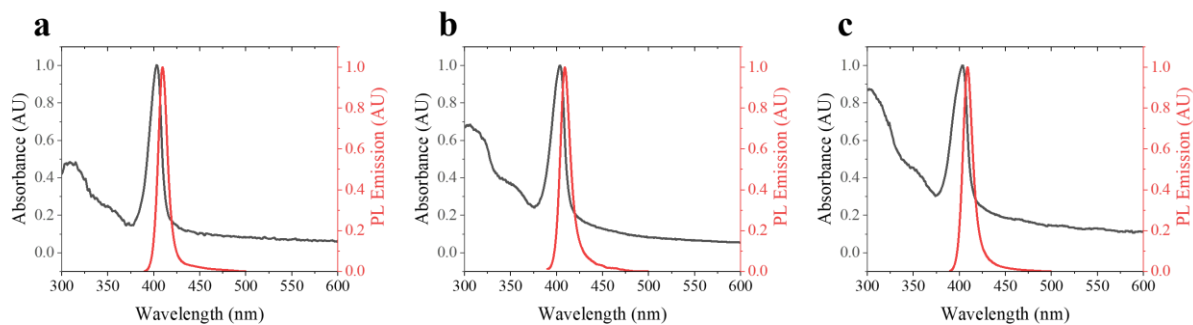


Figure 25 - UV-vis absorbance and PL emission of $(\text{PEA})_2\text{PbBr}_4$ NPLs produced in 15 cm reactor with 5 mL/hr precursor injection rate and 1200 mL/hr flow of (a) toluene, (b) chlorobenzene, and (c) dichloromethane antisolvent.

II. Influence of Reactor Tube Length

After toluene was determined to be the optimal antisolvent, it was used to investigate the effect of reactor tube length on the optical properties of (PEA)₂PbBr₄ NPLs. To this end, trials were run in the flow reactors with tube lengths of 15, 30 and 60 cm. For each tube length, Q_{tol} was fixed at 1200 mL/hr and $Q_{precursor}$ ranged from 5-30 mL/hr. Reactor tube length was found to have little effect on the morphology of the as-synthesized NPLs. Representative TEM images of NPLs synthesized with different reactor tube lengths but otherwise identical conditions ($Q_{tol}=1200$ mL/hr and $Q_{precursor}= 5$ mL/hr) are shown in **Figure 26a-c** (TEM images for $Q_{precursor}$ of 5-30 mL/hr for 15, 30, and 60 cm tube lengths are shown in **Figure 18a-f**, **Figure 27a-f**, and **Figure 28a-f**, respectively). The similarities of these TEM images signify that there is little effect from the reactor tube length. Reactor tube length was also found to exert a minimal effect on either FWHM or peak position (**Figure 26d-e**). We note that consistent FWHM and peak position were also observed in both the toluene and chlorobenzene antisolvent trials. As noted above, a unique property of n=1 RP perovskite is its restricted ability to form only one product with a single, sharp emission peak.¹⁹⁹ Shorter reactor tube lengths were generally observed to result in a higher average PLQY (with the exception of $Q_{precursor} = 30$ mL/hr, **Figure 26f**). Notably, this inconsistency occurred at the highest $Q_{precursor}$ level (30mL/hr) and resulted in the lowest PLQY for each sample (between 10 and 12%). Thus, the inconsistency may be attributed to degradation from the relatively high concentration of polar DMF. For the 15cm tube, a clear trend of increasing PLQY with decreasing $Q_{precursor}$ can be observed, which is consistent with previous study.²²⁹ This trend of increasing PLQY with decreasing $Q_{precursor}$ was less pronounced for samples made with longer reactor tubes (30 and 60 cm). We

hypothesize that this could be ascribed to longer tubes leading to an increase in residence time in the reactor tube. This increased residence time in turn could increase the interaction between DMF and the NPLs, thereby potentially degrading their structural integrity and decreasing PLQY. This residence time-induced degradation could obscure effects from increased $Q_{\text{precursor}}$, which are more obvious in the shorter tube lengths where residence time-induced degradation is not as prevalent. Further study, including modelling of the complex fluid dynamics, is needed to better understand this phenomenon.

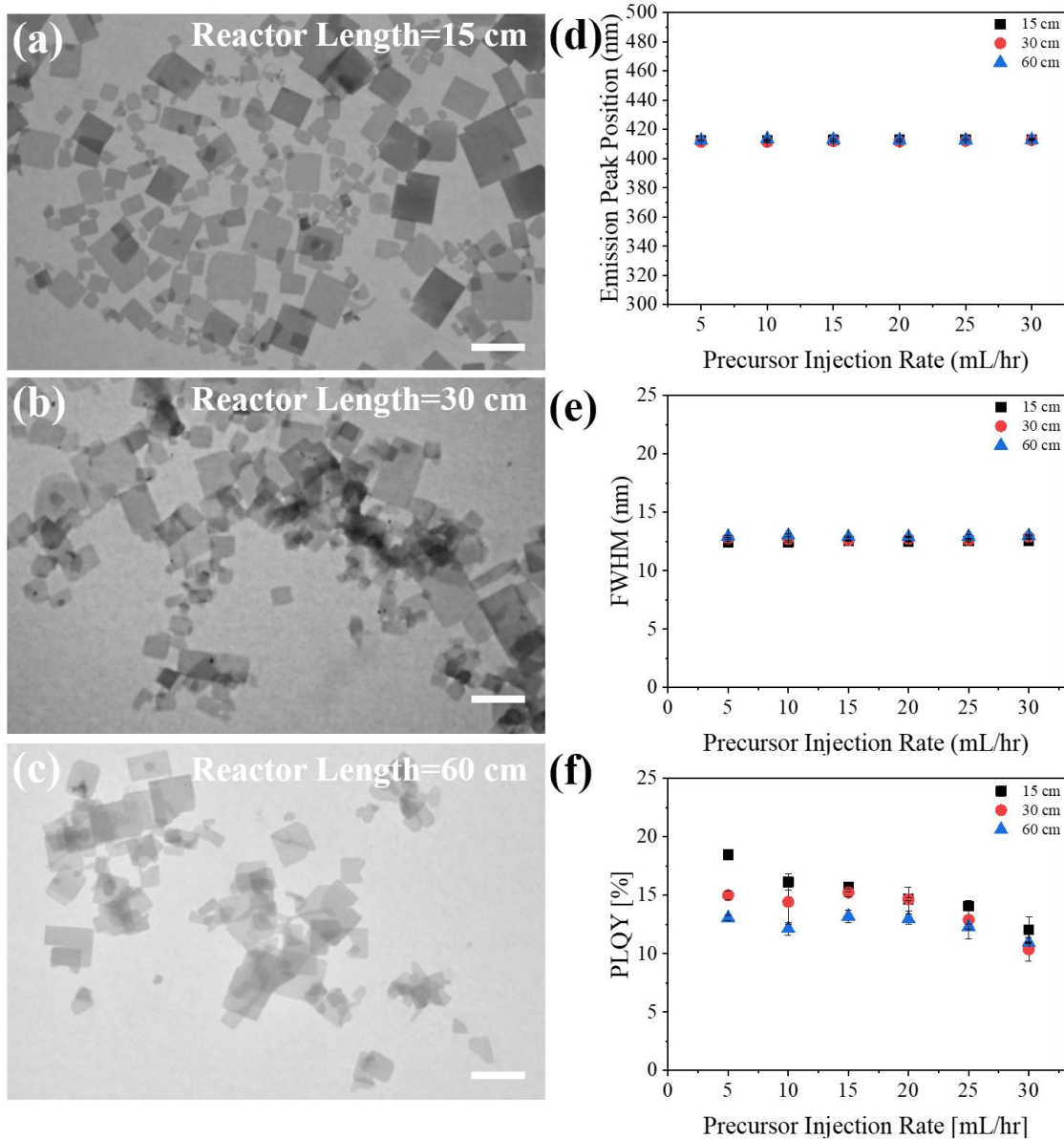


Figure 26 - TEM images of (PEA)₂PbBr₄ NPLs produced in the flow reactor with (a) 15 cm, (b) 30 cm, (c) 60 cm reactor tubes and 1200 mL/hr toluene and 5 mL/hr precursor solution injection rates. All scale bars = 2 μm. Effects of reactor tube length (from 15-60 cm) and precursor injection rates (from 5-30 mL/hr) on (d) emission peak position, (e) FWHM, (f) PLQY of (PEA)₂PbBr₄ NPLs.

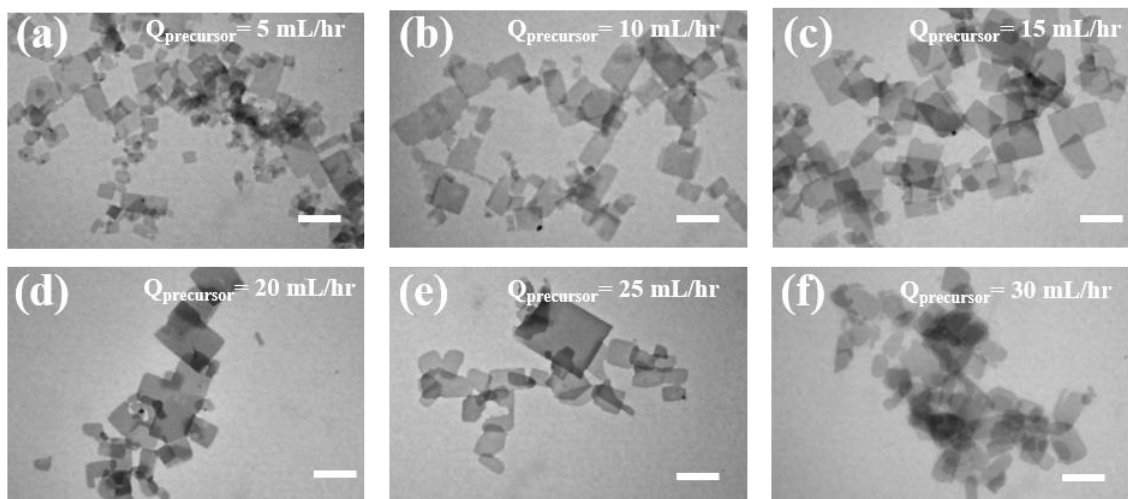


Figure 27 - TEM images of $(\text{PEA})_2\text{PbBr}_4$ NPLs produced in a 30cm reactor with toluene as the antisolvent at a constant flowrate of 1200 mL/hr and precursor injection rates ranging from 5-30 mL/hr, that is, (a) 5 mL/hr, (b) 10 mL/hr, (c) 15 mL/hr, (d) 20mL/hr, (e) 25 mL/hr, and (f) 30 mL/hr, respectively. All scale bars = 2 μm .

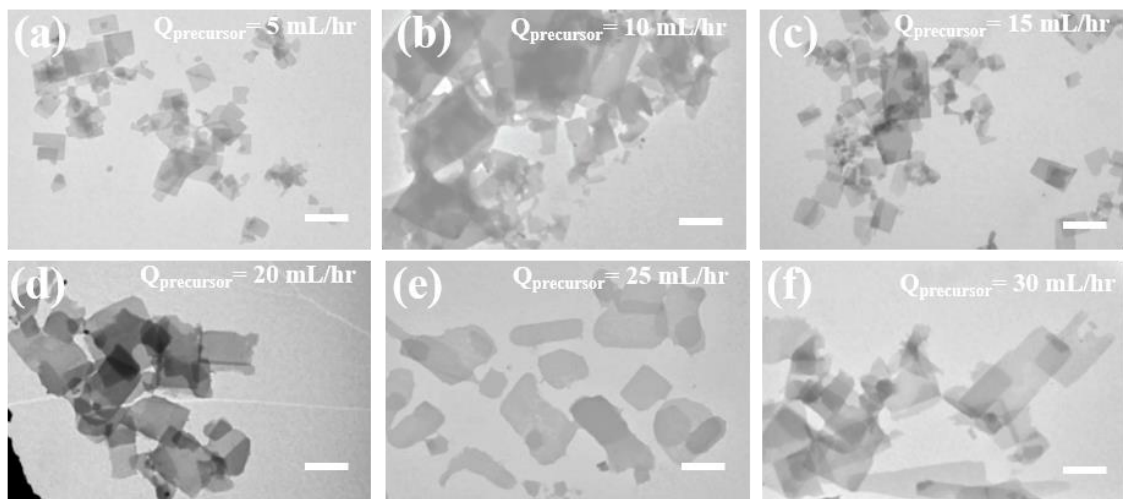


Figure 28 - TEM images of $(\text{PEA})_2\text{PbBr}_4$ NPLs produced in a 60cm reactor with toluene as the antisolvent at a constant flowrate of 1200 mL/hr and precursor injection rates ranging from 5-30 mL/hr, that is, (a) 5 mL/hr, (b) 10 mL/hr, (c) 15 mL/hr, (d) 20mL/hr, (e) 25 mL/hr, and (f) 30 mL/hr, respectively.

III. Examination of Precursor Solution Injection Rate

Throughout both the antisolvent composition and reactor tube length trials, the effect of precursor solution injection rate ($Q_{precursor}$) was also scrutinized. In both trials, Q_{anti} was kept constant at 1200 mL/hr and $Q_{precursor}$ ranged from 5-30 mL/hr. $Q_{precursor}$ was seen to impose a negligible impact on the peak position (**Figure 18h** and **Figure 26d**) of as prepared 2D perovskite NPLs (**Figure 18h** and **Figure 26d**). Additionally, the FWHM of all samples was found to be relatively unaffected by altering $Q_{precursor}$ (**Figure 18i** and **Figure 26e**). The minor fluctuations from the DCM trial can be attributed to the high polarity of the solvent, as discussed above. The relative stability of both emission wavelength and FWHM are in agreement with the fact that, based on the precursors in the solution, any emissive crystals formed would necessarily have to be monolayer $n=1$ NPLs. $Q_{precursor}$ was found to affect PLQY differently for each antisolvent. For DCM increasing $Q_{precursor}$ resulted in an increase of PLQY (from ~5% to ~10%), for chlorobenzene altering $Q_{precursor}$ had little impact on PLQY (stayed a relatively constant 8%), and for toluene decreasing $Q_{precursor}$ led to an increase in PLQY (from ~10% to ~20%) (**Figure 26d**). The trend of higher PLQY with increasing $Q_{precursor}$ for the more polar solvents (DCM and chlorobenzene) could be due to the relatively higher saturation concentrations of the perovskite precursor.²²⁶ Because these relatively polar solvents encourage solvation of the precursor, a greater concentration of precursor is needed to enable the growth of quality crystals. For the samples synthesized with toluene (lowest polarity among all antisolvents), the consistently higher PLQY from lower $Q_{precursor}$ is likely due to lower concentrations of DMF in the flow reactor. Because Q_{tol} is held constant, every increase of $Q_{precursor}$ results in a relatively higher concentration of DMF in the reactor and final product solution. Final

product solutions with relatively larger amounts of DMF impart a higher possibility of NPL degradation.²³⁰ This is in good agreement with previous study which have shown that increasing the amount of precursor solution in conventional LARP methods rapidly decreases the PLQY of the resultant nanocrystals.²²⁹ Additionally, lower $Q_{precursor}$ could result in better mixing of the precursor with antisolvent due to the relatively higher ratio of antisolvent to precursor. This higher ratio could increase the likelihood of complete crystallization.

IV. Scrutiny of Antisolvent Flowrate

After the optimal antisolvent composition, reactor tube length, and $Q_{precursor}$ were identified, the influence of Q_{anti} on $(PEA)_2PbBr_4$ NPLs was probed. For this trial, the previously optimized antisolvent composition (toluene), reactor tube length (15 cm), and $Q_{precursor}$ (5 mL/hr) were held constant while the toluene flowrate (Q_{tol}) was varied from 514-1200 mL/hr. Altering Q_{tol} was seen to have little impact on the morphology of the as-synthesized NPLs. The TEM images of NPLs produced from the various Q_{tol} (**Figure 29a-e**) display few differences, with the exception of the TEM image from the lowest Q_{tol} (514 mL/hr, **Figure 4e**) which resulted in irregular NPLs with some structural degradation. This could be attributed to the relatively higher ratio of DMF:antisolvent for the lower Q_{tol} trial, which could degrade the as-formed NPLs via the presence of high-concentration polar solvent (i.e., DMF). The particle size distribution and average corner to corner length and distribution of these NPLs are shown in **Figure 30** and **Figure 31**. **Figure 31** illustrates that NPLS made with the highest and lowest Q_{tol} resulted in NPLs with average sizes of with averages size of 2 ± 1 μm and 4.5 ± 3 μm , respectively. This trend of decreasing size and distribution with increasing Q_{tol} can be attributed to the enhanced mixing that occurs

at higher flowrates, which is consistent with previous studies.^{95, 231} Changing Q_{tol} imposed little effect on PLQY, and FWHM, or peak position of NPLs (**Figure 29f-h**). This can be ascribed to the fact that, though the flowrate of toluene was tuned over a wide range, the nature of the flow in the tube was unchanged. To confirm this, the Reynolds number (Re) corresponding to the flow for each trial was calculated using the following equation:

$$Re = \frac{\rho QD}{\mu A}$$

where ρ is the density of the fluid, μ is the dynamic viscosity of the fluid, A is the cross-sectional area of the tube, and D is the inner diameter of the PTFE tube. Generally, laminar flow is expected when $Re < 2000$ and turbulent flow is yielded at $Re > 2000$. The Re for all flowrates in this trial did not exceed 2000 (the highest Re was 393; see **Section 4.2** for more details; Error! Reference source not found.), suggesting that all experiments occurred in a laminar flow regime. This finding further enforces that, though the flowrates of each trial were different, nominal changes to their optical properties were observed because the nature of the flow was always laminar. In a similar study, altering Q_{anti} from 6-72 mL/hr was also found to affect little on the PL properties of flow reactor-synthesized MAPbBr₃ NCs.²²² The lack of impact was ascribed to the finding that changing Q_{anti} had a limited influence on the concentration field of the system, as determined by finite element analysis.

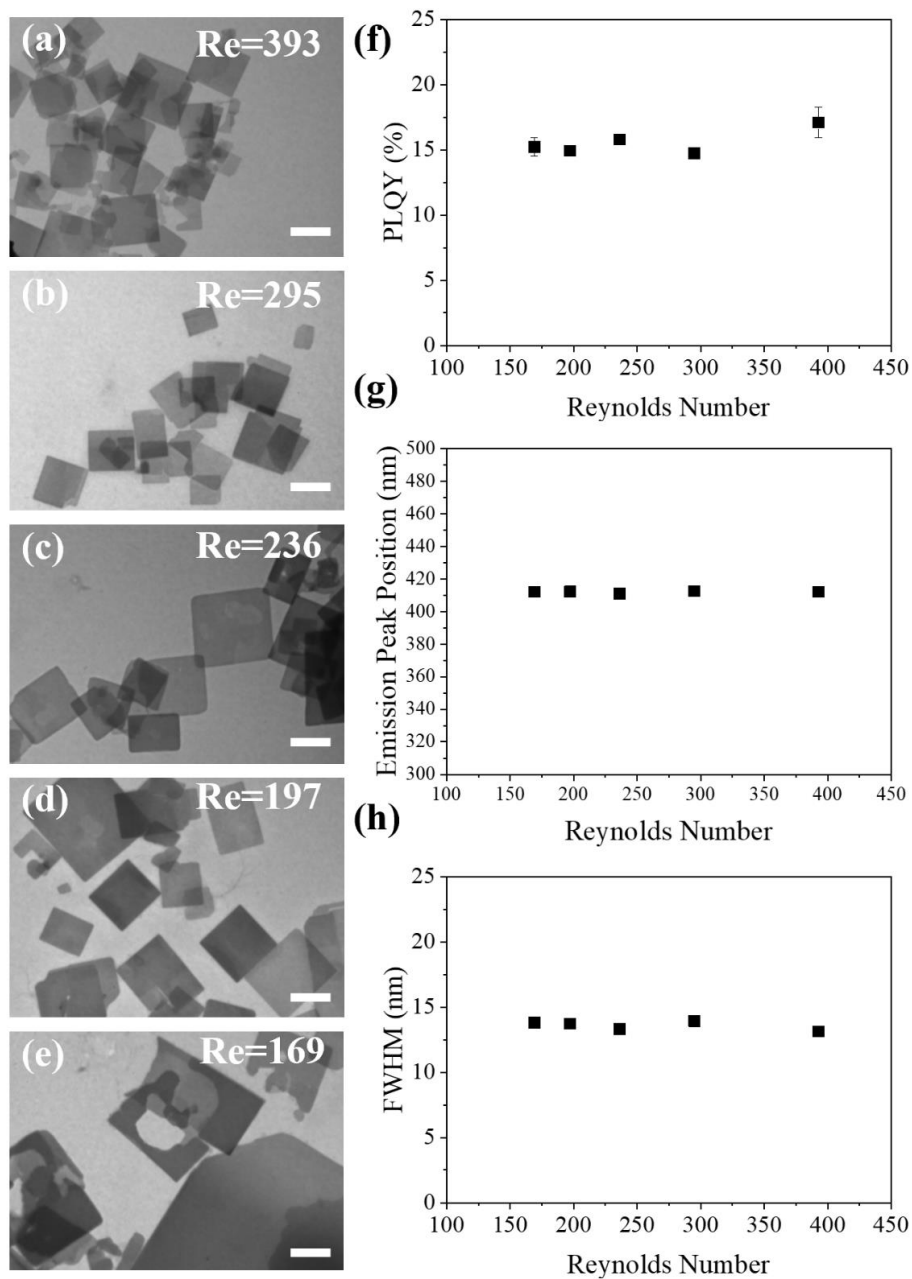


Figure 29 - (a-e) TEM images of (PEA)₂PbBr₄ NPLs synthesized in the flow reactor at varying toluene injection rates (from 514-1200 mL/hr) with a constant precursor injection rate of 5 mL/hr. All scale bars = 2 μm. The effect of Reynolds Number on (f) PLQY, (g) emission peak position, and (h) FWHM of (PEA)₂PbBr₄ NPLs.

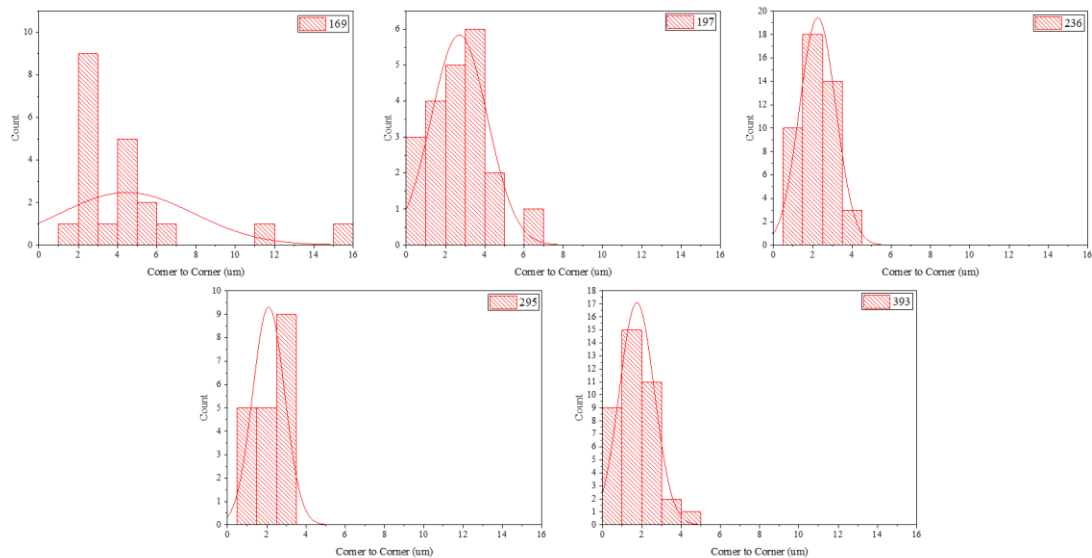


Figure 30 - Particle size distribution of $(\text{PEA})_2\text{PbBr}_4$ NPLs made in 15 cm reactor tubes with $Q_{\text{precursor}} = 5\text{ mL/hr}$ at varied toluene injection.

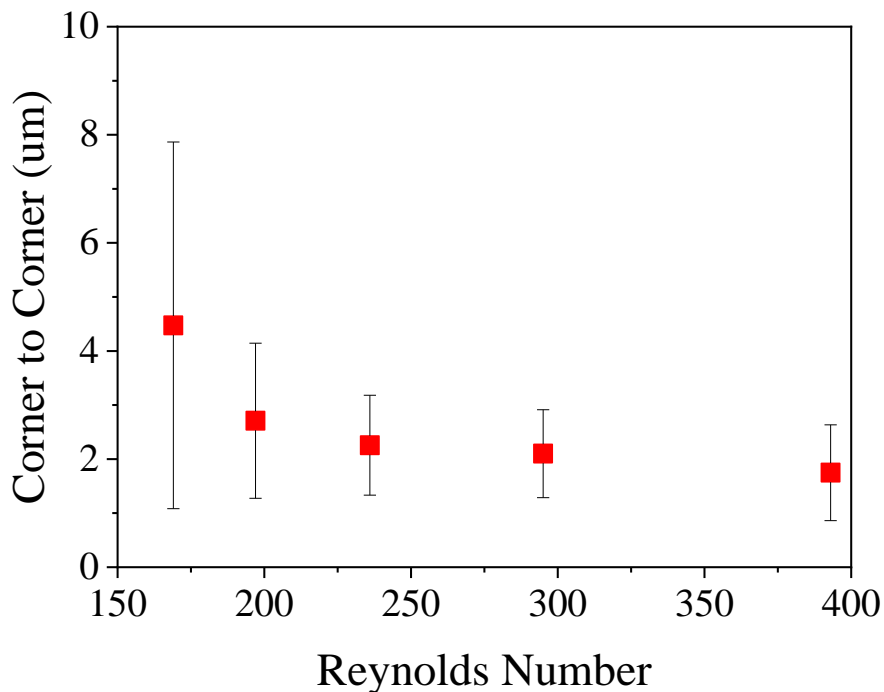


Figure 31 - Average corner to corner length and distribution of $(\text{PEA})_2\text{PbBr}_4$ NPLs made in 15 cm reactor tubes with $Q_{\text{precursor}} = 5\text{ mL/hr}$ at varied toluene injection.

It is notable that though many parameters were tuned throughout the trials, many of the optical properties of the $(\text{PEA})_2\text{PbBr}_4$ NPLs remained relatively constant. FWHM and peak position of the PL were unchanged by altering the antisolvent composition, reactor tube length, $Q_{\text{precursor}}$, or $Q_{\text{antisolvent}}$. As seen in **Figure 32** and **Figure 33**, neither changing the antisolvents nor reactor tube length resulted in meaningfully altered peak position or FWHM. These stable optical properties are also in good agreement with those observed for changing Q_{tot} , as shown in **Figure 29g-h**. The unchanged peak position and FWHM of emission are consistent with the fact that all $(\text{PEA})_2\text{PbBr}_4$ NPLs are monolayer thick. As the only available cation in the system is the monovalent bulky spacer PEA, any luminescent crystal formed is $n=1$ $(\text{PEA})_2\text{PbBr}_4$. In addition, because of the nature of this material, all produced NPLs experience identical quantum confinement, ensuring a stable and constant emission.¹⁹⁹

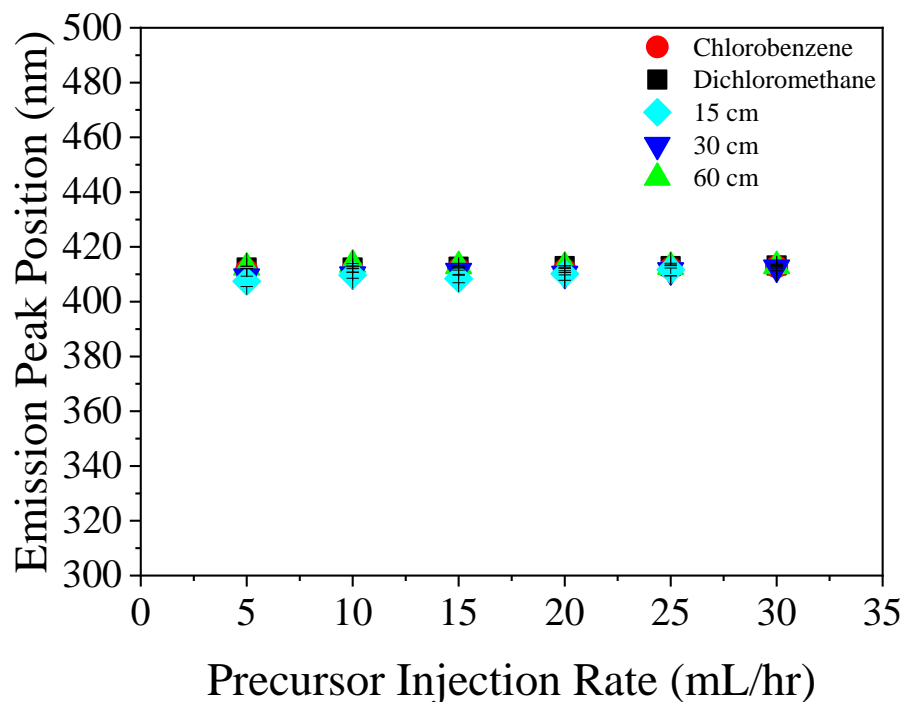


Figure 32 - Comparison of emission peak position of a variety of trials. Chlorobenzene and dichloromethane samples were created with Q_{anti} held constant at 1200 mL/hr and 15 cm reactor tube lengths. The variable tube length trials were conducted with toluene as the antisolvent and Q_{tol} was a constant 1200 mL/hr.

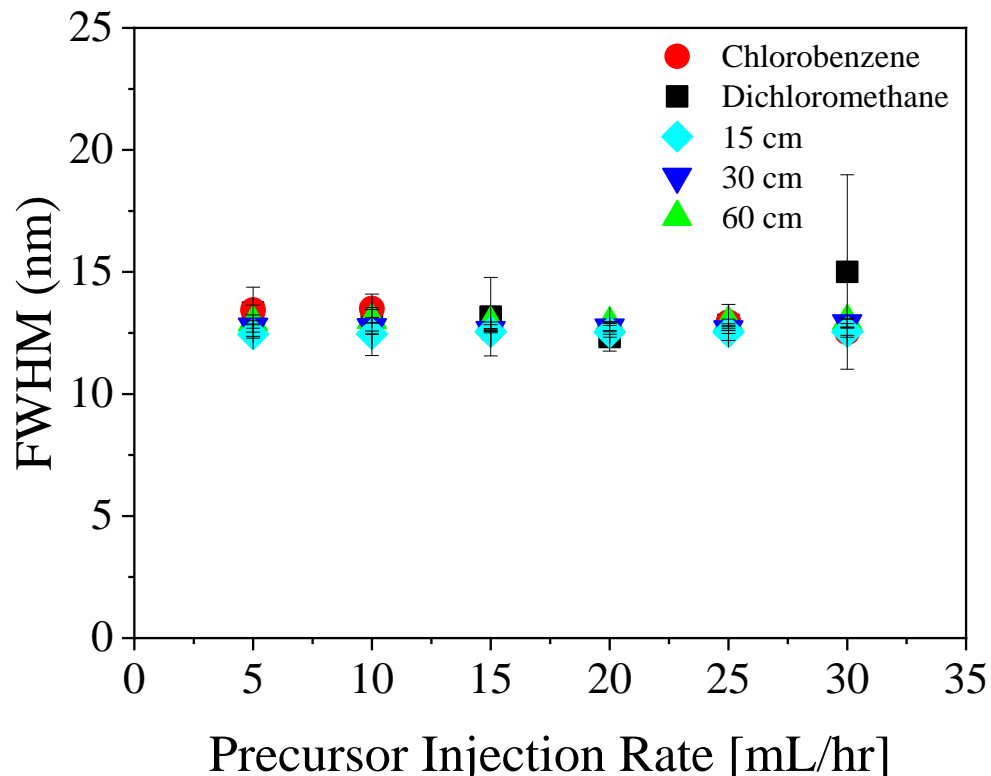


Figure 33 - Comparison of FWHM of emission of a variety of trials. Chlorobenzene and dichloromethane samples were created with Q_{anti} held constant at 1200 mL/hr and 15 cm reactor tube lengths. The variable tube length trials were conducted with toluene as the antisolvent and Q_{tol} was a constant 1200 mL/hr.

The optimized antisolvent, $Q_{precursor}$, reactor tube length, and Q_{tol} were then implemented to craft high-quality $(PEA)_2PbBr_4$ and $(PEA)_2PbI_4$ NPLs. **Figure 34a-d** compares TEM images of NPLs produced from the optimized flow reactor as well as synthesized via conventional LARP batch synthesis. NPLs made from either strategy possess characteristic platelet morphology, while the NPLs synthesized from conventional LARP batch synthesis have a smaller average dimension. This decreased average size is due likely to the limited growth of NPL nuclei caused by the enhanced mixing of precursor solution with antisolvent via vigorous stirring. Conversely, in the flow reactor, the laminar nature of the flow could

allow a prolonged growth time of nuclei as discussed above and yield NPLs with larger dimensions. **Figure 34e-f** present the UV-vis absorption and PL emission of flow-reactor-synthesized $(\text{PEA})_2\text{PbBr}_4$ and $(\text{PEA})_2\text{PbI}_4$ NPLs, respectively. The emission peaks of 410nm for $(\text{PEA})_2\text{PbBr}_4$ ²²³⁻²²⁴ and 520nm for $(\text{PEA})_2\text{PbI}_4$ ²¹³ are in good agreement with those reported for NPLs made via conventional LARP. The absorption peaks are similarly consistent with previous reported results. It is worth noting that the average absolute PLQYs (measured via an integrating sphere) of $(\text{PEA})_2\text{PbBr}_4$ (18.5%) and $(\text{PEA})_2\text{PbI}_4$ (1.5%) NPLs formed in the flow reactor at optimized conditions are comparable (or better) to those of $(\text{PEA})_2\text{PbBr}_4$ (with reported values ranging from 5-24.8%)²²³⁻²²⁴ and $(\text{PEA})_2\text{PbI}_4$ (~1%)²¹³ NPLs synthesized by LARP batch synthesis.¹⁹⁴ The average PLQY, FWHM, and emission peak position of $(\text{PEA})_2\text{PbI}_4$ NPLs created in an optimized flow reactor ($l = 15\text{cm}$, $Q_{\text{tot}} = 1200 \text{ mL/hr}$) with $Q_{\text{precursor}}$ ranging from 5-30 mL/hr are summarized in **Figure 35a-c**. Atomic force microscopy was performed to verify the monolayer nature of the $(\text{PEA})_2\text{PbBr}_4$ NPLs made with the optimized parameters (**Figure 36a**). The observed thickness of ~2nm (**Figure 36b**) is in good agreement with previous study that reported the monolayer thickness of $(\text{PEA})_2\text{PbBr}_4$ to be 1.75nm.²³²

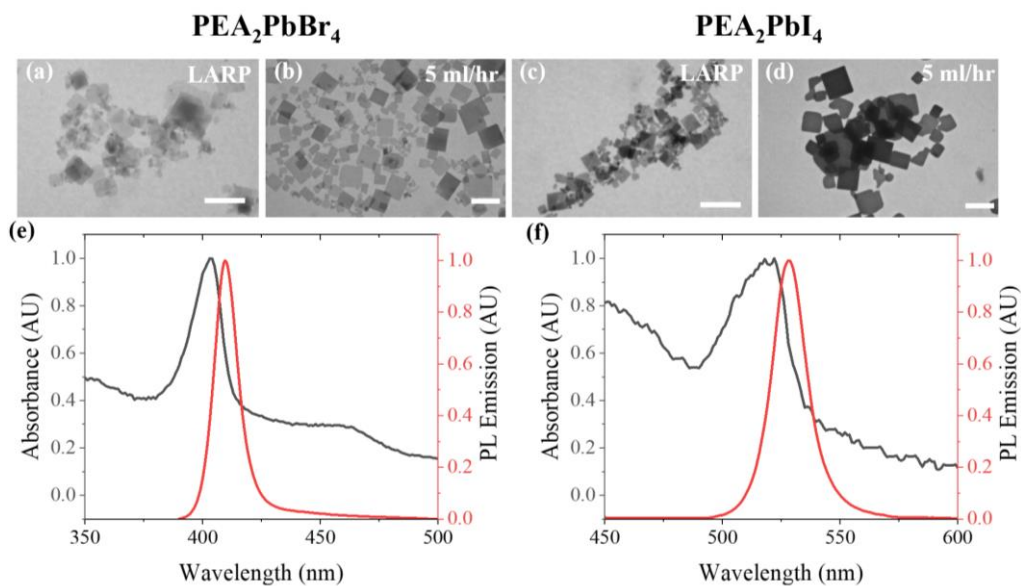


Figure 34 - TEM images of (a) and (c) LARP control and (b) and (d) flow reactor (1200 mL/hr toluene and 5 mL/hr precursor) $(\text{PEA})_2\text{PbBr}_4$ and $(\text{PEA})_2\text{PbI}_4$ NPLs, respectively. All scale bars = 2 μm . (e)-(f) UV-vis absorbance and PL of (e) $(\text{PEA})_2\text{PbBr}_4$ and (f) $(\text{PEA})_2\text{PbI}_4$ NPLs, respectively.

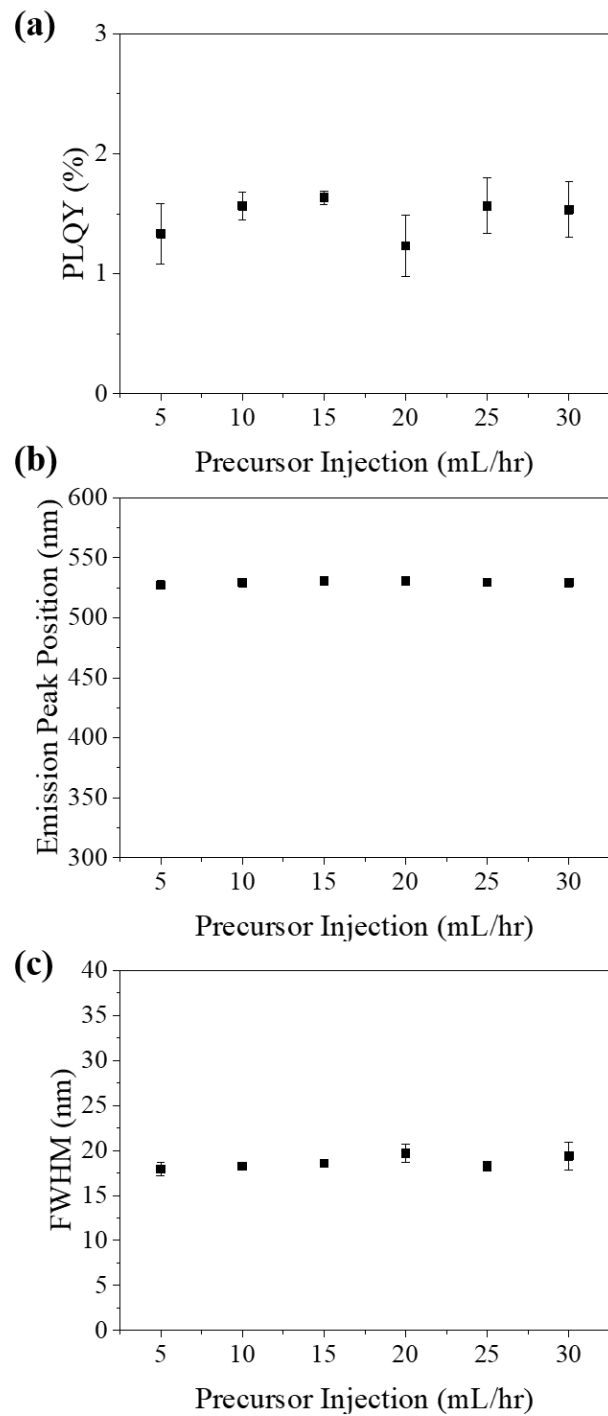


Figure 35 - (a) PLQY, (b) emission peak position, and (c) FWHM of $(\text{PEA})_2\text{PbI}_4$ NPLs produced in 15 cm reactor tube with a constant 1200 mL/hr toluene (antisolvent) flowrate and precursor solution flowrates ranging from 5-30 mL/hr (see x axis).

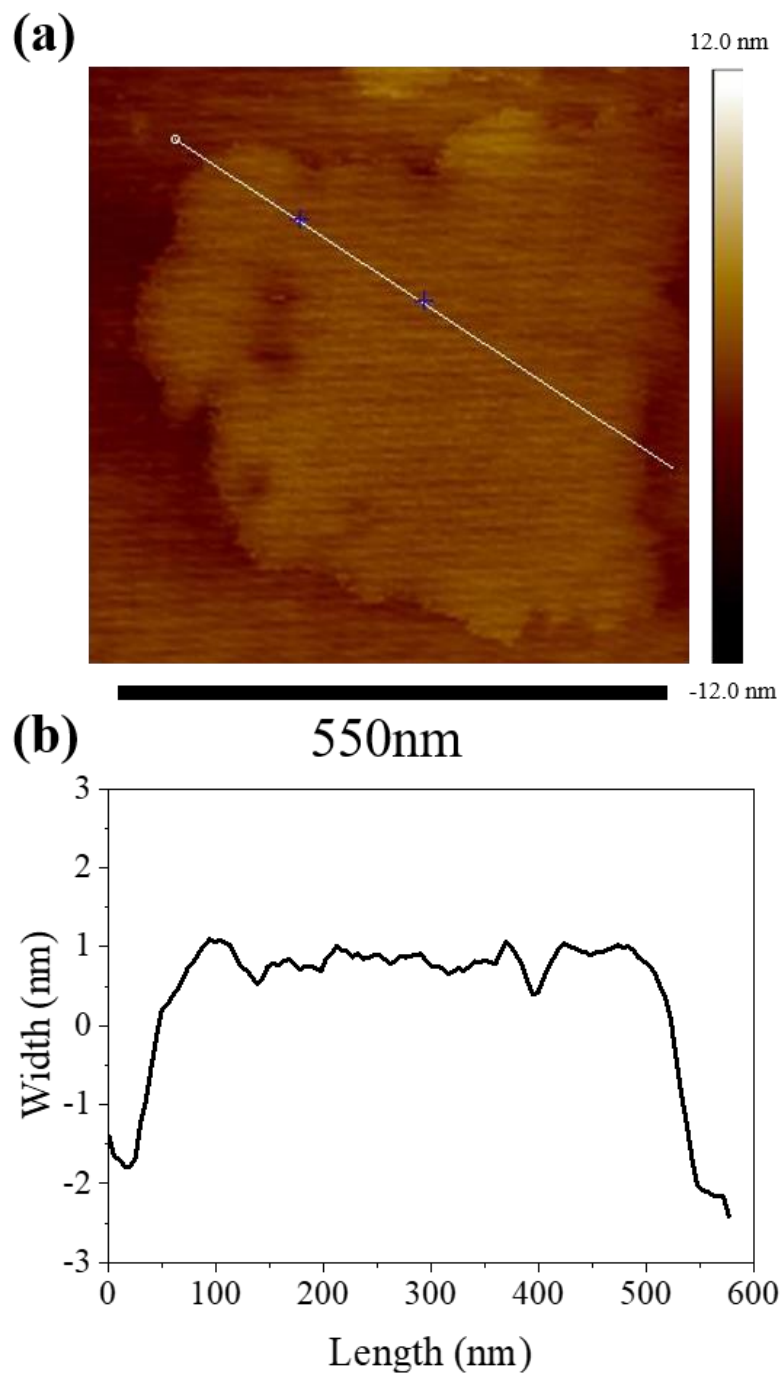


Figure 36 - (a) AFM image of $(\text{PEA})_2\text{PbBr}_4$ NPL made in a 15cm reactor tube at $Q_{\text{tol}}=1200$ mL/hr and $Q_{\text{precursor}}=5$ mL/hr. (b) Cross-sectional analysis of the line indicated in (a).

The effect of precursor solution concentration was then investigated. To accomplish this, the precursor solution concentration was doubled (from 0.02M PbBr₂ and 0.04M PEABr to 0.04M PbBr₂ and 0.08M PEABr in DMF), and the optimized flow parameters (toluene antisolvent, Q_{tol}=1200 mL/hr, Q_{precursor}=5 mL/hr, 15 cm reactor tube) were used. **Figure 37** shows TEM images of NPLs synthesized with concentrated precursor solutions at Q_{precursor} ranging from 5-30 mL/hr. No obvious trend can be seen in their morphology, with each Q_{precursor} resulting in NPLs with highly variable sizes. The PLQY of NPLs made from concentrated precursors was found to remain at a relatively constant value of ~9% regardless of precursor injection rate (**Figure 38a**). This value is significantly lower than that of the more dilute sample, which displayed a highest PLQY of ~18%. Interestingly, the lowest PLQY from the dilute samples (~11%) occurred at the highest Q_{precursor}. The relative similarity between the constant PLQY of the concentrated samples (~9%) and that highest Q_{precursor} of the dilute sample (~11%) could suggest that a critical ratio of precursor to antisolvent exists, beyond which PLQY will remain constant. At this critical ratio, there is potentially not sufficient toluene to spur crystallization of all perovskite precursors, leading to crystals with poor PL performance. Moreover, the emission peak position and FWHM were found to be relatively unaffected by changing the precursor concentration (**Figure 38b-c**). This is in good agreement with previous findings which have shown peak position and FWHM to be relatively stable throughout a variety of parameter tuning.

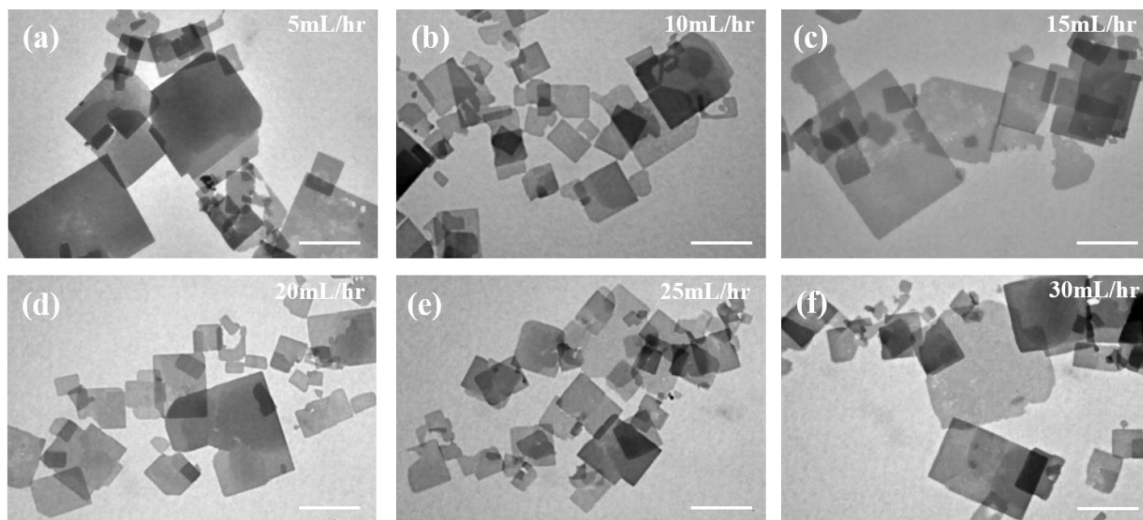


Figure 37 - TEM images of $(\text{PEA})_2\text{PbBr}_4$ NPLs produced with a precursor solution concentration of 0.04M PbBr_2 and 0.08M PEABr (double concentration in DMF) in a 15cm reactor with toluene as the antisolvent at a constant flowrate of 1200 mL/hr and precursor injection rates ranging from 5-30 mL/hr, that is, (a) 5 mL/hr, (b) 10 mL/hr, (c) 15 mL/hr, (d) 20mL/hr, (e) 25 mL/hr, and (f) 30 mL/hr, respectively. All scale bars = 2 μm .

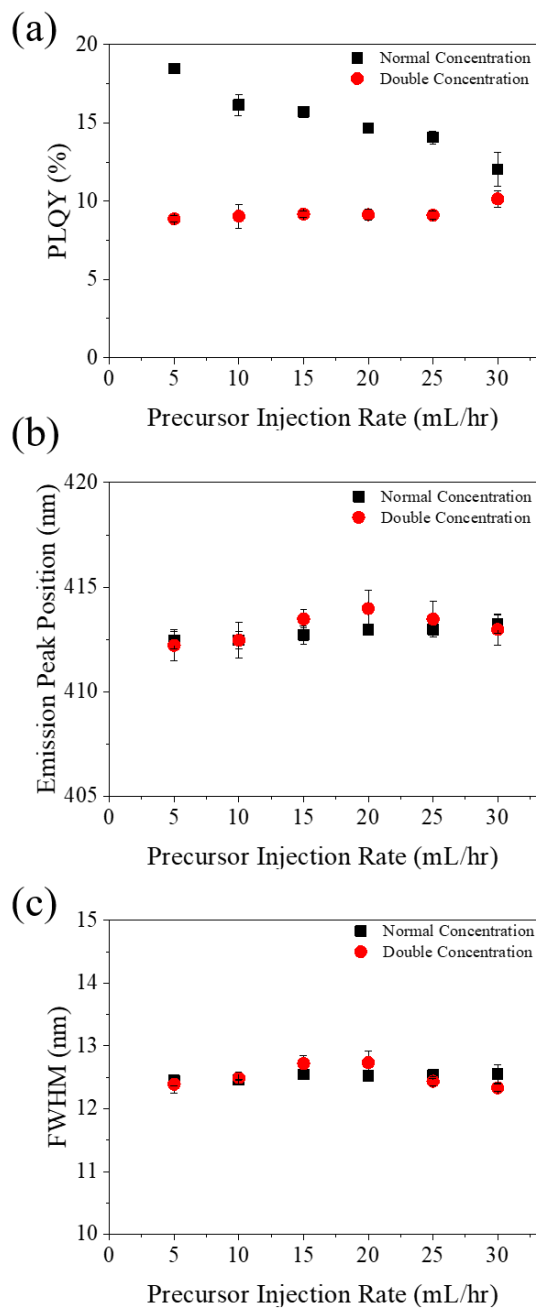


Figure 38- (a) PLQY, (b) emission peak position, and (c) FWHM of (PEA)₂PbI₄ NPLs produced with precursor solutions of 0.02M PbBr₂ and 0.04 PEABr (normal concentration in DMF) and 0.04M PbBr₂ and 0.08M PEABr (double concentration in DMF) in a 15 cm reactor tube with a constant 1200 mL/hr toluene (antisolvent) flowrate and precursor solution flowrates ranging from 5-30 mL/hr (see x axis).

Production rate (mass per time) is a key metric to evaluate the viability of any continuous production system. Determining the production rate of legacy batch synthesis strategies is difficult, because the time component is highly dependent on the rate at which batches are switched. As an estimate, we assumed that lab-scale batch synthesis of perovskite NPLs takes on average 60 s per batch, not including purification or cleaning of the reactors. Using this approximation, we estimated the production rate of batch synthesis to be 0.0185 g/hr (see **Equation 7** in **Section 4.2**). We then calculated the production rate of the flow reactor to be 0.1542 g/hr (**Equation 8** in **Section 4.2**). These calculations demonstrate well that our flow reactor enables a greater than eight times increase in the production rate of 2D RP perovskite NPLs. We also note that all samples yielded in the flow reactor were characterized without purification, which avoids the need for an additional and potentially costly step that could hinder commercial applications.

4.4 Conclusion

In summary, we demonstrated that a flow reactor is capable of continuously producing both $(\text{PEA})_2\text{PbBr}_4$ and $(\text{PEA})_2\text{PbI}_4$ NPLs with properties comparable to those of NPLs previously reported from batch synthesis. The selection of antisolvent (particularly its polarity) was witnessed to drastically affect the properties of the NPLs, with lower polarity solvents achieving better PLQY due to the absence of degradation of NPLs often caused by polar solvents. Furthermore, a moderate decrease in PLQY was observed as reactor tube length increased, which may be due to longer tubes resulting in a longer residence time that promotes interaction between DMF and the NPLs and thus the NPL degradation. In addition, altering the flowrate of antisolvent was not found to meaningfully affect any of the tested optical properties (e.g., PLQY, FWHM, peak position), which can

be attributed to the laminar flow characteristic at all injection rates. Antisolvent flowrate was, however, found to affect NPL morphology, with higher flowrates resulting in smaller and more monodisperse NPLs. A trend of higher PLQY with lower flowrates of precursor solution was noted for the toluene samples and was attributed to a relatively lower concentration of DMF in the final product solution, leading to less degradation of as-formed NPLs. Nearly all samples displayed a constant emission peak position and FWHM, correlating well with the nature of the highly quantum-confined 2D RP perovskite structure. Our systematic study displayed that 2D RP perovskite NPLs with competitive PL properties (i.e., PLQY, FWHM, and emission peak position) can be produced at rates eight times greater than that of traditional batch synthesis. This scaling-up represents a viable and crucial step towards far-reaching commercial applications of 2D RP perovskite NPLs. Insights gleaned from this investigation can be exercised to scale up production of other perovskite materials, including Dion–Jacobson perovskites and RP perovskites where $n > 1$.

CHAPTER 5. ENHANCING THE STABILITY OF RUDDLESDEN-POPPE PEROVSKITE VIA ENGINEERING ALKYLAMMONIUM CATION

Biesold, G. M., Bonadio, A., & Lin, Z. (in preparation)

5.1 Introduction

Metal halide perovskites, an emerging class of semiconducting materials with outstanding optoelectronic properties, have the general chemical formula ABX_3 . A^+ (commonly methylammonium ($CH_3NH_3^+$) (MA^+), formamidinium ($CH(NH_2)_2^+$) (FA^+), or Cs^+) and B^{2+} (commonly Pb^{2+} or Sn^{2+}) are cations of different sizes and X^- are halide anions (Cl^- , Br^- , I^-) that coordinate with the B^{2+} ions. The coordination of the X^- and B^{2+} ions result in corner sharing BX_6 octahedrons that constitute a three-dimensional (3D) framework. The A-site cations occupy the cavity within the framework. Metal halide perovskites have a relatively soft ionic lattice and a dynamically disordered crystal structure which results in tunable charge-carrier recombination rates and other nonclassical semiconductor characteristics.²³³⁻²³⁶ Metal halide perovskites have been extensively studied for solar energy conversion over the past decade due to their intriguing optoelectronic properties, including near-perfect crystalline structures,²³⁷ tunable direct band gaps,²³⁸ large absorption coefficient ($1.5 \times 10^4 \text{ cm}^{-1}$ at 550 nm),²³⁹ high ambipolar mobility ($\sim 20 \text{ cm}^2 \text{ V}^{-1} \text{ s}^{-1}$),²⁴⁰ long carrier diffusion lengths (100~1000 nm; $\sim 175 \mu\text{m}$ in $MAPbI_3$ single crystals) ($L_{\text{eff}, e} / L_{\text{eff}, h} < 1$),⁶ small exciton binding energy ($\sim 30 \text{ meV}$),²⁴¹ high defect tolerance,²⁴² solution processability, and low processing cost.²⁴³ Notably, the certified power conversion efficiency (PCE) of single-junction perovskite solar cells has rapidly increased from 3.8% in 2009 to 25.2% in 2019.²⁴⁴

To date, a wide range of perovskite nanostructures have been achieved, including quantum dots (QDs), nanoplatelets (NPLs), nanosheets (NSs) and nanowires (NWs).^{113, 194, 245-246} Similar to conventional semiconducting NCs, the composition, size, and structural engineering of metal halide PNCs can be realized via either *in-situ* synthesis or post-synthesis methods.²⁴⁷⁻²⁴⁸ Specific bulky organic cations (aliphatic or aromatic alkylammonium) can be inserted into 3D perovskite framework and function as spacers that isolate single (or multiple) inorganic perovskite layers.²⁴⁹ These resulting low-dimensional perovskites (Ruddlesden-Popper phase) possess relaxed limits of cation dimensions, expanded compositional diversity, and high environmental stability.^{195, 249-250} Numerous desirable properties (e.g. large exciton binding energy) can be achieved by tuning the composition and chain length of the bulky organic cations and by changing the number of layers of 2D perovskite.²⁵⁰ Perhaps most notably, Ruddlesden-Popper phase perovskite has been shown to possess enhanced environmental stability (compared to their 3D counterpart) from their ionically-attached hydrophobic alkylammonium cations^{206, 208}. Most often, the bulky alkylammonium cations consist most of fully saturated carbon chains, but functionalizing these cations by capitalizing on unsaturated outermost bonds represents an exciting new direction for enhancing the stability and functionality of Ruddlesden-Popper phase perovskites.

Unsaturated outer bonds have been used to functionalize conventional 3D ABX_3 perovskite. Recently, crosslinked methylammonium lead bromide ($MAPbBr_3$) PNCs were crafted through a modified ligand-assisted reprecipitation method using the trifunctional 4-vinyl-benzyl-dimethyloctadecylammonium chloride (V-18) as the polymerizable ligand.¹¹⁸ In V-18, the center of the ligand (an ammonium group with two methyl groups) was

found to induce sufficient ionic interactions with PNCs to anchor the ligands onto the NC surfaces, and the styryl groups and long alkyl side chain were found to facilitate radical polymerization and high colloidal stability, respectively.¹¹⁸ When synthesized in the presence of other inorganic ligands V-18-capped MAPbBr₃ NCs exhibited monodisperse morphology, excellent PLQY, high film conductivity, and optical homogeneity due to enhanced surface passivation. Further study demonstrated that the as-prepared MAPbBr₃ NCs could be thermally polymerized, or copolymerized with styrene and methyl methacrylate to obtain homogeneous MAPbBr₃ PNC/polymer nanocomposites that could be applied in LEDs with excellent performance.¹¹⁸ This *in-situ* method has been further extended to include other commercially available monomers, such as methyl methacrylate²⁵¹, lauryl methacrylate²⁵² and styrene²⁵³. *In-situ* synthesis of PNCs (e.g. CsPbBr₃ NCs) has also been conducted in pure monomer solutions. After formation of the NCs, the surface capped monomers can be polymerized via thermal polymerization or UV light-induced photopolymerization, both of which provide enhanced protection of the PNCs.²⁵¹ The resulting nanocomposites have been found to be highly soluble in organic solvents, which enables solution-processability and the ability to be used as a luminescent ink to create optoelectronic devices with high luminous efficiency and excellent color-rendering index.²⁵¹

Click chemistry is one of the most universal methods of easily modifying many organic molecules²⁵⁴. Click reactions are notable in that they are highly efficient, simple to execute, proceed rapidly, and result in no side products. Thiol-ene reactions, in particular, are an intriguing class of click chemistry that will be used for cation engineering. Thiol-ene reactions are photoinitiated processes which can be activated at specific times and

locations on the target molecules.²⁵⁵⁻²⁵⁶ Thiol-ene reactions occur via a free-radical chain mechanism. First, free radicals are generated via either heat or light (in this study the photo initiator 2,2,-dimethoxy-2-phenylacetophenone (DMPA) was used), and then they form thiyl radical species. The thiyl radical then propagates with available C=C (“ene”) functional groups via anti-Markovnikov addition, forming a carbon centered radical. A final chain transfer step removes a hydrogen radical, ensuring the strong covalent bonding. A graphic of typical thiol-ene mechanisms can be seen in **Figure 39** below.

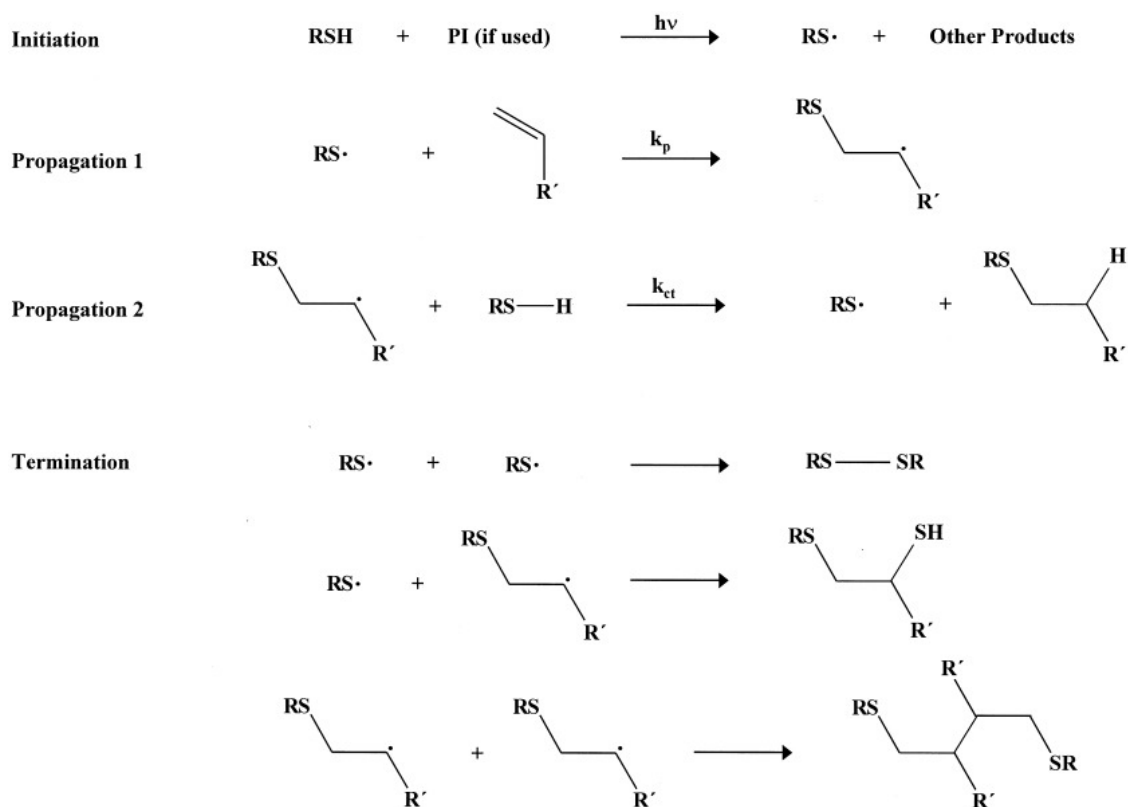


Figure 39 – General photoinitiated thiol-ene reaction mechanisms²⁵⁵

This study aims to combine the functionality of polymerizable ligands with the versatility of thiol-ene chemistry to engineer novel alkylammonium cations to enhance the stability of Ruddlesden-Popper perovskites. In the first thrust, organic shells will be

synthesized *in-situ* around Ruddlesden-Popper perovskites by crosslinking unsaturated butene ammonium bromide cations with disulfide molecules via a UV light induced thiol-ene reaction. After analysis, it was determined that the UV light necessary for driving this reaction also result in severe degradation of the perovskite itself. As such, a new *ex-situ* cation engineering method was developed, where thiol-ene chemistry was used to craft superhydrophobic perfluorinated cations. Cations were made with 8, 6, and 1 perfluorinated carbons, and these cations were then used to synthesize perfluorinated perovskite nanoplatelets. The stability and optical properties of these perfluorinated nanoplatelets were then systematically examined as a function of increasing degree of fluorination. Results suggest that increasing number of fluorinated carbons increases both the luminescence and water stability of NPLs.

5.2 Experimental Details

5.2.1 Materials

All materials were used as received. Toluene (ACS, VWR), anhydrous dimethylformamide (DMF, Millipore), lead bromide (99.99%, TCI), hydrobromic acid (48 wt%, Alfa Aesar), diethyl ether (ACS, Millipore Sigma), ethanol (200 proof, Koptec), methylamine (40 wt.% in water, BeanTown Chemical), 1-butylamine (99%, Thermo Scientific), 3-buten-1-amine (97%, Thermo Scientific Chemicals), 1-octylamine (99%, Alfa Aesar), 4-vinylbenzylamine (stabilized with MEHQ 92%, TCI), 1,6-hexanedithiol (97%, Thermo Scientific), 3,3,4,4,5,5,6,6,7,7,8,8,9,9,10,10,10-heptafluoro-1-decanethiol (>96%, Sigma-Aldrich), 3,3,4,4,5,5,6,6,7,7,8,8,8-tridecafluoro-1-octanethiol (97%, Sigma-Aldrich), 2,2,2-trifluoroethanethiol (95%, Sigma-Aldrich)

5.2.2 Methods

Synthesis of Alkylammonium Cations

The alkylammonium cations (methylammonium bromide (MABr), butylammonium bromide (BABr), butene-ammonium bromide (BeABr), octylammonium bromide (OABr), and vinylbenzyl ammonium bromide (VBABr) were synthesized in an acid-base method similar to that previously-reported.¹⁹⁴ In short, excess halide acids (HBr) were dropped into an ethanol/alkylamine mixture at 0 C. The solution was then stirred at room temperature for two hours. After two hours, the solution was dried via rotary evaporation until all liquid was removed. The mixture was then washed with diethyl ether three times, recrystallized with ethanol, and dried in a vacuum oven before use.

Synthesis of Colloidal Nanoplatelets

All perovskite nanoplatelets were synthesized using a modified ligand-assisted reprecipitation (LARP) technique. Perovskite precursors were added to anhydrous dimethylformamide in proper stoichiometric proportions. The proportions are (in terms of (LX:BX₂:AX) 2:1:0 and 2:2:1 for L₂PbX₄ (n=1) and L₄Pb₂X₇ (n=2), respectively. The precursor solution was then dropped into vigorously stirring toluene to allow for crystallization. Immediately, the solution changed color, indicating the formation of perovskite nanoplatelets.

In-Situ Thiol-Ene Crosslinking of Perovskite NPLs

In-situ crosslinking was conducted using a thiol-ene reaction in a manner similar to that previously reported.²⁵⁷ Specifically, DMPA and an excess amount of dithiol-containing

molecules (either dithiopropane or hexanedithiol) were added to toluene solutions of NPLs (made in the manner described above) with terminal alkene groups. The system was then purged via bubbling N₂ gas for at least 1 hour. After purging, the mixture was stirred under 365nm UV irradiation for the desired amount of time. Products were then separated via centrifugation.

Ex-Situ Thiol-ene Synthesis of Perfluorinated Alkene Cations

All three perfluorinated alkylammonium cations (perfluoro ethane ammonium bromide (PFEABr), perfluoro octane ammonium bromide (PFOABr), and perfluoro decane ammonium bromide (PFDABr)) were synthesized in an identical manner. BeABr (synthesized as described above), perfluoro alkane thiol (perfluorodecanethiol, perfluorooctanethiol, perfluoroethanethiol), and DMPA were first added to DMF. The solution was then degassed by bubbling for at least one hour. After purging, the solution was stirred under 365nm UV irradiation overnight to ensure full conversion. The products were isolated by rotary evaporation and washed with diethyl ether twice. The final products were then dried overnight in a vacuum oven. The dried cations were then used to synthesize NPLs in LARP method described above.

Characterization Techniques

The composition of the alkylammonium cations was verified with proton nuclear magnetic resonance spectroscopy (NMR) on a Varian Mercury 400 MHz. Organic synthesis was further verified by Fourier Transform Infrared Spectroscopy (FT-IR) on a Nicolet 6700 FT-IR spectrometer. Organic molecule composition was also confirmed with Raman Spectroscopy on a Renishaw inVia Raman Spectrometer. The photoluminescence (PL)

spectra of each 2D RP perovskite NPL was obtained by a PerkinElmer LS 55 fluorescence spectrometer with a 365nm excitation light. The absolute photoluminescence quantum yield (PLQY) was measured with a Hamamatsu Quantaurus QY Plus with an excitation wavelength of 365 nm. The absorbance of the NPLs was examined by 800-300 nm with a Shimadzu UV-2600. The morphologies of the NPLs were investigated with a JEOL CX-II transmission electron microscope (TEM) operated at 100 keV.

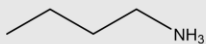
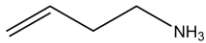
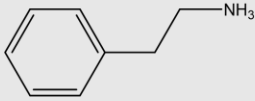
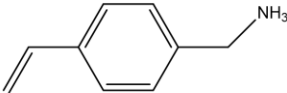
5.3 Results and Discussion

The first step in enhancing the stability of Ruddlesden-Popper perovskite via engineering alkylammonium cations was to determine the effects of different alkylammonium cations on the optical properties of resultant perovskite NPLs. Changing the structure of alkylammonium cations has already been shown to alter the emission and absorption peaks of otherwise identical NPLs²⁵⁸⁻²⁵⁹. The alkylammonium cation-dependent PL and absorption peaks have been attributed to many things, including (1) the differing dielectric constant of unique cations, (2) the angle between the cations and the perovskite surface (which induces distortions to the crystal lattice), and (3) the strength of the van der Waals interactions between adjacent cations.²⁵⁹ Four different alkylammonium cations were synthesized (as described in **Section 5.2**) and used to craft perovskite NPLs. Phenylethylammonium bromide (PEABr), butylammonium bromide (BABr), butene ammonium bromide (BeABr), and 4-vinylbenzylammonium bromide (VBABr) were chosen as the cations because of the similarity of their structures. BABr and BeABr are identical except for their outmost carbon to carbon bond. Similarly, PEABr and VBABr are nearly identical except VBA has an outermost unsaturated bond. The molecular structures of these four cations can be seen below in **Table 4**. Each cation was individually

characterized after synthesis to verify their chemical structure. **Figure 40A** shows the FT-IR spectra of both BABr and BeABr. Note that only the BeABr spectra possess the C=C stretching peak at 1644 cm^{-1} , which indicates that the outermost unsaturated bond survived the acid-base synthesis. Further, **Figure 40B** shows the proton NMR spectra of both BeABr and BABr. The spectra are identical except for the peaks between 5 and 6 ppm that are visible only in the BeABr samples. These peaks are characteristic of C=C bonds, which confirms what was observed in the FT-IR spectra. After verification of their composition, the cations were then used to make both $n=1$ and $n=2$ perovskite nanoplatelets in the LARP method described above in **Section 5.2**. Representative TEM images of $n=1$ NPLs made using each of these alkylammonium cations can be seen in below in **Figure 41**. Samples made with all alkylammonium cations possess the characteristic platelet morphology, which results in a highly extremely confined structure. This confinement can be seen in the photoluminescence spectra (**Figure 42**), as each sample displays a significantly blue shifted emission. The narrow and sharp peaks are in good agreement with what is expected from the highly confined $n=1$ and $n=2$ Ruddlesden-Popper perovskite phase, especially noting that all $n=2$ peaks are noticeable red shifted due to their decreased confinement²⁵⁸⁻

259.

Table 4 – Structure and PLQY of NPLs made with different alkylammonium cations

Alkylammonium cation	Molecule Structure	PLQY N=1 (L) ₂ PbBr ₄	PLQY N=2 (L) ₂ MAPb ₂ Br ₇
Butylammonium (BA)		12.5%	41.8%
Butene ammonium (BeA)		0.6%	36.4%
Phenylethylammonium (PEA)		4.6%	20.4%
Vinylbenzylammonium (VBA)		5.3%	34.5%

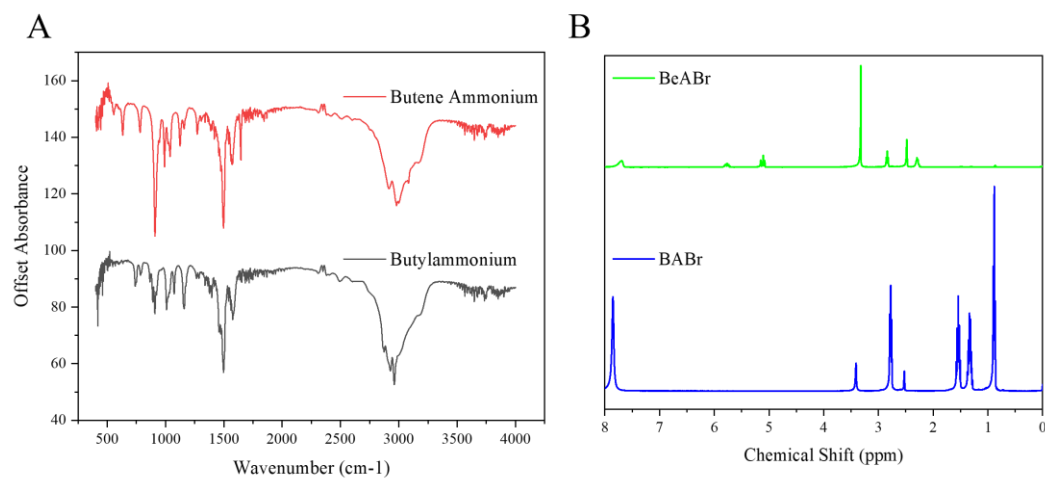


Figure 40 – Characterization of BABr and BeABr cations by (A) FT-IR and (B) NMR to verify the existence of C=C double bond

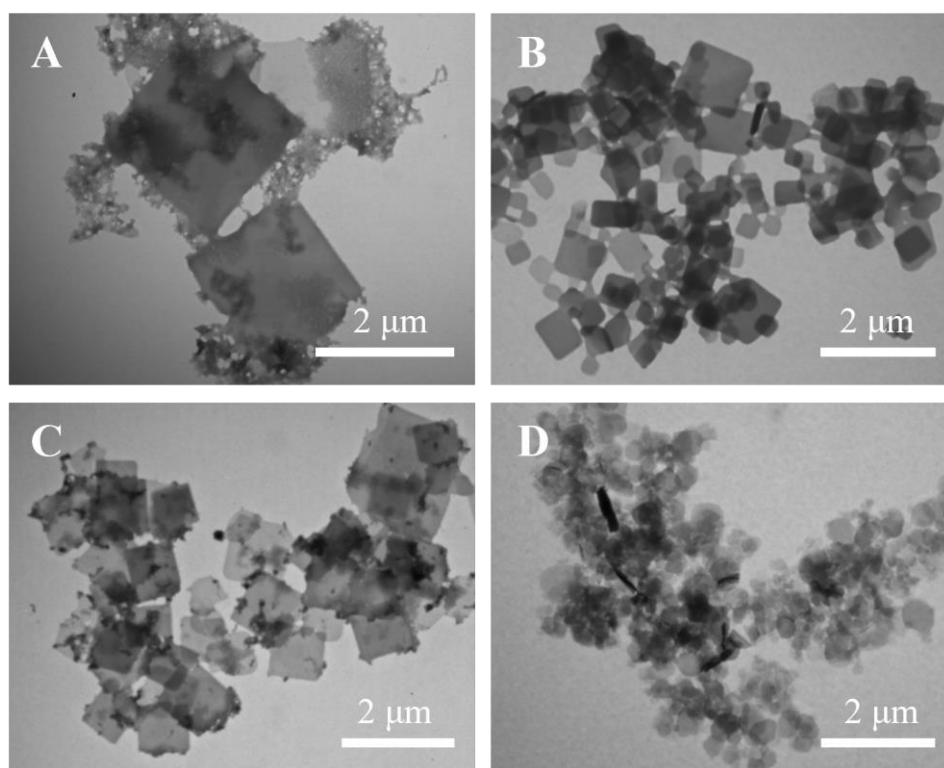


Figure 41 - TEM images of n=1 L₂PbBr₄ NPLs made with (A) BABr, (B) BeABr, (C) PEABr, and (D) VBABr

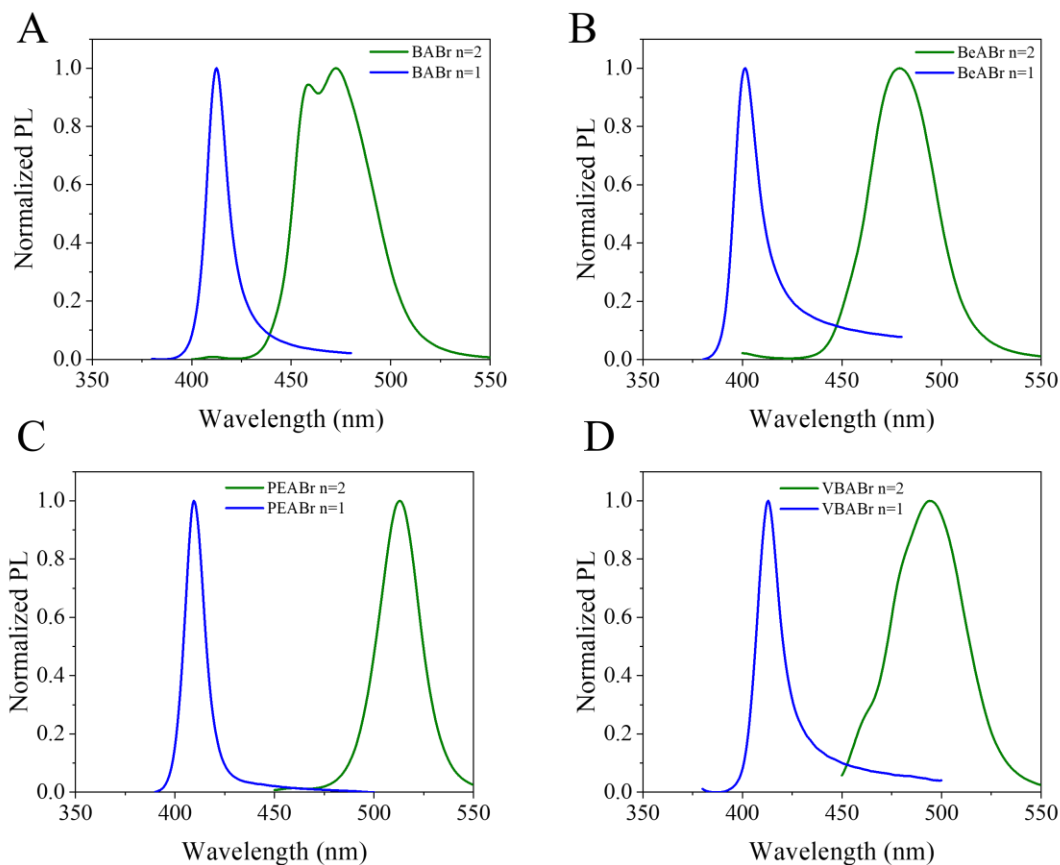


Figure 42 – PL of n=1 and n=2 NPLs made with (A) BABr, (B) BeABr, (C) PEABr, and (D) VBABr alkylammonium cations

After the NPLs made from each alkylammonium cation were synthesized and characterized, post treatment via thiol-ene crosslinking chemistry was used to enhance their stability. A diagram of the proposed architecture can be seen in **Figure 43**. The proposed research involves using thiol-ene chemistry to crosslink the outer unsaturated bonds to *in-situ* craft a covalently bound fully organic shell around each individual NPL. The hydrophobic properties of the organic shell should increase the moisture resistance of the NPLs. To achieve this crosslinking, dithiol molecules (dithiopropane or hexanedithiol

(HDT)), and the photo initiator 2,2,-dimethoxy-2-phenylacetophenone (DMPA) were added to a toluene solution of NPLs. The solution was then stirred at room temperature and irradiated with UV light to initiate the crosslinking process. During the process, aliquots of sample were removed and their optical properties were evaluated. **Figure 44** shows the progression of PLQY of $(\text{BeA})_2\text{PbBr}_4$ and $(\text{BA})_2\text{PbBr}_4$ NPLs as a function of UV irradiation. A sharp and monotonic decrease in PLQY was observed for both $(\text{BeA})_2\text{PbBr}_4$ and $(\text{BA})_2\text{PbBr}_4$ NPLs, which was likely due to UV-induced degradation of the perovskite. Though the BeABr samples were observed to retain more PLQY than the BABr samples, the near 60% decrease after only an hour was already too severe to merit further testing.

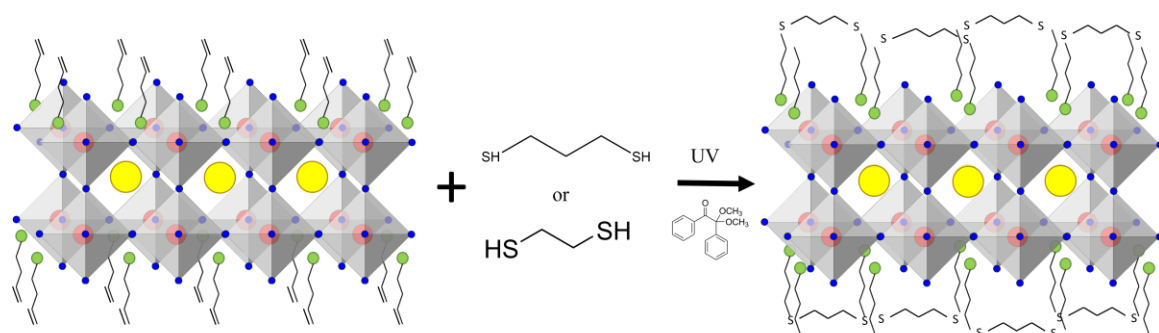


Figure 43 – Schematic of thiol-ene crosslinking unsaturated alkylammonium cations in NPLs

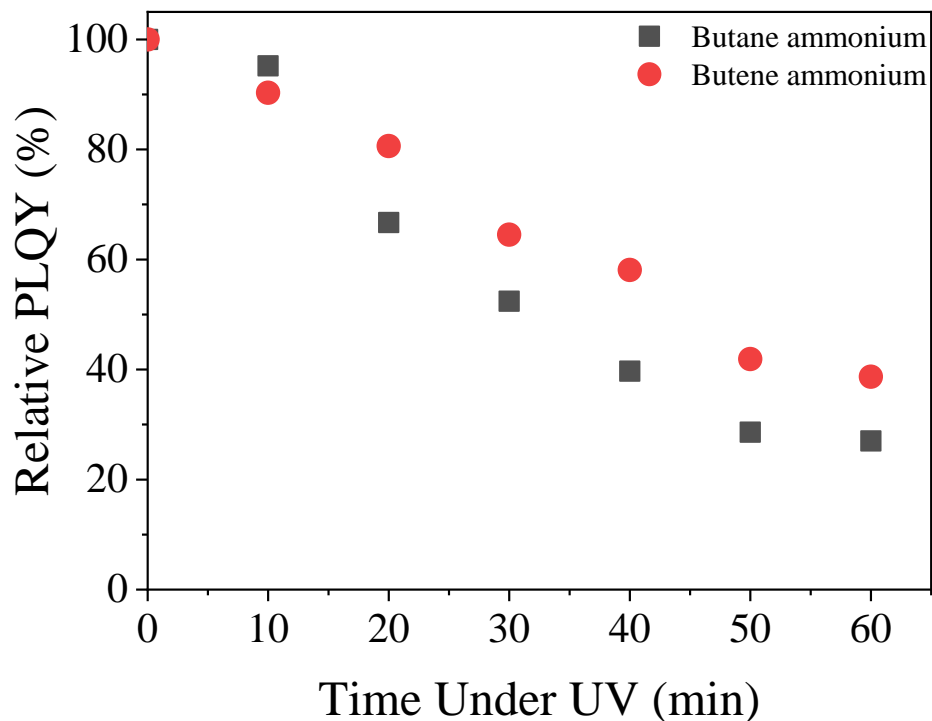


Figure 44 – Evolution of PLQY of $(\text{BeA})_2\text{PbBr}_4$ and $(\text{BA})_2\text{PbBr}_4$ NPLs during UV exposure. NPL solution included DMPA and hexanedithiol

After recognizing the sharp UV-induced degradation of BeABr and BABr NPLs, other alkylammonium cations were explored to boost stability. 4-vinylbenzylammonium bromide (VBABr) has been successfully demonstrated to photo polymerize and crosslink between Ruddlesden-Popper perovskite quantum wells²⁶⁰⁻²⁶¹. VBABr (structure seen in **Table 4**) is beneficial because its aromatic ring possesses enhanced UV absorption, which has been shown to increase the likelihood of chemical crosslinking. Further, any enhanced absorption could protect the inner perovskite nanoplatelet from unnecessary irradiation and degradation. As such, VBABr cations were synthesized and used to craft NPLs. TEM images of VBABr NPLs are seen in **Figure 41D**, and PL of VBABr NPLs are seen in

Figure 42D. Unfortunately, the PLQY of VBABr NPLs was too low (less than 5%) to justify further investigation.

After recognizing that UV-initiated crosslinking of Ruddlesden-Popper perovskite NPLs resulted in severe degradation, alternative crosslinking methods were explored. Using lower energy light that would not photodegrade the perovskite emerged as a promising technique. Sunlight²⁶² and commercial white LEDs²⁶³ have successfully been used to *in-situ* polymerize perovskite/polymer composites. Because these light sources produce lower energy photons, less degradation was seen in the perovskite. In a method similar to that reported for the UV trial, five samples were made to determine the effectiveness of white light LED crosslinking. Five samples of (BeA)₂PbBr₄ NPLs were synthesized in toluene, and their pristine photoluminescence can be seen in **Figure 45A**. Various amounts of ethane dithiol (ranging from 0-100 μ L) were then added to each of the samples with 10mg DMPA. The samples were then exposed to white light LED irradiation for 3 hours, and their PLs were again recorded (**Figure 45B**). All samples but that without any thiol presented a near full quenching in emission. This suggests that that thiol itself could be degrading the perovskite, rendering this *in-situ* crosslinking unfeasible.

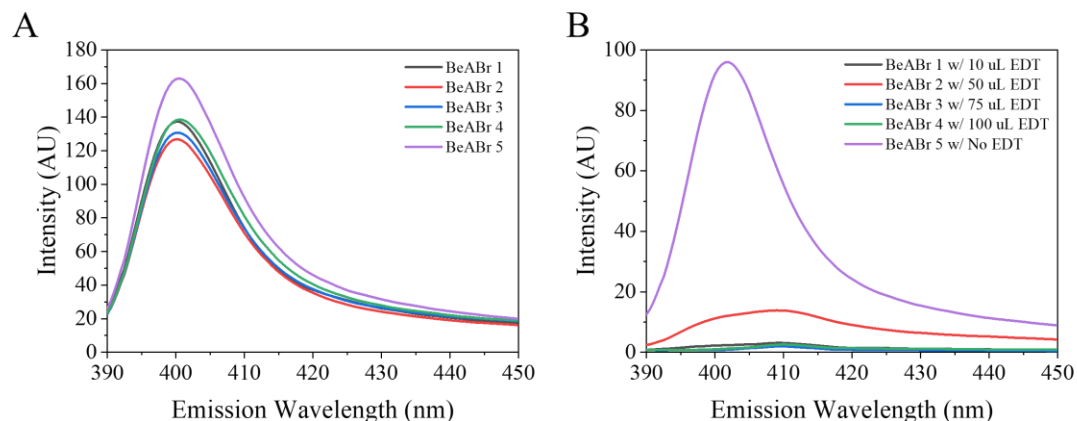


Figure 45 – PL of n=1 BeABr NPLs (A) before and (B) after illumination with LED and addition of ethane dithiol and DMPA

Based on the experience of degrading NPLs, it was determined that *in-situ* cation engineering was not worthy of further exploration. Instead, the cations could be engineered *ex-situ* and then used to synthesize highly stable perovskite NPLs. Perfluorinated cations are an ideal candidate to enhance NPL stability due to their noted super hydrophobicity. Three different perfluorinated cations were synthesized: perfluoro ethane ammonium bromide (PFEABr), perfluoro octane ammonium bromide (PFOABr), and perfluoro decane ammonium bromide (PFDABr), as illustrated in **Figure 46**. Synthesis was conducted via room temperature photoinitiated thiol-ene chemistry, as described in **Section 5.2**. The structure and composition of each perfluorinated cation was confirmed by proton NMR. **Figures 47-49** show that the C=C peaks (5-6 ppm) present in BeABr are only barely visible in the final product, signifying a near complete conversion. Further, new peaks in the 2-3 ppm range emerged for each synthesized perfluorinated cation, which verifies that new bonds were made and that the reaction was successful. PFEABr, PFOABr, and PFDABr were chosen because of their similar structures. They allow for the systematic study the effect of degree of perfluorination (1, 6, and 8 fluorinated carbons) on various

properties of the resultant NPLs. Higher degrees of perfluorination should increase hydrophobicity, which should result in greater moisture stability.

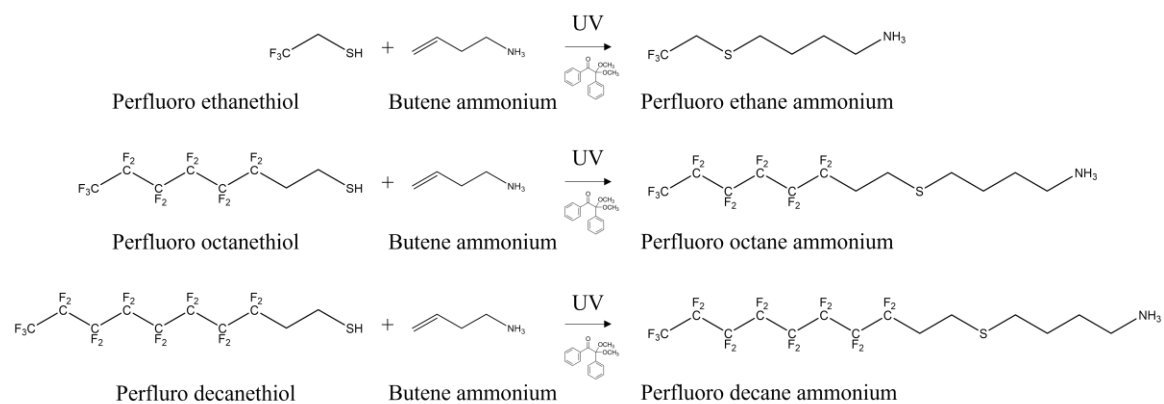


Figure 46 – Synthesis scheme for 1, 6, and 8 carbon perfluorinated cations

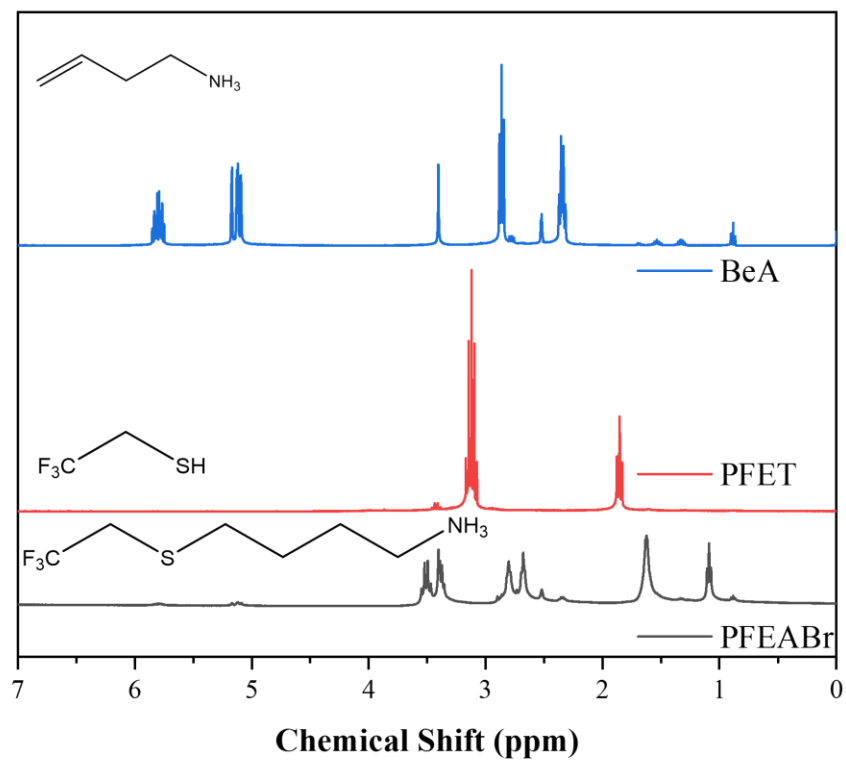


Figure 47 – NMR of BeA, perfluoro ethanethiol (PFET), and perfluoro ethane ammonium bromide

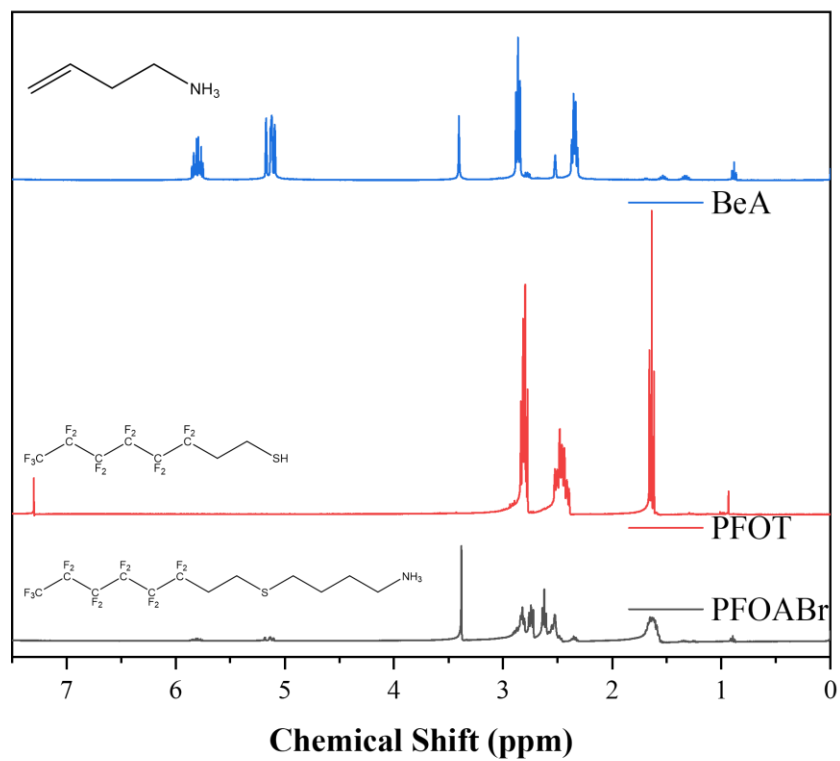


Figure 48 - NMR of BeA, perfluoro octanethiol (PFOT), and perfluoro octane ammonium bromide

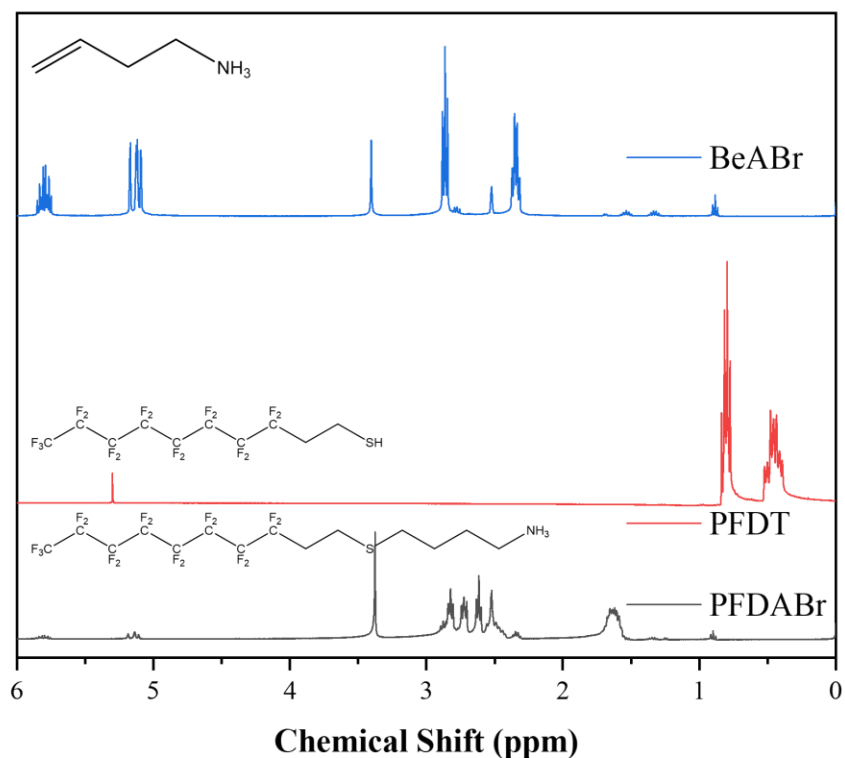


Figure 49 - NMR of BeA, perfluoro decanethiol (PFDT), and perfluoro decane ammonium bromide

The successfully synthesized perfluorinated cations were then used to craft perovskite NPLs with varying degrees of perfluorination. A summary of the optical properties of $n=1$ and $n=2$ NPLs made with each PF cation and an octylammonium (OABr) control can be seen in **Table 5**. OABr was chosen as a control because of its wholly saturated alkane nature and similar number of carbons in its chain. Unfortunately, $n=1$ NPLs made with perfluorinated cations did not register any detectable PL (OA control exhibited a PL of 0.6%). $N=2$ species did, however, all result in luminescent NPLs. This result is consistent with studies that have shown that the PLQY of perovskite increases as n does (the number of octahedral layers)²⁰⁰. Note, in this study, the monovalent A cation

was methylammonium bromide (MABr, synthetic details in the methods section). N=2 NPLs were then subjected to a water stability test in which 1 mL of deionized water was dropped into 5 mL stirring NPL/toluene solution. **Figure 51A** shows that NPLs with more fluorinated carbons had a higher peak count throughout the test (water was dropped in after time 0). **Figure 51B** further shows how perfluorinated NPLs fared better than the alkane OABr control. Both PFOABr and PFDABr maintained luminescence longer than the pure alkane OABr. Notably, PFEABr possessed poorer properties than all other samples, which suggests that a critical length and degree of perfluorination exists. This critical length theory is further suggested by the relative similarity in PFOABr and PFDABr NPL PL stability. This suggests 8 and 6 fluorinated carbons result in similar water stability and that a critical number of fluorinated carbons might exist beneath that. Regardless, this finding shows that perfluorinated cations possess a better water stability than simple alkane chains and thus ligand engineering is a promising technique.

Table 5 – Summary of optical Properties of NPLs made with perfluorinated cations

Structure	PLQY (%)	Peak (nm)	FWHM (nm)
n=1 PFDA	0	-	-
n=1 PFOA	0	-	-
n=1 PFEA	0	-	-
n=1 OA	0.6	433	22
n=2 PFDA	13.0	436.5	15
n=2 PFOA	2.4	441	19
n=2 PFEA	2.0	433	15.5
n=2 OA	33.4	436	12.5

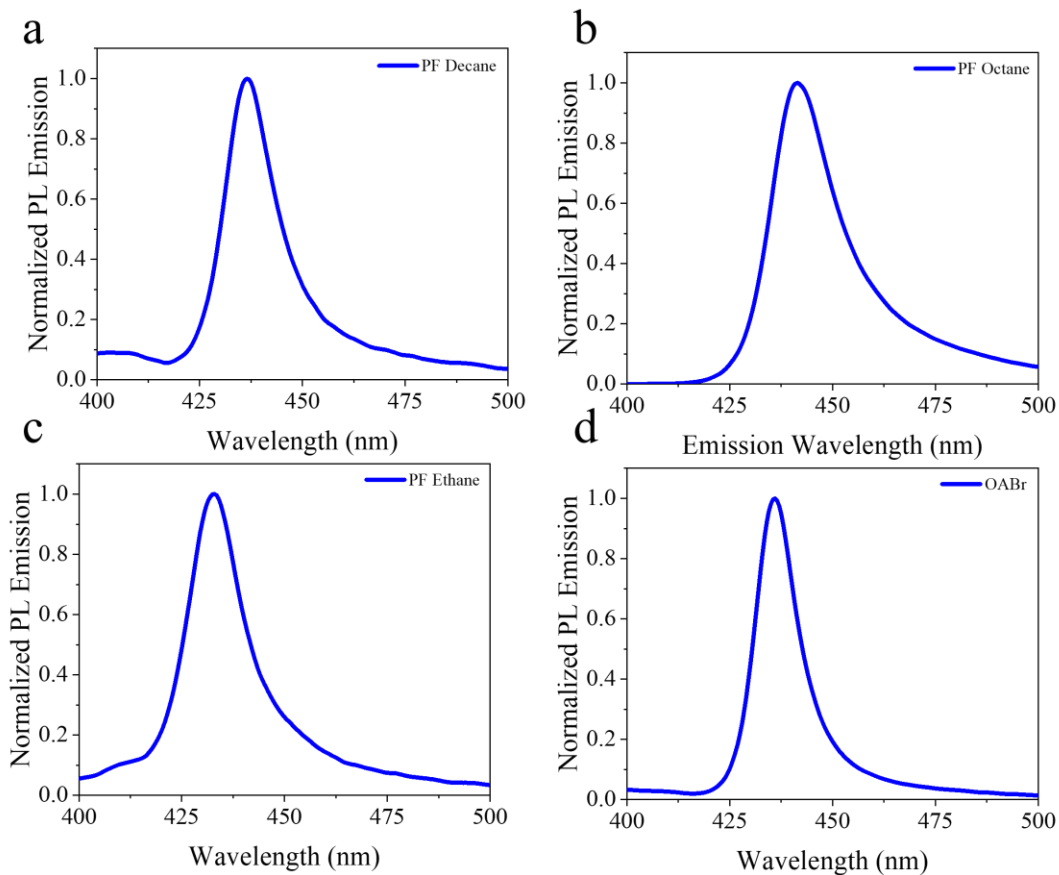


Figure 50 – PL emission spectra of n=2 NPLs made with (a) PFDABr, (b) PFOABr, (c) PFEABr, and (d) OABr cations.

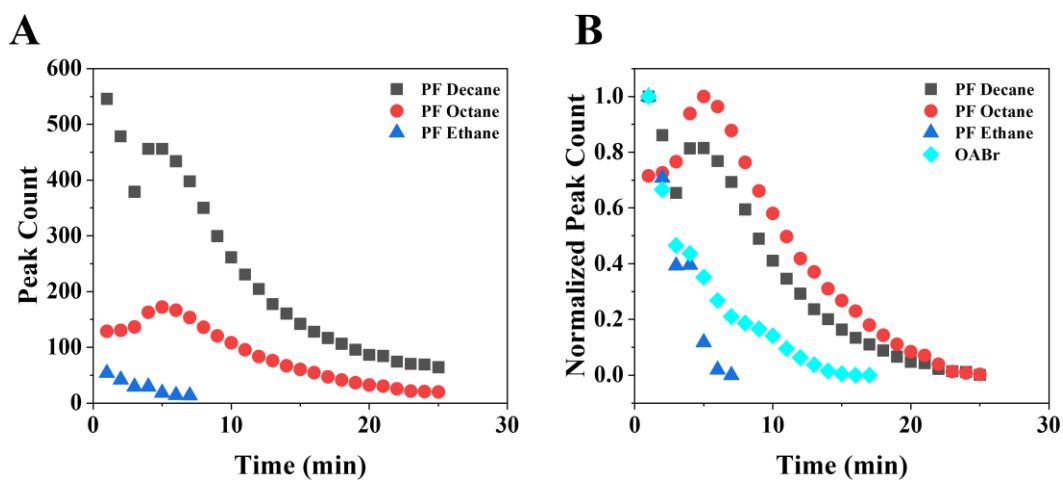


Figure 51 – PL evolution of NPLs made with perfluorinated cations. 1 mL water dropped into 5mL NPL/toluene solution

To further illustrate how perfluorinated alkylammonium cations result in enhanced water stability, the water-dependent PLQY of NPLs made with PFDABr and OABr were evaluated. PFDABr was chosen because it possessed the highest PL intensity water stability as illustrated in **Figure 51A**. **Figure 52a** depicts the evolution of PLQY of NPLs made with both OABr and PFDABr cations. After time 0, 1 mL of water was introduced into 5 mL of a stirring NPL/toluene solution. A near total quenching was observed for the OABr, with PLQY falling to less than 10% of its initial value (~4%) after only one minute (**Figure 52b**). Total quenching of PL was observed only 3 minutes after water introduction. Conversely, NPLs made with PFDABr, maintained 40% of their initial PLQY after 1 minute and then exhibited a slow decrease in PLQY over time. Notably, it took 13 minutes for PFDABr to reach 10% of its initial PLQY, which was 13 times longer than the non-perfluorinated OABr sample. This suggests that using superhydrophobic perfluorinated cations is a powerful technique that can increase stability by an order of magnitude.

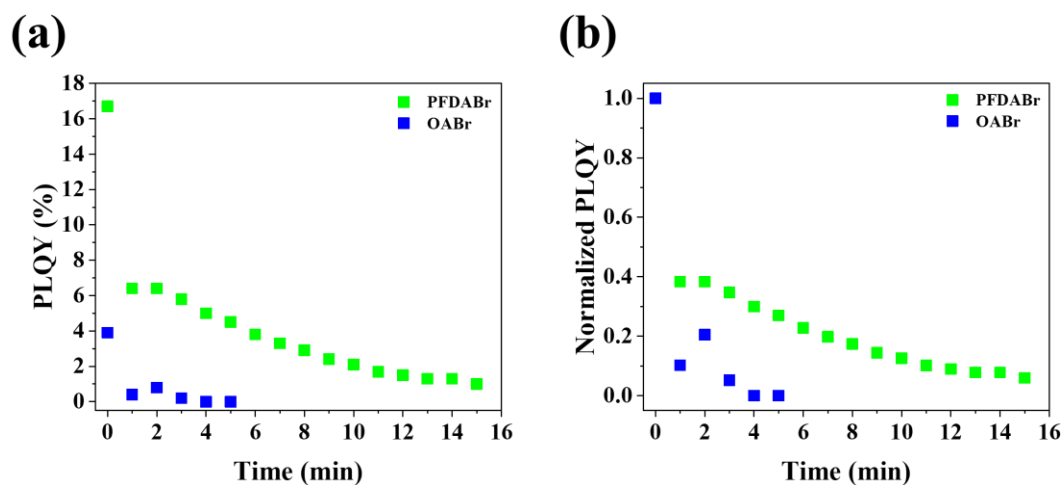


Figure 52 – Evolution of (a) absolutely and (b) normalized PLQY of NPLs made with OABr and PFDABr alkylammonium cations. 1 mL of deionized water was dropped into a 5 mL NPL/toluene solution after time 0.

5.4 Conclusion

Ruddlesden-Popper perovskites are intriguing materials with tremendous promise in a variety of optoelectronic applications. Their significant quantum confinement results in distinctly blue shifted optical properties, and their organic cations bestow significant moisture resistance. The organic/inorganic nature of RP perovskite uniquely positions it as a hybrid material with beneficial properties from both of its constituents. This study explores how powerful techniques from organic chemistry can be used to enhance the organic portion of the hybrid to account for deficiencies from the inorganic portion of RP perovskites. Specifically, thiol-ene chemistry was used to rationally engineer the alkylammonium cations to increase the moisture stability of RP perovskite. While *in-situ* thiol-ene crosslinking was unsuccessful due to UV-induced degradation of the perovskite, *ex-situ* engineering of perfluorinated cations was demonstrated to increase water stability by an order of magnitude. Further, through the systematic variation of the number of fluorinated carbons this study showed that increasing the degree of perfluorination of alkylammonium cations resulted in enhanced water stability. Thus, engineering of alkylammonium cations has been shown to be a powerful technique to enhance stability. While this study focused on using hydrophobic perfluorinated cations to enhance moisture stability, this technique could be used to create cations with various other functionalization. In theory, this universal thiol-ene technique could be used to create cations from any molecule with a thiol functionality. This technique could be used in the future to create libraries of cations with application specific functionalities, including stimuli responsivity, emission, or self-assembly.

CHAPTER 6. GENERAL CONCLUSIONS AND FUTURE RESEARCH

6.1 General Conclusions

This dissertation presents new strategies to boost the stability and production rate of lead halide perovskite nanocrystals. The recent development and intense research into lead halide perovskite have shown it to be a material with tremendous potential in numerous optoelectronic applications, including photodetectors, solar cells, scintillators, and emitters. Lead halide perovskites are particularly attractive as emitters because of their widely tunable emission wavelength, narrow full width at half max of emission, high photoluminescence quantum yield, tremendous defect tolerance, and facile room temperature synthesis. While these numerous characteristics are beneficial, there are also challenges for the widespread adoption of lead halide perovskite in commercial applications. Perovskite's inherent instability to many ambient conditions is particularly problematic. Atmospheric moisture, UV irradiation, and heat exposure have been shown to quickly degrade optical performance. Additionally, current production methods of lead halide perovskite rely on batch techniques, which are insufficient for any real-world scaling up. While these challenges appear daunting, there is good evidence that both can be overcome by a combination of new chemistry and a transition to continuous manufacturing process. This dissertation has examined three unique approaches to remedy the above-mentioned challenges, with the hope of moving perovskite toward commercialization and widespread use.

To address the issues of instability and batch production, this dissertation first examined the continuous production of highly stable lead halide perovskite nanocrystals

by integrating nonlinear block copolymer nanoreactors into a continuous flow reactor (**Chapter 3**). The polymer nanoreactors consist of inner poly(acrylic acid) and outer polystyrene blocks and were synthesized using sequential atom transfer radical polymerization of brominated beta cyclodextrin molecules. Because of the strong coordination of carboxy groups with metal moieties in the perovskite precursors, the growth of perovskite nanocrystals is confined within the poly(acrylic acid) block. Nanoreactors loaded with perovskite precursors were then placed into a house-built flow reactor to facilitate continuous production. Templated perovskite nanocrystals were then manufactured via a modified ligand assisted reprecipitation technique, where the flow dynamics of the antisolvent and precursor solution were responsible for the mixing necessary for crystallization. Numerous synthetic parameters were systematically optimized, including antisolvent composition, antisolvent injection rate, and precursor solution injection rate. Finally, the thermal, UV, and colloidal stabilities of both templated and conventional ligand perovskite nanocrystals made at the optimized conditions were evaluated. Perovskite nanocrystals made with the nanoreactor were found to be more stable in all tested scenarios, which was attributed to the permanently ligated polystyrene from the nanoreactor. This chapter serves as proof that highly stable perovskite can be made in a continuous manner needed for commercial applications.

Subsequently, this dissertation aimed to increase stability and production rate of colloidal perovskite nanocrystals by applying an in-house developed flow reactor for the continuous production of high performance two dimensional Ruddlesden-Popper perovskite nanoplatelets (**Chapter 4**). Ruddlesden-Popper perovskite is formed when the monovalent A site cations in the ABX_3 structure are replaced with bulky alkylammonium

cations. These bulky organic molecules are too large to fit within the cubo-octahedral cavity, and as such they inhibit the growth of three-dimensional crystals. This results in sheets of corner sharing octahedron with ionically attached organic molecules. Ruddlesden-Popper perovskite has been shown to possess enhanced moisture stability due to the hydrophobic nature of the organic chains on their alkylammonium cations. These higher stability perovskites were continuously manufactured by placing a precursor solution and antisolvent into a flow reactor. Both were flowed simultaneously, and the flow dynamics were responsible for the stirring necessary for crystallization. Numerous parameters were optimized, including: antisolvent composition, antisolvent flowrate, precursor solution flowrate, precursor solution concentration, and reactor tube length. The optimized conditions were then used to craft both bromide and iodide containing perovskite nanoplatelets, and their optical properties were evaluated. The iodide containing nanoplatelets exhibited performance similar to that reported in literature, and the bromide samples were better. This study showed that flow reactors can be used to continuously manufacture perovskite nanocrystals with properties equal to or greater than that of batch synthesis without the use of nanoreactors.

Finally, this dissertation explores increasing the stability of perovskite nanocrystals by using thiol-ene click chemistry to rationally engineer the alkylammonium cation in Ruddlesden-Popper perovskite (**Chapter 5**). As discussed above, the hydrophobic nature of the ionically attached alkylammonium cations on Ruddlesden-Popper perovskite has been shown to increase moisture resistance. Normally the cation consists of fully saturated carbon chains, but by creating chains with unsaturated terminal groups unique chemistries can be conducted to functionalize the perovskite. This thesis first examines using thiol-ene

crosslinking chemistry to *in-situ* create a hydrophobic organic shell to boost stability. After that, *ex-situ* cation engineering was conducted to create superhydrophobic perfluorinated cations to enhance stability. It was shown that chains with more fluorination possessed higher water stability, as demonstrated by their ability to maintain photoluminescence longer after introduction of water. This shows that rational design of the alkylammonium cations is an area rich for enhancement of Ruddlesden-Popper perovskite.

The findings reported throughout this dissertation provide general strategies to remedy the challenges that hinder the widespread adoption of metal halide perovskite for next generation optoelectronic applications. As is well documented, their poor environmental stability and reliance on batch processing are two of the most pressing challenges of metal halide perovskite. Each chapter of this dissertation responds to at least one of those obstacles and are generalizable enough to pave the way for future research.

This dissertation underscores the advantages of using both polymers and continuous flow reactors in the synthesis of perovskite nanocrystals. Specifically, **Chapter 3** showed that the stability and production rate of PNCs can be vastly increased by using nonlinear polymer nanoreactors to template the growth of perovskite nanocrystals. One key to the stability of the templated perovskite nanocrystals was the permanence of the polymer “ligands”. Therefore, this study suggests that the stability of other colloidal perovskite nanocrystals can be increased by increasing the strength of ligand binding to the surface of the nanocrystals. Unfortunately, this likely means that conventional ligands oleylamine and oleic acid are probably unsuitable for widespread production of perovskite nanocrystals, due to their highly dynamic nature. Thus, this dissertation suggests that the synthesis of PNCs with more advanced strongly-bound polymeric ligands is a strategy that could endow

further improved stabilities against multiple environmental factors. Zwitterionic ligands that possess multiple anchoring groups in conjunction with long hydrocarbon chains are a representative example of such ligands. The incorporation of zwitterionic polymers has been found to significantly enhance the stabilities of CsPbBr₃ PNC/polymer nanocomposites in polar solvents to over 1.5 years²⁶⁴. They have also been demonstrated to increase surface passivation and dispersity of PNCs in as-prepared nanocomposite thin films,¹⁰¹ which could enable practical applications of PNCs. However, the synthesis of zwitterionic polymer ligands normally requires multiple steps and yields a limited amount. Therefore, it is important to develop new polymeric ligands that can afford the same increases in stability while being more easily synthesized and scaled-up. Regardless, as shown in this dissertation, the use of polymeric ligands will be crucial for future applications of PNCs.

Chapters 4 and 5 of this dissertation emphasize the rich potential of Ruddlesden-Popper perovskite. Because RP perovskites are hybrid inorganic/organic materials, they enable the use of various unique chemistries. This dissertation has shown how new functionality and properties can be achieved by engineering the alkylammonium cations in RP perovskites. While this study focused on using superhydrophobic perfluorinated cations to increase moisture/water stability, the synthetic methods can be extended to include numerous other functionalities. This is owed in large part to the ubiquity of thiol-ene click chemistry, which enables high conversion at relatively mild conditions. Thiol-ene chemistry could be used to attach a thiol molecule with any desired functionality to an unsaturated outer bond in an alkylammonium cation, as was shown with butene ammonium and perfluorinated thiols in this dissertation.

While unsuccessful in **Chapter 5** of this dissertation, crosslinking unsaturated alkylammonium cations/ligands to create PNC/polymer nanocomposites remains an intriguing possibility. A crosslinked polymer matrix outside PNCs could provide a dense protective organic layer that inhibits the diffusion of moisture and polar solvents to the inner PNC while simultaneously limiting the ion migration in the PNC. This has been demonstrated in 3D MAPbBr₃ PNC/polymer nanocomposites that exhibited extraordinary stabilities in harsh environments (e.g. 85°C and 85% relative humidity²⁶⁵).²⁶⁶ Furthermore, selecting monomers with specific functional groups (e.g. 1-alkynyl acid) for crosslinking have been shown to increase emission of CsPbBr₃ PNCs by passivating their surface.²⁶⁷ Thus, the rational design of crosslinked polymer matrixes for the synthesis of PNC/polymer or RP NPL/polymer nanocomposites merits for further exploration.

6.2 Future Research

As this dissertation has shown, the judicious use of organic chemistry and flow reactors can remedy some of the obstacles that inhibit the use of PNCs for widespread application. Though the studies outlined in this dissertation offer many unique insights (as mentioned in **Section 6.1**), much work remains before perovskite can be widely adopted for practical uses. Based on the findings of this dissertation, the following future research directions are suggested.

First, more parameters within flow reactors should be explored for their effect on resultant PNC performance. Reactor tube diameter is one parameter that was not optimized in the studies outlined in this dissertation. Scrutinizing the effect of reactor tube diameter is crucial because of its obvious effect on the volumetric flow in the entire system. For

industrial scaling up, the diameter of the reactor tube should be maximized to enable the highest flowrates. Further, altering pipe diameter is a facile method of probing the effect of the nature of fluid flow (as described by Reynolds number) on resultant PNCs. As shown in **Equation 9**, Reynolds Number scales linearly with pipe diameter (D). Thus, by changing the pipe diameter and holding all other parameters constant, the effect of transitioning from laminar to turbulent flow can be elucidated. This is especially helpful for systems like the house-built flow reactor that have technical limits on the maximum achievable flowrate (the maximum syringe pump flowrate still falls below the turbulent regime).

Second, further alkylammonium cation engineering should be explored. This dissertation has delved into thiol-ene crosslinking and perfluorinated cations, but numerous other unique chemistries remain. As discussed in **Section 6.1**, by reacting unsaturated alkene ammonium cations with functionalized thiol-containing molecules, a nearly endless library of functional alkylammonium cations can be realized. One particularly interesting candidate for further cation engineering are stimuli-responsive molecules that could enable the properties of the resultant NPLs to be tuned on command. As a representative example, coumarin-containing alkylammonium cations could be synthesized by reacting thiol-terminated coumarin molecules with unsaturated alkylammonium cations. By creating coumarin-containing cations, the resultant NPLs could demonstrate reversible self-assembly because coumarin is well known to crosslink together under 365nm light and reversibly uncouple under 254nm light²⁶⁸. Such reversible self-assembly of perovskite NPLs could result in intriguing changes in optical properties. Further, the concentration of coumarin-containing cations could be optimized to promote either *intra* or *inter* NPL

coupling, with former enabling better moisture stability and the latter resulting in unique stacked morphologies.

Another option for further cation engineering is to incorporate organic light emitting molecules into these functional alkylammonium cations, which would enable dual emissive NPLs. As an example, anthracene has been well studied for its use as an organic emitter with widely tunable emission²⁶⁹. Additionally, anthracene possesses a structure similar to other bulky alkylammonium cations and can be easily functionalized with thiol-containing groups²⁷⁰. After reacting with unsaturated alkene ammonium cations, the anthracene-containing cations could be used to form dual emissive perovskite NPLs. Using these dual emission NPLs, devices could be made consisting of hybrid red emitting anthracene/green emitting perovskite layered on a blue-chip LED. The combined emission of all three components of this device could result in highly-desired white light. This represents only one possibility, and clearly many other compositions are possible. While this dissertation only examined engineering cations to increase moisture stability, it is clear that the studied cation engineering techniques can have much wider applications.

More broadly, through the use of both polymer nanoreactors and alkylammonium cation engineering, this dissertation has outlined the critical role that organic chemistry can play in enhancing the properties of perovskite nanocrystals. Future study in this field will likely use these and the synthesis of PNC/polymer nanocomposites to push the stabilities of perovskite towards commercialization.²⁷¹ For this to come to fruition, however, deeper study into the fundamental mechanisms of how polymers interact with PNCs is needed. For example, it is still not clear what functional groups of polymers passivate trap states of perovskites and how polymers affect the termination and surface energy of PNCs.

Additionally, how chain packing and composition of polymers affect water and oxygen diffusion and a polymers' overall contribution to electronic band structure and stability needs to be elucidated. In this context, a suite of surface analysis techniques, including vibrational spectroscopy, nuclear magnetic resonance spectroscopy, X-ray photoelectron spectroscopy, and small-angle neutron scattering technique may be needed to clarify the interactions between polymers and the PNCs.²⁷²⁻²⁷³ To optimize nanocomposites for optoelectronic applications, an in-depth understanding of the influence of polymers on charge carrier dynamics and PL decay kinetics is of key importance. Time-resolved PL, transient absorption, and time-resolved fluorescence quenching spectroscopies are some critical techniques that will allow for the exploration of structure-optoelectronic properties correlation of PNC/polymer nanocomposites.²⁷⁴⁻²⁷⁵ Furthermore, computational simulation techniques could be a powerful tool to facilitate the understanding of polymer-PNC interactions and the development of PNC/polymer nanocomposites with enhanced properties.

This work represents an important brick on the road towards the eventual commercialization of PNCs for numerous optoelectronic applications. It has offered concrete strategies to increase both the stability and production rate of PNCs, two major obstacles inhibiting widespread usage. Excitingly, the methods discussed are based in concepts that are more broadly applicable, as illustrated by Section 6.2. Future work can build on the methods developed in this dissertation to continue pushing PNCs to reach their immense potential.

DISSEMINATION OF THE WORK

1. **Biesold, G. M.**; Liang, S.; Wagner, B. K.; Kang, Z.; Lin, Z., Continuous production of ultrathin organic–inorganic Ruddlesden–Popper perovskite nanoplatelets via a flow reactor. *Nanoscale* 2021, 13 (30), 13108-13115.
2. **Biesold, G. M.**; Liang, S.; Brettmann, B.; Thadhani, N.; Kang, Z.; Lin, Z., Tailoring Optical Properties of Luminescent Semiconducting Nanocrystals through Hydrostatic, Anisotropic Static, and Dynamic Pressures. *Angewandte Chemie International Edition* 2021, 60 (18), 9772-9788.
3. **Biesold, G. M.**; Liang, S.; Wagner, B. K.; Kang, Z.; Lin, Z., Continuous manufacturing of highly stable lead halide perovskite nanocrystals via a dual-reactor strategy. *ACS Applied Nanomaterials*, (under review)
4. Fan, Q.#; **Biesold-McGee, G. V.**#; Ma, J.; Xu, Q.; Pan, S.; Peng, J.; Lin, Z., Lead-free halide perovskite nanocrystals: crystal structures, synthesis, stabilities, and optical properties. *Angewandte Chemie International Edition* 2020, 59 (3), 1030-1046. (# = co-first author)
5. Yoon, Y. J. #; **Biesold, G.**#; Liang, S.; Wang, Z.; Harn, Y. W.; Lu, C.-H.; Kim, R.; Yao, W.; Lane, S.; James, J. C., Stable Infrared-Emitting Chemical Composition Gradient Quantum Dots for Down-Convertors and Photodetectors. *ACS Applied Nano Materials* 2020, 3 (11), 11335-11343. (# = co-first author)

6. Wang, B.[#]; **Biesold, G. M.[#]**; Zhang, M.; Lin, Z., Amorphous inorganic semiconductors for the development of solar cell, photoelectrocatalytic and photocatalytic applications. *Chemical Society Reviews* 2021, 50 (12), 6914-6949. (# = co-first author)
7. Liang, S.[#]; Zhang, M.[#]; **Biesold, G. M.[#]**; Choi, W.; He, Y.; Li, Z.; Shen, D.; Lin, Z., Recent Advances in Synthesis, Properties, and Applications of Metal Halide Perovskite Nanocrystals/Polymer Nanocomposites. *Advanced Materials*. 2021, 33 (50), 2005888. (# = co-first author)
8. He, Y.; Yoon, Y. J.; Harn, Y. W.; **Biesold-McGee, G. V.**; Liang, S.; Lin, C. H.; Tsukruk, V. V.; Thadhani, N.; Kang, Z.; Lin, Z., Unconventional route to dual-shelled organolead halide perovskite nanocrystals with controlled dimensions, surface chemistry, and stabilities. *Science Advances*, 2019, 5 (11), eaax4424-eaax4424.
9. Lu, C.-H.; **Biesold-McGee, G. V.**; Liu, Y.; Kang, Z.; Lin, Z., Doping and ion substitution in colloidal metal halide perovskite nanocrystals. *Chemical Society Reviews*. 2020, 49 (14), 4953-5007.
10. Wang, Q.; Cai, J.; **Biesold-McGee, G. V.**; Huang, J.; Ng, Y. H.; Sun, H.; Wang, J.; Lai, Y.; Lin, Z., Silk fibroin-derived nitrogen-doped carbon quantum dots anchored on TiO₂ nanotube arrays for heterogeneous photocatalytic degradation and water splitting. *Nano Energy* 2020, 78, 105313.
11. Wei, P. C.; Liao, C. N.; Wu, H. J.; Yang, D.; He, J.; **Biesold-McGee, G. V.**; Liang, S.; Yen, W. T.; Tang, X.; Yeh, J. W., Thermodynamic routes to ultralow thermal

conductivity and high thermoelectric performance. *Advanced Materials* 2020, 32 (12), 1906457.

12. Dong, J.; Huang, J.; Wang, A.; **Biesold-McGee, G. V.**; Zhang, X.; Gao, S.; Wang, S.; Lai, Y.; Lin, Z., Vertically-aligned Pt-decorated MoS₂ nanosheets coated on TiO₂ nanotube arrays enable high-efficiency solar-light energy utilization for photocatalysis and self-cleaning SERS devices. *Nano Energy* 2020, 71, 104579.

13. Gomez, C. M.; Pan, S.; Braga, H. M.; de Oliveira, L. S.; Dalpian, G. M.; **Biesold-McGee, G. V.**; Lin, Z.; Santos, S. F.; Souza, J. A., Possible Charge-Transfer-Induced Conductivity Enhancement in TiO₂ Microtubes Decorated with Perovskite CsPbBr₃ Nanocrystals. *Langmuir* 2020, 36 (19), 5408-5416.

14. Ge, M.; Cao, C.; **Biesold, G. M.**; Sewell, C. D.; Hao, S. M.; Huang, J.; Zhang, W.; Lai, Y.; Lin, Z., Recent advances in silicon-based electrodes: from fundamental research toward practical applications. *Advanced Materials* 2021, 33 (16), 2004577.

15. Kang, S.; **Biesold, G. M.**; Lee, H.; Bukharina, D.; Lin, Z.; Tsukruk, V. V., Dynamic Chiro-Optics of Bio-Inorganic Nanomaterials via Seamless Co-Assembly of Semiconducting Nanorods and Polysaccharide Nanocrystals. *Advanced Functional Materials* 2021, 31 (42), 2104596.

16. Li, Z.; Tang, M.; Liang, S.; Zhang, M.; **Biesold, G. M.**; He, Y.; Hao, S.-M.; Choi, W.; Liu, Y.; Peng, J., Bottlebrush polymers: From controlled synthesis, self-assembly, properties to applications. *Progress in Polymer Science* 2021, 116, 101387.

17. Liu, F.-W.; **Biesold, G.**; Zhang, M.; Lawless, R.; Correa-Baena, J.-P.; Chueh, Y.-L.; Lin, Z., Recycling and recovery of perovskite solar cells. *Materials Today* 2021, 43, 185-197.
18. Dai, B.; **Biesold, G. M.**; Zhang, M.; Zou, H.; Ding, Y.; Wang, Z. L.; Lin, Z., Piezo-phototronic effect on photocatalysis, solar cells, photodetectors and light-emitting diodes. *Chemical Society Reviews* 2021, 50, 13646-13691.
19. Wang, W.; Zhang, M.; Pan, Z.; **Biesold, G. M.**; Liang, S.; Rao, H.; Lin, Z.; Zhong, X., Colloidal Inorganic Ligand-Capped Nanocrystals: Fundamentals, Status, and Insights into Advanced Functional Nanodevices. *Chemical Reviews* 2022, 122, 3, 4091–4162.
20. Ye, M.; **Biesold, G. M.**; Zhang, M.; Wang, W.; Bai, T.; Lin, Z., Multifunctional quantum dot materials for perovskite solar cells: Charge transport, efficiency and stability. *Nano Today* 2021, 40, 101286.
21. Zhang, M.; **Biesold, G. M.**; Lin, Z., A multifunctional 2D black phosphorene-based platform for improved photovoltaics. *Chemical Society Reviews* 2021, 50, 13346-13371.
22. Zhang, M.; **Biesold, G. M.**; Choi, W.; Yu, J.; Deng, Y.; Silvestre, C.; Lin, Z., Recent advances in polymers and polymer composites for food packaging. *Materials Today* 2022, 53, 134-161.

REFERENCES

- (1) Wells, H. L. Über die cäsium-und kalium-bleihalogenide. *Zeitschrift für anorganische Chemie* **1893**, 3 (1), 195-210.
- (2) Møller, C. K. Crystal structure and photoconductivity of caesium plumbahalides. *Nature* **1958**, 182 (4647), 1436-1436.
- (3) Kojima, A.; Teshima, K.; Shirai, Y.; Miyasaka, T. Organometal halide perovskites as visible-light sensitizers for photovoltaic cells. *Journal of the American Chemical Society* **2009**, 131 (17), 6050-6051.
- (4) Yoo, J. J.; Seo, G.; Chua, M. R.; Park, T. G.; Lu, Y.; Rotermund, F.; Kim, Y.-K.; Moon, C. S.; Jeon, N. J.; Correa-Baena, J.-P. Efficient perovskite solar cells via improved carrier management. *Nature* **2021**, 590 (7847), 587-593.
- (5) Stranks, S. D.; Eperon, G. E.; Grancini, G.; Menelaou, C.; Alcocer, M. J.; Leijtens, T.; Herz, L. M.; Petrozza, A.; Snaith, H. J. Electron-hole diffusion lengths exceeding 1 micrometer in an organometal trihalide perovskite absorber. *Science* **2013**, 342 (6156), 341-344.
- (6) Dong, Q.; Fang, Y.; Shao, Y.; Mulligan, P.; Qiu, J.; Cao, L.; Huang, J. Electron-hole diffusion lengths > 175 μm in solution-grown $\text{CH}_3\text{NH}_3\text{PbI}_3$ single crystals. *Science* **2015**, 347 (6225), 967-970.

- (7) Herz, L. M. Charge-carrier mobilities in metal halide perovskites: fundamental mechanisms and limits. *ACS Energy Letters* **2017**, *2* (7), 1539-1548.
- (8) Xing, G.; Mathews, N.; Sun, S.; Lim, S. S.; Lam, Y. M.; Grätzel, M.; Mhaisalkar, S.; Sum, T. C. Long-range balanced electron-and hole-transport lengths in organic-inorganic CH₃NH₃PbI₃. *Science* **2013**, *342* (6156), 344-347.
- (9) Shi, D.; Adinolfi, V.; Comin, R.; Yuan, M.; Alarousu, E.; Buin, A.; Chen, Y.; Hoogland, S.; Rothenberger, A.; Katsiev, K. Low trap-state density and long carrier diffusion in organolead trihalide perovskite single crystals. *Science* **2015**, *347* (6221), 519-522.
- (10) Wang, Y.; Li, X.; Zhao, X.; Xiao, L.; Zeng, H.; Sun, H. Nonlinear absorption and low-threshold multiphoton pumped stimulated emission from all-inorganic perovskite nanocrystals. *Nano letters* **2016**, *16* (1), 448-453.
- (11) Yamada, Y.; Yamada, T.; Phuong, L. Q.; Maruyama, N.; Nishimura, H.; Wakamiya, A.; Murata, Y.; Kanemitsu, Y. Dynamic optical properties of CH₃NH₃PbI₃ single crystals as revealed by one-and two-photon excited photoluminescence measurements. *Journal of the American Chemical Society* **2015**, *137* (33), 10456-10459.
- (12) Protesescu, L.; Yakunin, S.; Bodnarchuk, M. I.; Krieg, F.; Caputo, R.; Hendon, C. H.; Yang, R. X.; Walsh, A.; Kovalenko, M. V. Nanocrystals of cesium lead halide perovskites (CsPbX₃, X= Cl, Br, and I): novel optoelectronic materials showing bright emission with wide color gamut. *Nano Lett.* **2015**, *15* (6), 3692-3696.

- (13) Lan, C.; Zou, H.; Wang, L.; Zhang, M.; Pan, S.; Ma, Y.; Qiu, Y.; Wang, Z. L.; Lin, Z. Revealing Electrical-Poling-Induced Polarization Potential in Hybrid Perovskite Photodetectors. *Adv. Mater.* **2020**, *32* (47), 2005481.
- (14) Pan, S.; Zou, H.; Wang, A. C.; Wang, Z.; Yu, J.; Lan, C.; Liu, Q.; Wang, Z. L.; Lian, T.; Peng, J. Rapid Capillary-Assisted Solution Printing of Perovskite Nanowire Arrays Enables Scalable Production of Photodetectors. *Angew. Chem. Int. Ed.* **2020**, *59* (35), 14942-14949.
- (15) Ramasamy, P.; Lim, D.-H.; Kim, B.; Lee, S.-H.; Lee, M.-S.; Lee, J.-S. All-inorganic cesium lead halide perovskite nanocrystals for photodetector applications. *Chemical communications* **2016**, *52* (10), 2067-2070.
- (16) Tan, Z.; Wu, Y.; Hong, H.; Yin, J.; Zhang, J.; Lin, L.; Wang, M.; Sun, X.; Sun, L.; Huang, Y. Two-dimensional (C₄H₉NH₃)₂PbBr₄ perovskite crystals for high-performance photodetector. *Journal of the American Chemical Society* **2016**, *138* (51), 16612-16615.
- (17) Sim, K. M.; Swarnkar, A.; Nag, A.; Chung, D. S. Phase Stabilized α -CsPbI₃ Perovskite Nanocrystals for Photodiode Applications. *Laser & Photonics Reviews* **2018**, *12* (1), 1700209.
- (18) Xu, Y.; Chen, Q.; Zhang, C.; Wang, R.; Wu, H.; Zhang, X.; Xing, G.; Yu, W. W.; Wang, X.; Zhang, Y. Two-photon-pumped perovskite semiconductor nanocrystal lasers. *Journal of the American Chemical Society* **2016**, *138* (11), 3761-3768.

- (19) Wang, Y.; Li, X.; Song, J.; Xiao, L.; Zeng, H.; Sun, H. All-inorganic colloidal perovskite quantum dots: a new class of lasing materials with favorable characteristics. *Advanced materials* **2015**, *27* (44), 7101-7108.
- (20) Yakunin, S.; Protesescu, L.; Krieg, F.; Bodnarchuk, M. I.; Nedelcu, G.; Humer, M.; De Luca, G.; Fiebig, M.; Heiss, W.; Kovalenko, M. V. Erratum: Low-threshold amplified spontaneous emission and lasing from colloidal nanocrystals of caesium lead halide perovskites. *Nature communications* **2015**, *6*.
- (21) Sichert, J. A.; Tong, Y.; Mutz, N.; Vollmer, M.; Fischer, S.; Milowska, K. Z.; García Cortadella, R.; Nickel, B.; Cardenas-Daw, C.; Stolarczyk, J. K.; Urban, A. S.; Feldmann, J. Quantum Size Effect in Organometal Halide Perovskite Nanoplatelets. *Nano Letters* **2015**, *15* (10), 6521-6527, DOI: 10.1021/acs.nanolett.5b02985.
- (22) Weidman, M. C.; Goodman, A. J.; Tisdale, W. A. Colloidal Halide Perovskite Nanoplatelets: An Exciting New Class of Semiconductor Nanomaterials. *Chemistry of Materials* **2017**, *29* (12), 5019-5030, DOI: 10.1021/acs.chemmater.7b01384.
- (23) Roghabadi, F. A.; Alidaei, M.; Mousavi, S. M.; Ashjari, T.; Tehrani, A. S.; Ahmadi, V.; Sadrameli, S. M. Stability progress of perovskite solar cells dependent on the crystalline structure: From 3D ABX₃ to 2D Ruddlesden–Popper perovskite absorbers. *J Mater Chem A* **2019**, *7* (11), 5898-5933.
- (24) Chen, Y.; Sun, Y.; Peng, J.; Tang, J.; Zheng, K.; Liang, Z. 2D Ruddlesden–Popper Perovskites for Optoelectronics. *Advanced Materials* **2018**, *30* (2), 1-15, DOI: 10.1002/adma.201703487.

- (25) Kamminga, M. E.; Fang, H.-H.; Filip, M. R.; Giustino, F.; Baas, J.; Blake, G. R.; Loi, M. A.; Palstra, T. T. Confinement effects in low-dimensional lead iodide perovskite hybrids. *Chemistry of materials* **2016**, 28 (13), 4554-4562.
- (26) Zhou, J.; Chu, Y.; Huang, J. Photodetectors based on two-dimensional layer-structured hybrid lead iodide perovskite semiconductors. *ACS applied materials & interfaces* **2016**, 8 (39), 25660-25666.
- (27) Ahmad, S.; Kanaujia, P. K.; Beeson, H. J.; Abate, A.; Deschler, F.; Credgington, D.; Steiner, U.; Prakash, G. V.; Baumberg, J. J. Strong photocurrent from two-dimensional excitons in solution-processed stacked perovskite semiconductor sheets. *ACS applied materials & interfaces* **2015**, 7 (45), 25227-25236.
- (28) Cha, M.; Da, P.; Wang, J.; Wang, W.; Chen, Z.; Xiu, F.; Zheng, G.; Wang, Z.-S. Enhancing perovskite solar cell performance by interface engineering using CH₃NH₃PbBr_{0.9}I_{0.1} quantum dots. *Journal of the American Chemical Society* **2016**, 138 (27), 8581-8587.
- (29) Li, X.; Yu, D.; Cao, F.; Gu, Y.; Wei, Y.; Wu, Y.; Song, J.; Zeng, H. Healing all-inorganic perovskite films via recyclable dissolution–recrystallization for compact and smooth carrier channels of optoelectronic devices with high stability. *Advanced Functional Materials* **2016**, 26 (32), 5903-5912.
- (30) Wang, Q.; Zhang, X.; Jin, Z.; Zhang, J.; Gao, Z.; Li, Y.; Liu, S. F. Energy-down-shift CsPbCl₃: Mn quantum dots for boosting the efficiency and stability of perovskite solar cells. *ACS Energy Letters* **2017**, 2 (7), 1479-1486.

- (31) Zhang, Y.-W.; Wu, G.; Dang, H.; Ma, K.; Chen, S. Multicolored Mixed-Organic-Cation Perovskite Quantum Dots (FA x MA_{1-x} PbX₃, X= Br and I) for White Light-Emitting Diodes. *Industrial & Engineering Chemistry Research* **2017**, *56* (36), 10053-10059.
- (32) Muthu, C.; Nagamma, S. R.; Nair, V. C. Luminescent hybrid perovskite nanoparticles as a new platform for selective detection of 2, 4, 6-trinitrophenol. *RSC advances* **2014**, *4* (99), 55908-55911.
- (33) Chen, Q.; Wu, J.; Ou, X.; Huang, B.; Almutlaq, J.; Zhumeckenov, A. A.; Guan, X.; Han, S.; Liang, L.; Yi, Z. All-inorganic perovskite nanocrystal scintillators. *Nature* **2018**, *561* (7721), 88-93.
- (34) Park, S.; Chang, W. J.; Lee, C. W.; Park, S.; Ahn, H.-Y.; Nam, K. T. Photocatalytic hydrogen generation from hydriodic acid using methylammonium lead iodide in dynamic equilibrium with aqueous solution. *Nature Energy* **2016**, *2* (1), 1-8.
- (35) Xu, L.; Chen, J.; Song, J.; Li, J.; Xue, J.; Dong, Y.; Cai, B.; Shan, Q.; Han, B.; Zeng, H. Double-protected all-inorganic perovskite nanocrystals by crystalline matrix and silica for triple-modal anti-counterfeiting codes. *ACS applied materials & interfaces* **2017**, *9* (31), 26556-26564.
- (36) Lou, S.; Zhou, Z.; Xuan, T.; Li, H.; Jiao, J.; Zhang, H.; Gautier, R.; Wang, J. Chemical transformation of lead halide perovskite into insoluble, less cytotoxic, and brightly luminescent CsPbBr₃/CsPb₂Br₅ composite nanocrystals for cell imaging. *ACS applied materials & interfaces* **2019**, *11* (27), 24241-24246.

- (37) Kovalenko, M. V.; Protesescu, L.; Bodnarchuk, M. I. Properties and potential optoelectronic applications of lead halide perovskite nanocrystals. *Science* **2017**, *358* (6364), 745-750.
- (38) Gonzalez-Carrero, S.; Galian, R. E.; Pérez-Prieto, J. Maximizing the emissive properties of CH₃NH₃PbBr₃ perovskite nanoparticles. *Journal of Materials Chemistry A* **2015**, *3* (17), 9187-9193.
- (39) Gonzalez-Carrero, S.; Francés-Soriano, L.; González-Béjar, M.; Agouram, S.; Galian, R. E.; Pérez-Prieto, J. The luminescence of CH₃NH₃PbBr₃ perovskite nanoparticles crests the summit and their photostability under wet conditions is enhanced. *Small* **2016**, *12* (38), 5245-5250.
- (40) Schmidt, L. C.; Pertegás, A.; González-Carrero, S.; Malinkiewicz, O.; Agouram, S.; Minguez Espallargas, G.; Bolink, H. J.; Galian, R. E.; Pérez-Prieto, J. Nontemplate synthesis of CH₃NH₃PbBr₃ perovskite nanoparticles. *Journal of the American Chemical Society* **2014**, *136* (3), 850-853.
- (41) Hassan, Y.; Ashton, O. J.; Park, J. H.; Li, G. R.; Sakai, N.; Wenger, B.; Haghghirad, A. A.; Noel, N. K.; Song, M. H.; Lee, B. R.; Friend, R. H.; Snaith, H. J. Facile Synthesis of Stable and Highly Luminescent Methylammonium Lead Halide Nanocrystals for Efficient Light Emitting Devices. *Journal of the American Chemical Society* **2019**, *141* (3), 1269-1279, DOI: 10.1021/jacs.8b09706.
- (42) Zhang, F.; Zhong, H.; Chen, C.; Wu, X.-g.; Hu, X.; Huang, H.; Han, J.; Zou, B.; Dong, Y. Brightly Luminescent and Color-Tunable Colloidal CH₃NH₃PbX₃ (X = Br, I, Cl)

Quantum Dots: Potential Alternatives for Display Technology. *ACS Nano* **2015**, *9* (4), 4533-4542, DOI: 10.1021/acsnano.5b01154.

(43) Zhang, Y. W.; Wu, G.; Dang, H.; Ma, K. Z.; Chen, S. Multicolored Mixed-Organic-Cation Perovskite Quantum Dots (FA(x)MA(1-x)PbX₃), X = Br and I) for White Light-Emitting Diodes. *Ind Eng Chem Res* **2017**, *56* (36), 10053-10059, DOI: 10.1021/acs.iecr.7b02309.

(44) Protesescu, L.; Yakunin, S.; Bodnarchuk, M. I.; Krieg, F.; Caputo, R.; Hendon, C. H.; Yang, R. X.; Walsh, A.; Kovalenko, M. V. Nanocrystals of Cesium Lead Halide Perovskites (CsPbX₃, X = Cl, Br, and I): Novel Optoelectronic Materials Showing Bright Emission with Wide Color Gamut. *Nano Letters* **2015**, *15* (6), 3692-3696, DOI: 10.1021/nl5048779.

(45) Chouhan, L.; Ghimire, S.; Subrahmanyam, C.; Miyasaka, T.; Biju, V. Synthesis, optoelectronic properties and applications of halide perovskites. *Chem. Soc. Rev.* **2020**, *49* (10), 2869-2885.

(46) Brenner, T. M.; Egger, D. A.; Kronik, L.; Hodes, G.; Cahen, D. Hybrid organic—inorganic perovskites: low-cost semiconductors with intriguing charge-transport properties. *Nat. Rev. Mater.* **2016**, *1* (1), 1-16.

(47) Brandt, R. E.; Stevanovic, V.; Ginley, D. S.; Buonassisi, T. Identifying defect-tolerant semiconductors with high minority-carrier lifetimes: beyond hybrid lead halide perovskites. *MRS Comm.* **2015**, *5* (2), 265-275.

(48) Sze, S. M.; Ng, K. K. *Physics of semiconductor devices*, John wiley & sons: 2006.

- (49) Brenner, T. M.; Egger, D. A.; Rappe, A. M.; Kronik, L.; Hodes, G.; Cahen, D. Are mobilities in hybrid organic–inorganic halide perovskites actually “high”? *J. Phys. Chem. Lett.* **2015**, *6* (23), 4754-4757.
- (50) Milot, R. L.; Eperon, G. E.; Snaith, H. J.; Johnston, M. B.; Herz, L. M. Temperature-dependent charge-carrier dynamics in CH₃NH₃PbI₃ perovskite thin films. *Adv. Funct. Mater.* **2015**, *25* (39), 6218-6227.
- (51) Wehrenfennig, C.; Eperon, G. E.; Johnston, M. B.; Snaith, H. J.; Herz, L. M. High charge carrier mobilities and lifetimes in organolead trihalide perovskites. *Adv. Mater.* **2014**, *26* (10), 1584-1589.
- (52) Noel, N. K.; Stranks, S. D.; Abate, A.; Wehrenfennig, C.; Guarnera, S.; Haghighirad, A.-A.; Sadhanala, A.; Eperon, G. E.; Pathak, S. K.; Johnston, M. B. Lead-free organic–inorganic tin halide perovskites for photovoltaic applications. *Energy & Environmental Science* **2014**, *7* (9), 3061-3068.
- (53) Tress, W.; Marinova, N.; Inganäs, O.; Nazeeruddin, M. K.; Zakeeruddin, S. M.; Graetzel, M. Predicting the open-circuit voltage of CH₃NH₃PbI₃ perovskite solar cells using electroluminescence and photovoltaic quantum efficiency spectra: the role of radiative and non-radiative recombination. *Adv. Energy Mater.* **2015**, *5* (3), 1400812.
- (54) Nirmal, M.; Brus, L. Luminescence photophysics in semiconductor nanocrystals. *Accounts of chemical research* **1999**, *32* (5), 407-414.
- (55) Houtepen, A. J.; Hens, Z.; Owen, J. S.; Infante, I. On the origin of surface traps in colloidal II–VI semiconductor nanocrystals. *Chemistry of Materials* **2017**, *29* (2), 752-761.

- (56) Brandt, R. E.; Poindexter, J. R.; Gorai, P.; Kurchin, R. C.; Hoye, R. L.; Nienhaus, L.; Wilson, M. W.; Polizzotti, J. A.; Sereika, R.; Žaltauskas, R. Searching for “defect-tolerant” photovoltaic materials: combined theoretical and experimental screening. *Chemistry of Materials* **2017**, *29* (11), 4667-4674.
- (57) Lu, C.-H.; Biesold-McGee, G. V.; Liu, Y.; Kang, Z.; Lin, Z. Doping and ion substitution in colloidal metal halide perovskite nanocrystals. *Chem. Soc. Rev.* **2020**.
- (58) Kang, J.; Wang, L.-W. High defect tolerance in lead halide perovskite CsPbBr₃. *J Phys Chem Lett* **2017**, *8* (2), 489-493.
- (59) Dirin, D. N.; Protesescu, L.; Trummer, D.; Kochetygov, I. V.; Yakunin, S.; Krumeich, F.; Stadie, N. P.; Kovalenko, M. V. Harnessing defect-tolerance at the nanoscale: highly luminescent lead halide perovskite nanocrystals in mesoporous silica matrixes. *Nano letters* **2016**, *16* (9), 5866-5874.
- (60) Yin, W.-J.; Shi, T.; Yan, Y. Unusual defect physics in CH₃NH₃PbI₃ perovskite solar cell absorber. *Appl. Phys. Lett.* **2014**, *104* (6), 063903.
- (61) Buin, A.; Pietsch, P.; Xu, J.; Voznyy, O.; Ip, A. H.; Comin, R.; Sargent, E. H. Materials processing routes to trap-free halide perovskites. *Nano Lett.* **2014**, *14* (11), 6281-6286.
- (62) Ten Brinck, S.; Infante, I. Surface termination, morphology, and bright photoluminescence of cesium lead halide perovskite nanocrystals. *ACS Energy Lett.* **2016**, *1* (6), 1266-1272.

- (63) Hao, M.; Bai, Y.; Zeiske, S.; Ren, L.; Liu, J.; Yuan, Y.; Zarrabi, N.; Cheng, N.; Ghasemi, M.; Chen, P.; Lyu, M.; He, D.; Yun, J. H.; Du, Y.; Wang, Y.; Ding, S.; Armin, A.; Meredith, P.; Liu, G.; Cheng, H. M.; Wang, L. Ligand-assisted cation-exchange engineering for high-efficiency colloidal Cs_{1-x}FAXPbI₃ quantum dot solar cells with reduced phase segregation. *Nature Energy* **2020**, *5* (1), 79-88, DOI: 10.1038/s41560-019-0535-7.
- (64) Liang, X.; Baker, R. W.; Wu, K.; Deng, W.; Ferdani, D.; Kubiak, P. S.; Marken, F.; Torrente-Murciano, L.; Cameron, P. J. Continuous low temperature synthesis of MAPbX₃ perovskite nanocrystals in a flow reactor. *Reaction Chemistry and Engineering* **2018**, *3* (5), 640-644, DOI: 10.1039/c8re00098k.
- (65) Song, J.; Li, J.; Li, X.; Xu, L.; Dong, Y.; Zeng, H. Quantum dot light-emitting diodes based on inorganic perovskite cesium lead halides (CsPbX₃). *Adv. Mater.* **2015**, *27* (44), 7162-7167.
- (66) Vybornyi, O.; Yakunin, S.; Kovalenko, M. V. Polar-solvent-free colloidal synthesis of highly luminescent alkylammonium lead halide perovskite nanocrystals. *Nanoscale* **2016**, *8* (12), 6278-6283.
- (67) Jung, J.; Lin, C. H.; Yoon, Y. J.; Malak, S. T.; Zhai, Y.; Thomas, E. L.; Vardeny, V.; Tsukruk, V. V.; Lin, Z. Crafting Core/Graded Shell-Shell Quantum Dots with Suppressed Re-absorption and Tunable Stokes Shift as High Optical Gain Materials. *Angewandte Chemie* **2016**, *128* (16), 5155-5159.

- (68) Du, X.; Wu, G.; Cheng, J.; Dang, H.; Ma, K.; Zhang, Y.-w.; Tan, P.-f.; Chen, S. High-quality CsPbBr₃ perovskite nanocrystals for quantum dot light-emitting diodes. *RSC Advances* **2017**, 10391-10396, DOI: 10.1039/c6ra27665b.
- (69) Pu, Y.; Cai, F.; Wang, D.; Wang, J. X.; Chen, J. F., Colloidal Synthesis of Semiconductor Quantum Dots toward Large-Scale Production: A Review. *American Chemical Society*: 2018; Vol. 57, pp 1790-1802.
- (70) Akkerman, Q. A.; Rainò, G.; Kovalenko, M. V.; Manna, L. Genesis, challenges and opportunities for colloidal lead halide perovskite nanocrystals. *Nat. Mater.* **2018**, *17* (5), 394.
- (71) Xiang, W.; Liu, S. F.; Tress, W. A review on the stability of inorganic metal halide perovskites: challenges and opportunities for stable solar cells. *Energy & Environmental Science* **2021**, *14* (4), 2090-2113.
- (72) Kuno, M.; Brennan, M. C. What exactly causes light-induced halide segregation in mixed-halide perovskites? *Matter* **2020**, *2* (1), 21-23.
- (73) Beal, R. E.; Hagström, N. Z.; Barrier, J.; Gold-Parker, A.; Prasanna, R.; Bush, K. A.; Passarello, D.; Schelhas, L. T.; Brüning, K.; Tassone, C. J. Structural origins of light-induced phase segregation in organic-inorganic halide perovskite photovoltaic materials. *Matter* **2020**, *2* (1), 207-219.
- (74) Ummadisingu, A.; Steier, L.; Seo, J.-Y.; Matsui, T.; Abate, A.; Tress, W.; Grätzel, M. The effect of illumination on the formation of metal halide perovskite films. *Nature* **2017**, *545* (7653), 208-212.

- (75) Tsai, H.; Asadpour, R.; Blancon, J.-C.; Stoumpos, C. C.; Durand, O.; Strzalka, J. W.; Chen, B.; Verduzco, R.; Ajayan, P. M.; Tretiak, S. Light-induced lattice expansion leads to high-efficiency perovskite solar cells. *Science* **2018**, *360* (6384), 67-70.
- (76) Calado, P.; Telford, A. M.; Bryant, D.; Li, X.; Nelson, J.; O'Regan, B. C.; Barnes, P. R. Evidence for ion migration in hybrid perovskite solar cells with minimal hysteresis. *Nature communications* **2016**, *7* (1), 1-10.
- (77) Zhang, H.; Fu, X.; Tang, Y.; Wang, H.; Zhang, C.; Yu, W. W.; Wang, X.; Zhang, Y.; Xiao, M. Phase segregation due to ion migration in all-inorganic mixed-halide perovskite nanocrystals. *Nature communications* **2019**, *10* (1), 1-8.
- (78) Palazon, F.; Di Stasio, F.; Lauciello, S.; Krahne, R.; Prato, M.; Manna, L. Evolution of CsPbBr₃ nanocrystals upon post-synthesis annealing under an inert atmosphere. *Journal of Materials Chemistry C* **2016**, *4* (39), 9179-9182.
- (79) Yuan, X.; Hou, X.; Li, J.; Qu, C.; Zhang, W.; Zhao, J.; Li, H. Thermal degradation of luminescence in inorganic perovskite CsPbBr₃ nanocrystals. *Phys. Chem. Chem. Phys.* **2017**, *19* (13), 8934-8940.
- (80) Li, Q.; Ji, S.; Yuan, X.; Li, J.; Fan, Y.; Zhang, J.; Zhao, J.; Li, H. Ultraviolet light-induced degradation of luminescence in Mn-doped CsPbCl₃ nanocrystals. *The Journal of Physical Chemistry C* **2019**, *123* (23), 14849-14857.
- (81) Li, J.; Wang, L.; Yuan, X.; Bo, B.; Li, H.; Zhao, J.; Gao, X. Ultraviolet light induced degradation of luminescence in CsPbBr₃ perovskite nanocrystals. *Mater. Res. Bull.* **2018**, *102*, 86-91.

- (82) Glasser, L. Lattice energies of crystals with multiple ions: a generalized Kapustinskii equation. *Inorganic Chemistry* **1995**, *34* (20), 4935-4936.
- (83) Stoumpos, C. C.; Malliakas, C. D.; Peters, J. A.; Liu, Z.; Sebastian, M.; Im, J.; Chasapis, T. C.; Wibowo, A. C.; Chung, D. Y.; Freeman, A. J. Crystal growth of the perovskite semiconductor CsPbBr₃: a new material for high-energy radiation detection. *Crystal growth & design* **2013**, *13* (7), 2722-2727.
- (84) Sutton, R. J.; Eperon, G. E.; Miranda, L.; Parrott, E. S.; Kamino, B. A.; Patel, J. B.; Hörantner, M. T.; Johnston, M. B.; Haghighirad, A. A.; Moore, D. T. Bandgap-tunable cesium lead halide perovskites with high thermal stability for efficient solar cells. *Advanced Energy Materials* **2016**, *6* (8), 1502458.
- (85) Jiang, Q.; Zhang, S.; Zhao, M. Size-dependent melting point of noble metals. *Materials Chemistry and Physics* **2003**, *82* (1), 225-227.
- (86) De Roo, J.; Ibáñez, M.; Geiregat, P.; Nedelcu, G.; Walravens, W.; Maes, J.; Martins, J. C.; Van Driessche, I.; Kovalenko, M. V.; Hens, Z. Highly Dynamic Ligand Binding and Light Absorption Coefficient of Cesium Lead Bromide Perovskite Nanocrystals. *ACS Nano* **2016**, *10* (2), 2071-2081, DOI: 10.1021/acsnano.5b06295.
- (87) Owen, J. The coordination chemistry of nanocrystal surfaces. *Science* **2015**, *347* (6222), 615-616.
- (88) He, Y.; Yoon, Y. J.; Harn, Y. W.; Biesold-McGee, G. V.; Liang, S.; Lin, C. H.; Tsukruk, V. V.; Thadhani, N.; Kang, Z.; Lin, Z. Unconventional route to dual-shelled

organolead halide perovskite nanocrystals with controlled dimensions, surface chemistry, and stabilities. *Sci. Adv.* **2019**, *5* (11), eaax4424-eaax4424, DOI: 10.1126/sciadv.aax4424.

(89) Biesold, G. M.; Liang, S.; Wagner, B. K.; Kang, Z.; Lin, Z. Continuous production of ultrathin organic–inorganic Ruddlesden–Popper perovskite nanoplatelets via a flow reactor. *Nanoscale* **2021**, *13* (30), 13108-13115.

(90) Epps, R. W.; Felton, K. C.; Coley, C. W.; Abolhasani, M. Automated microfluidic platform for systematic studies of colloidal perovskite nanocrystals: Towards continuous nano-manufacturing. *Lab Chip* **2017**, *17* (23), 4040-4047, DOI: 10.1039/c7lc00884h.

(91) Li, C.; Ding, B.; Zhang, L.; Song, K.; Tao, S. 3D-printed continuous flow reactor for high yield synthesis of $\text{CH}_3\text{NH}_3\text{PbX}_3$ ($\text{X} = \text{Br}, \text{I}$) nanocrystals. *J. Mater. Chem. C* **2019**, *7* (30), 9167-9174, DOI: 10.1039/c9tc02390a.

(92) Liang, X.; Baker, R. W.; Wu, K.; Deng, W.; Ferdani, D.; Kubiak, P. S.; Marken, F.; Torrente-Murciano, L.; Cameron, P. J. Continuous low temperature synthesis of MAPbX_3 perovskite nanocrystals in a flow reactor. *React. Chem. Eng.* **2018**, *3* (5), 640-644, DOI: 10.1039/c8re00098k.

(93) Niu, G.; Ruditskiy, A.; Vara, M.; Xia, Y. Toward continuous and scalable production of colloidal nanocrystals by switching from batch to droplet reactors. *Chem Soc Rev* **2015**, *44* (16), 5806-5820, DOI: 10.1039/c5cs00049a.

(94) Song, Y. H.; Choi, S. H.; Park, W. K.; Yoo, J. S.; Kwon, S. B.; Kang, B. K.; Park, S. R.; Seo, Y. S.; Yang, W. S.; Yoon, D. H. Innovatively Continuous Mass Production

Couette-taylor Flow: Pure Inorganic Green-Emitting Cs₄PbBr₆ Perovskite Microcrystal for display technology. *Sci. Rep.* **2018**, *8* (1), 1-6, DOI: 10.1038/s41598-018-20376-3.

(95) Sui, J.; Yan, J.; Liu, D.; Wang, K.; Luo, G. Continuous Synthesis of Nanocrystals via Flow Chemistry Technology. *Small* **2020**, *16* (15), 1-23, DOI: 10.1002/sml.201902828.

(96) Wang, C.; Zhang, Y.; Wang, A.; Wang, Q.; Tang, H.; Shen, W.; Li, Z.; Deng, Z. Controlled synthesis of composition tunable formamidinium cesium double cation lead halide perovskite nanowires and nanosheets with improved stability. *Chem. Mater.* **2017**, *29* (5), 2157-2166.

(97) Berhe, T. A.; Su, W.-N.; Chen, C.-H.; Pan, C.-J.; Cheng, J.-H.; Chen, H.-M.; Tsai, M.-C.; Chen, L.-Y.; Dubale, A. A.; Hwang, B.-J. Organometal halide perovskite solar cells: degradation and stability. *Energy Environ. Sci.* **2016**, *9* (2), 323-356.

(98) Leijtens, T.; Eperon, G. E.; Noel, N. K.; Habisreutinger, S. N.; Petrozza, A.; Snaith, H. J. Stability of metal halide perovskite solar cells. *Adv. Energy Mater.* **2015**, *5* (20), 1500963.

(99) de Arquer, F. P. G.; Gong, X.; Sabatini, R. P.; Liu, M.; Kim, G.-H.; Sutherland, B. R.; Voznyy, O.; Xu, J.; Pang, Y.; Hoogland, S. Field-emission from quantum-dot-in-perovskite solids. *Nat. Commun.* **2017**, *8* (1), 1-8.

(100) Cha, W.; Kim, H.-J.; Lee, S.; Kim, J. Size-controllable and stable organometallic halide perovskite quantum dots/polymer films. *J. Mater. Chem. C* **2017**, *5* (27), 6667-6671.

- (101) Kim, H.; Hight-Huf, N.; Kang, J. H.; Bisnoff, P.; Sundararajan, S.; Thompson, T.; Barnes, M.; Hayward, R. C.; Emrick, T. Polymer Zwitterions for Stabilization of CsPbBr₃ Perovskite Nanoparticles and Nanocomposite Films. *Angew. Chem. Int. Ed.* **2020**, *59* (27), 10802-10806.
- (102) Jeong, B.; Han, H.; Kim, H. H.; Choi, W. K.; Park, Y. J.; Park, C. Polymer-Assisted Nanoimprinting for Environment-and Phase-Stable Perovskite Nanopatterns. *ACS Nano* **2020**, *14*, 1645.
- (103) He, J.; He, Z.; Towers, A.; Zhan, T.; Chen, H.; Zhou, L.; Zhang, C.; Chen, R.; Sun, T.; Gesquiere, A. J. Ligand assisted swelling–deswelling microencapsulation (LASDM) for stable, color tunable perovskite–polymer composites. *Nanoscale Adv.* **2020**, *2*, 2034.
- (104) Zhu, T.; Yang, Y.; Zheng, L.; Liu, L.; Becker, M. L.; Gong, X. Solution-Processed Flexible Broadband Photodetectors with Solution-Processed Transparent Polymeric Electrode. *Adv. Funct. Mater.* **2020**, *30*, 1909487.
- (105) Shan, Q.; Song, J.; Zou, Y.; Li, J.; Xu, L.; Xue, J.; Dong, Y.; Han, B.; Chen, J.; Zeng, H. High performance metal halide perovskite light-emitting diode: from material design to device optimization. *Small* **2017**, *13* (45), 1701770.
- (106) Yang, D.; Li, X.; Zeng, H. Surface chemistry of all inorganic halide perovskite nanocrystals: passivation mechanism and stability. *Adv. Mater. Interfaces* **2018**, *5* (8), 1701662.
- (107) Tomczak, N.; Jańczewski, D.; Han, M.; Vancso, G. J. Designer polymer–quantum dot architectures. *Prog. Polym. Sci.* **2009**, *34* (5), 393-430.

- (108) Glogowski, E.; Tangirala, R.; Russell, T. P.; Emrick, T. Functionalization of nanoparticles for dispersion in polymers and assembly in fluids. *J. Polym. Sci. A Polym. Chem.* **2006**, *44* (17), 5076-5086.
- (109) Raja, S. N.; Bekenstein, Y.; Koc, M. A.; Fischer, S.; Zhang, D.; Lin, L.; Ritchie, R. O.; Yang, P.; Alivisatos, A. P. Encapsulation of perovskite nanocrystals into macroscale polymer matrices: enhanced stability and polarization. *ACS Appl. Mater. Interfaces* **2016**, *8* (51), 35523-35533.
- (110) Righetto, M.; Meggiolaro, D.; Rizzo, A.; Sorrentino, R.; He, Z.; Meneghesso, G.; Sum, T. C.; Gatti, T.; Lamberti, F. Coupling halide perovskites with different materials: From doping to nanocomposites, beyond photovoltaics. *Prog. Mater. Sci.* **2020**, *110*, 100639.
- (111) Wang, H.; Wang, X.; Chen, R.; Zhang, H.; Wang, X.; Wang, J.; Zhang, J.; Mu, L.; Wu, K.; Fan, F. Promoting photocatalytic H₂ evolution on organic–inorganic hybrid perovskite nanocrystals by simultaneous dual-charge transportation modulation. *ACS Energy Lett.* **2018**, *4* (1), 40-47.
- (112) Yuan, J.; Ling, X.; Yang, D.; Li, F.; Zhou, S.; Shi, J.; Qian, Y.; Hu, J.; Sun, Y.; Yang, Y. Band-aligned polymeric hole transport materials for extremely low energy loss α -CsPbI₃ perovskite nanocrystal solar cells. *Joule* **2018**, *2* (11), 2450-2463.
- (113) Yoon, Y. J.; Chang, Y.; Zhang, S.; Zhang, M.; Pan, S.; He, Y.; Lin, C. H.; Yu, S.; Chen, Y.; Wang, Z.; Ding, Y.; Jung, J.; Thadhani, N.; Tsukruk, V. V.; Kang, Z.; Lin, Z. Enabling tailorable optical properties and markedly enhanced stability of perovskite

quantum dots by permanently ligating with polymer hairs. *Adv. Mater.* **2019**, *31* (32), 1901602.

(114) Chen, X.; Sun, C.; Liu, Y.; Yu, L.; Zhang, K.; Asiri, A. M.; Marwani, H. M.; Tan, H.; Ai, Y.; Wang, X. All-inorganic perovskite quantum dots CsPbX₃ (Br/I) for highly sensitive and selective detection of explosive picric acid. *Chem. Eng. J.* **2020**, *379*, 122360.

(115) Bade, S. G. R.; Shan, X.; Hoang, P. T.; Li, J.; Geske, T.; Cai, L.; Pei, Q.; Wang, C.; Yu, Z. Stretchable Light-Emitting Diodes with Organometal-Halide-Perovskite–Polymer Composite Emitters. *Adv. Mater.* **2017**, *29* (23), 1607053.

(116) Zhao, Y.; Wei, J.; Li, H.; Yan, Y.; Zhou, W.; Yu, D.; Zhao, Q. A polymer scaffold for self-healing perovskite solar cells. *Nat. Commun.* **2016**, *7*, 10228.

(117) Ling, D.; Hackett, M. J.; Hyeon, T. Surface ligands in synthesis, modification, assembly and biomedical applications of nanoparticles. *Nano Today* **2014**, *9* (4), 457-477.

(118) Sun, H.; Yang, Z.; Wei, M.; Sun, W.; Li, X.; Ye, S.; Zhao, Y.; Tan, H.; Kynaston, E. L.; Schon, T. B.; Yan, H.; Lu, Z.-H.; Ozin, G. A.; Sargent, E. H.; Seferos, D. S. Chemically Addressable Perovskite Nanocrystals for Light-Emitting Applications. *Adv. Mater.* **2017**, *29* (34), 1701153.

(119) Zhang, F.; Zhong, H.; Chen, C.; Wu, X.-g.; Hu, X.; Huang, H.; Han, J.; Zou, B.; Dong, Y. Brightly luminescent and color-tunable colloidal CH₃NH₃PbX₃ (X= Br, I, Cl) quantum dots: potential alternatives for display technology. *ACS Nano* **2015**, *9* (4), 4533-4542.

- (120) Hou, S.; Guo, Y.; Tang, Y.; Quan, Q. Synthesis and stabilization of colloidal perovskite nanocrystals by multidentate polymer micelles. *ACS applied materials & interfaces* **2017**, *9* (22), 18417-18422.
- (121) Förster, S.; Antonietti, M. Amphiphilic block copolymers in structure-controlled nanomaterial hybrids. *Adv. Mater.* **1998**, *10* (3), 195-217.
- (122) Hui, L.; Beswick, C.; Getachew, A.; Heilbrunner, H.; Liang, K.; Hanta, G.; Arbi, R.; Munir, M.; Dawood, H.; Isik Goktas, N. Reverse Micelle Templating Route to Ordered Monodispersed Spherical Organo-Lead Halide Perovskite Nanoparticles for Light Emission. *ACS Appl. Nano Mater.* **2019**, *2* (7), 4121-4132.
- (123) Hintermayr, V. A.; Lampe, C.; Löw, M.; Roemer, J.; Vanderlinden, W.; Gramlich, M.; Böhm, A. X.; Sattler, C.; Nickel, B.; Lohmüller, T.; Urban, A. S. Polymer nanoreactors shield perovskite nanocrystals from degradation. *Nano Lett.* **2019**, *19* (8), 4928-4933.
- (124) Pang, X.; Zhao, L.; Han, W.; Xin, X.; Lin, Z. A general and robust strategy for the synthesis of nearly monodisperse colloidal nanocrystals. *Nat. Nanotechnol.* **2013**, *8* (6), 426.
- (125) Leong, W. L.; Lee, P. S.; Lohani, A.; Lam, Y. M.; Chen, T.; Zhang, S.; Dodabalapur, A.; G. Mhaisalkar, S. Non-volatile organic memory applications enabled by in situ synthesis of gold nanoparticles in a self-assembled block copolymer. *Adv. Mater.* **2008**, *20* (12), 2325-2331.
- (126) Darling, S. Directing the self-assembly of block copolymers. *Prog. Polym. Sci.* **2007**, *32* (10), 1152-1204.

- (127) Pang, X.; Zhao, L.; Akinc, M.; Kim, J. K.; Lin, Z. Novel amphiphilic multi-arm, star-like block copolymers as unimolecular micelles. *Macromolecules* **2011**, *44* (10), 3746-3752.
- (128) Chen, Y.; Wang, Z.; He, Y.; Yoon, Y. J.; Jung, J.; Zhang, G.; Lin, Z. Light-enabled reversible self-assembly and tunable optical properties of stable hairy nanoparticles. *Proc. Natl. Acad. Sci. U.S.A.* **2018**, *115* (7), E1391-E1400.
- (129) Massignani, M.; LoPresti, C.; Blanz, A.; Madsen, J.; Armes, S. P.; Lewis, A. L.; Battaglia, G. Controlling cellular uptake by surface chemistry, size, and surface topology at the nanoscale. *Small* **2009**, *5* (21), 2424-2432.
- (130) Liu, Y.; Wang, Z.; Liang, S.; Li, Z.; Zhang, M.; Li, H.; Lin, Z. Polar Organic Solvent-Tolerant Perovskite Nanocrystals Permanently Ligated with Polymer Hairs via Star-like Molecular Bottlebrush Trilobe Nanoreactors. *Nano Letters* **2019**, *19* (12), 9019-9028, DOI: 10.1021/acs.nanolett.9b04047.
- (131) He, Y.; Yoon, Y. J.; Harn, Y. W.; Biesold-McGee, G. V.; Liang, S.; Lin, C. H.; Tsukruk, V. V.; Thadhani, N.; Kang, Z.; Lin, Z. Unconventional route to dual-shelled organolead halide perovskite nanocrystals with controlled dimensions, surface chemistry, and stabilities. *Sci. Adv.* **2019**, *5* (11), eaax4424.
- (132) Pan, S.; Chen, Y.; Wang, Z.; Harn, Y.-W.; Yu, J.; Wang, A.; Smith, M. J.; Li, Z.; Tsukruk, V. V.; Peng, J.; Lin, Z. Strongly-ligated perovskite quantum dots with precisely controlled dimensions and architectures for white light-emitting diodes. *Nano Energy* **2020**, 105043.

- (133) Yoon, Y. J.; Chang, Y.; Zhang, S.; Zhang, M.; Pan, S.; He, Y.; Lin, C. H.; Yu, S.; Chen, Y.; Wang, Z.; Ding, Y.; Jung, J.; Thadhani, N.; Tsukruk, V. V.; Kang, Z.; Lin, Z. Enabling Tailorable Optical Properties and Markedly Enhanced Stability of Perovskite Quantum Dots by Permanently Ligating with Polymer Hairs. *Adv. Mater.* **2019**, 1901602-1901602, DOI: 10.1002/adma.201901602.
- (134) Acharyya, P.; Maji, K.; Kundu, K.; Biswas, K. 2D Nanoplates and Scaled-Up Bulk Polycrystals of Ruddlesden-Popper Cs₂PbI₂Cl₂ for Optoelectronic Applications. *ACS Applied Nano Materials* **2020**, 3 (1), 877-886, DOI: 10.1021/acsnm.9b02439.
- (135) Cao, Y.; Wang, N.; Tian, H.; Guo, J.; Wei, Y.; Chen, H.; Miao, Y.; Zou, W.; Pan, K.; He, Y.; Cao, H.; Ke, Y.; Xu, M.; Wang, Y.; Yang, M.; Du, K.; Fu, Z.; Kong, D.; Dai, D.; Jin, Y.; Li, G.; Li, H.; Peng, Q.; Wang, J.; Huang, W. Perovskite light-emitting diodes based on spontaneously formed submicrometre-scale structures. *Nature* **2018**, 562 (7726), 249-253, DOI: 10.1038/s41586-018-0576-2.
- (136) Chen, C.; Gao, L.; Gao, W.; Ge, C.; Du, X.; Li, Z.; Yang, Y.; Niu, G.; Tang, J. Circularly polarized light detection using chiral hybrid perovskite. *Nat Commun* **2019**, 10 (1), 1-7, DOI: 10.1038/s41467-019-09942-z.
- (137) Chen, Q.; Wu, J.; Ou, X.; Huang, B.; Almutlaq, J.; Zhumekenov, A. A.; Guan, X.; Han, S.; Liang, L.; Yi, Z.; Li, J.; Xie, X.; Wang, Y.; Li, Y.; Fan, D.; Teh, D. B. L.; All, A. H.; Mohammed, O. F.; Bakr, O. M.; Wu, T.; Bettinelli, M.; Yang, H.; Huang, W.; Liu, X., All-inorganic perovskite nanocrystal scintillators. Nature Publishing Group: 2018; Vol. 561, pp 88-93.

- (138) Wang, K.; Zhang, H.; Gu, Z. J. All-inorganic perovskite nanocrystal materials: new generation of scintillators for high quality X-ray imaging. *Sci Bull* **2019**, *64* (17), 1205-1206, DOI: 10.1016/j.scib.2019.07.009.
- (139) Zhang, M.; Ye, M.; Wang, W.; Ma, C.; Wang, S.; Liu, Q.; Lian, T.; Huang, J.; Lin, Z. Synergistic Cascade Carrier Extraction via Dual Interfacial Positioning of Ambipolar Black Phosphorene for High-Efficiency Perovskite Solar Cells. *Adv. Mater.* **2020**, *32* (28), 2000999.
- (140) Wang, B.; Zhang, M.; Cui, X.; Wang, Z.; Rager, M.; Yang, Y.; Zou, Z.; Wang, Z. L.; Lin, Z. Unconventional Route to Oxygen-Vacancy-Enabled Highly Efficient Electron Extraction and Transport in Perovskite Solar Cells. *Angew. Chem. Int. Ed.* **2019**, ange.201910471-ange.201910471, DOI: 10.1002/ange.201910471.
- (141) Akkerman, Q. A.; Gandini, M.; Di Stasio, F.; Rastogi, P.; Palazon, F.; Bertoni, G.; Ball, J. M.; Prato, M.; Petrozza, A.; Manna, L. Strongly emissive perovskite nanocrystal inks for high-voltage solar cells. *Nature Energy* **2017**, *2* (2), 1-7, DOI: 10.1038/nenergy.2016.194.
- (142) Lu, C.-H.; Biesold-McGee, G. V.; Liu, Y.; Kang, Z.; Lin, Z. Doping and ion substitution in colloidal metal halide perovskite nanocrystals. *Chem Soc Rev* **2020**, *49* (14), 4953-5007.
- (143) Gonzalez-Carrero, S.; Frances-Soriano, L.; Gonzalez-Bejar, M.; Agouram, S.; Galian, R. E.; Perez-Prieto, J. The Luminescence of CH₃NH₃PbBr₃ Perovskite

Nanoparticles Crests the Summit and Their Photostability under Wet Conditions is Enhanced. *Small* **2016**, *12* (38), 5245-5250, DOI: 10.1002/sml.201600209.

(144) Gonzalez-Carrero, S.; Galian, R. E.; Perez-Prieto, J. Maximizing the emissive properties of CH₃NH₃PbBr₃ perovskite nanoparticles. *J Mater Chem A* **2015**, *3* (17), 9187-9193, DOI: 10.1039/c4ta05878j.

(145) Liu, F.; Zhang, Y.; Ding, C.; Kobayashi, S.; Izuishi, T.; Nakazawa, N.; Toyoda, T.; Ohta, T.; Hayase, S.; Minemoto, T. Highly luminescent phase-stable CsPbI₃ perovskite quantum dots achieving near 100% absolute photoluminescence quantum yield. *ACS nano* **2017**, *11* (10), 10373-10383.

(146) Bai, S.; Yuan, Z.; Gao, F. Colloidal metal halide perovskite nanocrystals: synthesis, characterization, and applications. *J Mater Chem C* **2016**, *4* (18), 3898-3904.

(147) Wei, S.; Yang, Y.; Kang, X.; Wang, L.; Huang, L.; Pan, D. Room-temperature and gram-scale synthesis of CsPbX₃ (X= Cl, Br, I) perovskite nanocrystals with 50–85% photoluminescence quantum yields. *Chemical Communications* **2016**, *52* (45), 7265-7268.

(148) Huang, H.; Bodnarchuk, M. I.; Kershaw, S. V.; Kovalenko, M. V.; Rogach, A. L. Lead halide perovskite nanocrystals in the research spotlight: Stability and defect tolerance. *ACS Energy Lett.* **2017**, *2* (9), 2071-2083.

(149) Ha, S. K.; Mauck, C. M.; Tisdale, W. A. Toward Stable Deep-Blue Luminescent Colloidal Lead Halide Perovskite Nanoplatelets: Systematic Photostability Investigation. *Chem. Mater.* **2019**, *31* (7), 2486-2496, DOI: 10.1021/acs.chemmater.8b05310.

(150) Carbone, L.; Nobile, C.; De Giorgi, M.; Della Sala, F.; Morello, G.; Pompa, P.; Hytch, M.; Snoeck, E.; Fiore, A.; Franchini, I. R.; Nadasan, M.; Silvestre, A. F.; Chiodo, L.; Kudera, S.; Cingolani, R.; Krahn, R.; Manna, L. Synthesis and micrometer-scale assembly of colloidal CdSe/CdS nanorods prepared by a seeded growth approach. *Nano Lett.* **2007**, *7* (10), 2942-2950, DOI: 10.1021/nl0717661.

(151) Pedrueza, E.; Segura, A.; Abargues, R.; Bailach, J. B.; Chervin, J. C.; Martínez-Pastor, J. P. The effect of quantum size confinement on the optical properties of PbSe nanocrystals as a function of temperature and hydrostatic pressure. *Nanotechnology* **2013**, *24* (20), 205701-205701, DOI: 10.1088/0957-4484/24/20/205701.

(152) Kang, Z.; Banishev, A. A.; Lee, G.; Scripka, D. A.; Breidenich, J.; Xiao, P.; Christensen, J.; Zhou, M.; Summers, C. J.; Dlott, D. D.; Thadhani, N. N. Exploration of CdTe quantum dots as mesoscale pressure sensors via time-resolved shock-compression photoluminescent emission spectroscopy. *J Phys D Appl Phys* **2016**, *120* (4), 043107-043107, DOI: 10.1063/1.4959257.

(153) Smith, I. C.; Hoke, E. T.; Solis-Ibarra, D.; McGehee, M. D.; Karunadasa, H. I. A layered hybrid perovskite solar-cell absorber with enhanced moisture stability. *Angew. Chem. Int. Ed.* **2014**, *126* (42), 11414-11417.

(154) Lin, Y.; Bai, Y.; Fang, Y.; Chen, Z.; Yang, S.; Zheng, X.; Tang, S.; Liu, Y.; Zhao, J.; Huang, J. Enhanced thermal stability in perovskite solar cells by assembling 2D/3D stacking structures. *J Phys Chem Lett* **2018**, *9* (3), 654-658.

- (155) Bella, F.; Griffini, G.; Correa-Baena, J.-P.; Saracco, G.; Grätzel, M.; Hagfeldt, A.; Turri, S.; Gerbaldi, C. Improving efficiency and stability of perovskite solar cells with photocurable fluoropolymers. *Science* **2016**, *354* (6309), 203-206.
- (156) Levchuk, I.; Osvet, A.; Tang, X.; Brandl, M.; Perea, J. D.; Hoegl, F.; Matt, G. J.; Hock, R.; Batentschuk, M.; Brabec, C. J. Brightly luminescent and color-tunable formamidinium lead halide perovskite FAPbX₃ (X= Cl, Br, I) colloidal nanocrystals. *Nano Lett.* **2017**, *17* (5), 2765-2770.
- (157) Loiudice, A.; Saris, S.; Oveisi, E.; Alexander, D. T.; Buonsanti, R. CsPbBr₃ QD/AlOx inorganic nanocomposites with exceptional stability in water, light, and heat. *Angew. Chem. Int. Ed.* **2017**, *56* (36), 10696-10701.
- (158) Chang, Y.; Yoon, Y. J.; Li, G.; Xu, E.; Yu, S.; Lu, C.-H.; Wang, Z.; He, Y.; Lin, C. H.; Wagner, B. K.; Tsukruk, V. V.; Kang, Z.; Thadhani, N.; Jiang, Y.; Lin, Z. All-Inorganic Perovskite Nanocrystals with a Stellar Set of Stabilities and Their Use in White Light-Emitting Diodes. *ACS Appl. Mater. Interfaces* **2018**, *10* (43), 37267-37276, DOI: 10.1021/acsami.8b13553.
- (159) Liang, S.; Zhang, M.; Biesold, G. M.; Choi, W.; He, Y.; Li, Z.; Shen, D.; Lin, Z. Recent Advances in Synthesis, Properties, and Applications of Metal Halide Perovskite Nanocrystals/Polymer Nanocomposites. *Adv. Mater.* **2021**, *33* (50), 2005888.
- (160) He, Y.; Yoon, Y. J.; Harn, Y. W.; Biesold-McGee, G. V.; Liang, S.; Lin, C. H.; Tsukruk, V. V.; Thadhani, N.; Kang, Z.; Lin, Z. Unconventional route to dual-shelled organolead halide perovskite nanocrystals with controlled dimensions, surface chemistry,

and stabilities. *Science advances* **2019**, *5* (11), eaax4424-eaax4424, DOI: 10.1126/sciadv.aax4424.

(161) Yoon, Y. J.; Chang, Y.; Zhang, S.; Zhang, M.; Pan, S.; He, Y.; Lin, C. H.; Yu, S.; Chen, Y.; Wang, Z.; Ding, Y.; Jung, J.; Thadhani, N.; Tsukruk, V. V.; Kang, Z.; Lin, Z. Enabling Tailorable Optical Properties and Markedly Enhanced Stability of Perovskite Quantum Dots by Permanently Ligating with Polymer Hairs. *Adv. Mater.* **2019**, 1901602-1901602, DOI: 10.1002/adma.201901602.

(162) Pan, S.; Chen, Y.; Wang, Z.; Harn, Y.-W.; Yu, J.; Wang, A.; Smith, M. J.; Li, Z.; Tsukruk, V. V.; Peng, J. Strongly-ligated perovskite quantum dots with precisely controlled dimensions and architectures for white light-emitting diodes. *Nano Energy* **2020**, *77*, 105043.

(163) Liu, Y.; Wang, J.; Zhang, M.; Li, H.; Lin, Z. Polymer-Ligated Nanocrystals Enabled by Nonlinear Block Copolymer Nanoreactors: Synthesis, Properties, and Applications. *ACS nano* **2020**, *14* (10), 12491-12521.

(164) Pang, X.; Zhao, L.; Han, W.; Xin, X.; Lin, Z. A general and robust strategy for the synthesis of nearly monodisperse colloidal nanocrystals. *Nat. Nanotechnol.* **2013**, *8* (6), 426-431.

(165) Epps, R. W.; Felton, K. C.; Coley, C. W.; Abolhasani, M. Automated microfluidic platform for systematic studies of colloidal perovskite nanocrystals: Towards continuous nano-manufacturing. *Lab Chip* **2017**, *17* (23), 4040-4047, DOI: 10.1039/c7lc00884h.

- (166) Lignos, I.; Stavrakis, S.; Nedelcu, G.; Protesescu, L.; Demello, A. J.; Kovalenko, M. V. Synthesis of Cesium Lead Halide Perovskite Nanocrystals in a Droplet-Based Microfluidic Platform: Fast Parametric Space Mapping. *Nano Lett.* **2016**, *16* (3), 1869-1877, DOI: 10.1021/acs.nanolett.5b04981.
- (167) Maceiczky, R. M.; Dümbgen, K.; Lignos, I.; Protesescu, L.; Kovalenko, M. V.; deMello, A. J. Microfluidic Reactors Provide Preparative and Mechanistic Insights into the Synthesis of Formamidinium Lead Halide Perovskite Nanocrystals. *Chem. Mater.* **2017**, *29* (19), 8433-8439, DOI: 10.1021/acs.chemmater.7b02998.
- (168) Song, Y. H.; Choi, S. H.; Park, W. K.; Yoo, J. S.; Kwon, S. B.; Kang, B. K.; Park, S. R.; Seo, Y. S.; Yang, W. S.; Yoon, D. H. Innovatively Continuous Mass Production Couette-taylor Flow: Pure Inorganic Green-Emitting Cs₄PbBr₆ Perovskite Microcrystal for display technology. *Sci Rep* **2018**, *8* (1), 1-6, DOI: 10.1038/s41598-018-20376-3.
- (169) Li, C.; Ding, B.; Zhang, L.; Song, K.; Tao, S. 3D-printed continuous flow reactor for high yield synthesis of CH₃NH₃PbX₃ (X = Br, I) nanocrystals. *J Mater Chem C* **2019**, *7* (30), 9167-9174, DOI: 10.1039/c9tc02390a.
- (170) Xu, Y.; Li, W.; Qiu, F.; Lin, Z. Self-assembly of 21-arm star-like diblock copolymer in bulk and under cylindrical confinement. *Nanoscale* **2014**, *6* (12), 6844-6852.
- (171) Li, H.; Liu, B.; Zhang, X.; Gao, C.; Shen, J.; Zou, G. Single-molecule force spectroscopy on poly (acrylic acid) by AFM. *Langmuir* **1999**, *15* (6), 2120-2124.
- (172) Bruzzi, M.; Talamonti, C. Characterization of Crystalline CsPbBr₃ Perovskite Dosimeters for Clinical Radiotherapy. *Frontiers in Physics* **2021**, *36*.

- (173) Liang, S.; Zhang, M.; He, Y.; Kang, Z.; Tian, M.; Zhang, M.; Miao, H.; Lin, Z. Polymer-Ligated Uniform Lead Chalcogenide Nanoparticles with Tunable Size and Robust Stability Enabled by Judiciously Designed Surface Chemistry. *Chem. Mater.* **2021**, *33* (17), 6701-6712.
- (174) Hu, H.; Saniger, J.; Garcia-Alejandre, J.; Castaño, V. Fourier transform infrared spectroscopy studies of the reaction between polyacrylic acid and metal oxides. *Materials Letters* **1991**, *12* (4), 281-285.
- (175) Pang, X.; He, Y.; Jung, J.; Lin, Z. 1D nanocrystals with precisely controlled dimensions, compositions, and architectures. *Science* **2016**, *353* (6305), 1268-1272, DOI: 10.1126/science.aad8279.
- (176) Wang, Y.; He, J.; Chen, H.; Chen, J.; Zhu, R.; Ma, P.; Towers, A.; Lin, Y.; Gesquiere, A. J.; Wu, S. T. Ultrastable, highly luminescent organic–inorganic perovskite–polymer composite films. *Adv. Mater.* **2016**, *28* (48), 10710-10717.
- (177) Smallwood, I. M., Handbook of organic solvent properties. Arnold Halsted Press: London, New York, 1996; pp. 1 online resource (xxi, 306 pages).
- (178) Huo, H.; Li, K.; Wang, Q.; Wu, C. Self-assembly and optical property of triblock copolymers made of polystyrene and oligo (p-phenyleneethynylene) in different mixtures of toluene and hexane. *Macromolecules* **2007**, *40* (18), 6692-6698.
- (179) Darbyshire, A.; Mullin, T. Transition to turbulence in constant-mass-flux pipe flow. *Journal of Fluid Mechanics* **1995**, *289*, 83-114.

- (180) Sharp, K. V.; Adrian, R. J. Transition from laminar to turbulent flow in liquid filled microtubes. *Experiments in fluids* **2004**, *36* (5), 741-747.
- (181) Nagy, K. D.; Shen, B.; Jamison, T. F.; Jensen, K. F. Mixing and dispersion in small-scale flow systems. *Organic Process Research & Development* **2012**, *16* (5), 976-981.
- (182) Esparza, D.; Sidhik, S.; López-Luke, T.; Rivas, J. M.; De la Rosa, E. Light-induced effects on crystal size and photo-stability of colloidal CsPbBr₃ perovskite nanocrystals. *Materials Research Express* **2019**, *6* (4), 045041.
- (183) Han, Q.; Wu, W.; Liu, W.; Yang, Y. The peak shift and evolution of upconversion luminescence from CsPbBr₃ nanocrystals under femtosecond laser excitation. *RSC advances* **2017**, *7* (57), 35757-35764.
- (184) Li, J.; Wang, L.; Yuan, X.; Bo, B.; Li, H.; Zhao, J.; Gao, X. Ultraviolet light induced degradation of luminescence in CsPbBr₃ perovskite nanocrystals. *Materials Research Bulletin* **2018**, *102*, 86-91.
- (185) Li, T.; Zhou, C.; Jiang, M. UV absorption spectra of polystyrene. *Polymer Bulletin* **1991**, *25* (2), 211-216.
- (186) Yuan, X.; Hou, X.; Li, J.; Qu, C.; Zhang, W.; Zhao, J.; Li, H. Thermal degradation of luminescence in inorganic perovskite CsPbBr₃ nanocrystals. *Physical Chemistry Chemical Physics* **2017**, *19* (13), 8934-8940.

- (187) He, M.; Pang, X.; Liu, X.; Jiang, B.; He, Y.; Snaith, H.; Lin, Z. Monodisperse dual-functional upconversion nanoparticles enabled near-infrared organolead halide perovskite solar cells. *Angew. Chem. Int. Ed.* **2016**, *128* (13), 4352-4356.
- (188) Ye, M.; He, C.; Iocozzia, J.; Liu, X.; Cui, X.; Meng, X.; Rager, M.; Hong, X.; Liu, X.; Lin, Z. Recent advances in interfacial engineering of perovskite solar cells. *J Phys D Appl Phys* **2017**, *50* (37), 373002.
- (189) He, M.; Li, B.; Cui, X.; Jiang, B.; He, Y.; Chen, Y.; O'Neil, D.; Szymanski, P.; Eiyayed, M. A.; Huang, J.; Lin, Z. Meniscus-assisted solution printing of large-grained perovskite films for high-efficiency solar cells. *Nat Commun* **2017**, *8* (1).
- (190) Liu, F.-W.; Biesold, G.; Zhang, M.; Lawless, R.; Correa-Baena, J.-P.; Chueh, Y.-L.; Lin, Z. Recycling and recovery of perovskite solar cells. *Materials Today* **2021**.
- (191) Chang, Y.; Yoon, Y. J.; Li, G.; Xu, E.; Yu, S.; Lu, C.-H.; Wang, Z.; He, Y.; Lin, C. H.; Wagner, B. K. All-inorganic perovskite nanocrystals with a stellar set of stabilities and their use in white light-emitting diodes. *ACS Appl. Mater. Interfaces* **2018**, *10* (43), 37267-37276.
- (192) Hong, X.; Ishihara, T.; Nurmikko, A. Dielectric confinement effect on excitons in PbI₄-based layered semiconductors. *Phys. Rev. B* **1992**, *45* (12), 6961.
- (193) Stoumpos, C. C.; Cao, D. H.; Clark, D. J.; Young, J.; Rondinelli, J. M.; Jang, J. I.; Hupp, J. T.; Kanatzidis, M. G. Ruddlesden–Popper hybrid lead iodide perovskite 2D homologous semiconductors. *Chem. Mater.* **2016**, *28* (8), 2852-2867.

- (194) Weidman, M. C.; Seitz, M.; Stranks, S. D.; Tisdale, W. A. Highly tunable colloidal perovskite nanoplatelets through variable cation, metal, and halide composition. *Acs Nano* **2016**, *10* (8), 7830-7839.
- (195) Tsai, H.; Nie, W.; Blancon, J.-C.; Stoumpos, C. C.; Asadpour, R.; Harutyunyan, B.; Neukirch, A. J.; Verduzco, R.; Crochet, J. J.; Tretiak, S. High-efficiency two-dimensional Ruddlesden–Popper perovskite solar cells. *Nature* **2016**, *536* (7616), 312-316.
- (196) Cherusseri, J.; Varma, S. J.; Pradhan, B.; Li, J.; Kumar, J.; Barrios, E.; Amin, M. Z.; Towers, A.; Gesquiere, A.; Thomas, J. Synthesis of air-stable two-dimensional nanoplatelets of Ruddlesden–Popper organic–inorganic hybrid perovskites. *Nanoscale* **2020**, *12* (18), 10072-10081.
- (197) Wang, N.; Cheng, L.; Ge, R.; Zhang, S.; Miao, Y.; Zou, W.; Yi, C.; Sun, Y.; Cao, Y.; Yang, R. Perovskite light-emitting diodes based on solution-processed self-organized multiple quantum wells. *Nat. Photonics* **2016**, *10* (11), 699-704.
- (198) Safdari, M.; Svensson, P. H.; Hoang, M. T.; Oh, I.; Kloo, L.; Gardner, J. M. Layered 2D alkyldiammonium lead iodide perovskites: synthesis, characterization, and use in solar cells. *J Mater Chem A* **2016**, *4* (40), 15638-15646.
- (199) Sichert, J. A.; Tong, Y.; Mutz, N.; Vollmer, M.; Fischer, S.; Milowska, K. Z.; García Cortadella, R.; Nickel, B.; Cardenas-Daw, C.; Stolarczyk, J. K. Quantum size effect in organometal halide perovskite nanoplatelets. *Nano Lett.* **2015**, *15* (10), 6521-6527.
- (200) Liang, Y.; Shang, Q.; Wei, Q.; Zhao, L.; Liu, Z.; Shi, J.; Zhong, Y.; Chen, J.; Gao, Y.; Li, M. Lasing from mechanically exfoliated 2D homologous Ruddlesden–Popper

perovskite engineered by inorganic layer thickness. *Advanced Materials* **2019**, *31* (39), 1903030.

(201) Parobek, D.; Roman, B. J.; Dong, Y.; Jin, H.; Lee, E.; Sheldon, M.; Son, D. H. Exciton-to-dopant energy transfer in Mn-doped cesium lead halide perovskite nanocrystals. *Nano Lett.* **2016**, *16* (12), 7376-7380.

(202) De, A.; Das, S.; Mondal, N.; Samanta, A. Highly luminescent violet-and blue-emitting stable perovskite nanocrystals. *ASC Mater. Lett.* **2019**, *1* (1), 116-122.

(203) Ahmed, T.; Seth, S.; Samanta, A. Boosting the photoluminescence of CsPbX₃ (X= Cl, Br, I) perovskite nanocrystals covering a wide wavelength range by postsynthetic treatment with tetrafluoroborate salts. *Chem. Mater.* **2018**, *30* (11), 3633-3637.

(204) De, A.; Mondal, N.; Samanta, A. Luminescence tuning and exciton dynamics of Mn-doped CsPbCl₃ nanocrystals. *Nanoscale* **2017**, *9* (43), 16722-16727.

(205) Guo, Z.; Wu, X.; Zhu, T.; Zhu, X.; Huang, L. Electron-phonon scattering in atomically thin 2D perovskites. *ACS nano* **2016**, *10* (11), 9992-9998.

(206) Chen, Y. N.; Sun, Y.; Peng, J. J.; Tang, J. H.; Zheng, K. B.; Liang, Z. Q. 2D Ruddlesden-Popper Perovskites for Optoelectronics. *Adv. Mater.* **2018**, *30* (2).

(207) Xing, G.; Wu, B.; Wu, X.; Li, M.; Du, B.; Wei, Q.; Guo, J.; Yeow, E. K.; Sum, T. C.; Huang, W. Transcending the slow bimolecular recombination in lead-halide perovskites for electroluminescence. *Nat Commun* **2017**, *8* (1), 1-9.

- (208) Wang, H. Z.; Fang, C.; Luo, H. M.; Li, D. H. Recent progress of the optoelectronic properties of 2D Ruddlesden-Popper perovskites. *J Semicond* **2019**, *40* (4).
- (209) Liao, Y.; Liu, H.; Zhou, W.; Yang, D.; Shang, Y.; Shi, Z.; Li, B.; Jiang, X.; Zhang, L.; Quan, L. N. Highly oriented low-dimensional tin halide perovskites with enhanced stability and photovoltaic performance. *J. Am. Chem. Soc.* **2017**, *139* (19), 6693-6699.
- (210) Stoumpos, C. C.; Soe, C. M. M.; Tsai, H.; Nie, W.; Blancon, J.-C.; Cao, D. H.; Liu, F.; Traoré, B.; Katan, C.; Even, J. High members of the 2D Ruddlesden-Popper halide perovskites: synthesis, optical properties, and solar cells of $(\text{CH}_3(\text{CH}_2)_3\text{NH}_3)_2(\text{CH}_3\text{NH}_3)_4\text{Pb}_5\text{I}_{16}$. *Chem* **2017**, *2* (3), 427-440.
- (211) Yuan, M.; Quan, L. N.; Comin, R.; Walters, G.; Sabatini, R.; Voznyy, O.; Hoogland, S.; Zhao, Y.; Beauregard, E. M.; Kanjanaboos, P. Perovskite energy funnels for efficient light-emitting diodes. *Nat. Nanotechnol.* **2016**, *11* (10), 872-877.
- (212) Yang, X.; Zhang, X.; Deng, J.; Chu, Z.; Jiang, Q.; Meng, J.; Wang, P.; Zhang, L.; Yin, Z.; You, J. Efficient green light-emitting diodes based on quasi-two-dimensional composition and phase engineered perovskite with surface passivation. *Nat Commun* **2018**, *9* (1), 1-8.
- (213) Yu, D.; Cao, F.; Gu, Y.; Han, Z.; Liu, J.; Huang, B.; Xu, X.; Zeng, H. Broadband and sensitive two-dimensional halide perovskite photodetector for full-spectrum underwater optical communication. *Nano Res* **2021**, *14* (4), 1210-1217.

- (214) Yu, D.; Cao, F.; Shen, Y.; Liu, X.; Zhu, Y.; Zeng, H. Dimensionality and interface engineering of 2d homologous perovskites for boosted charge-carrier transport and photodetection performances. *J. Phys. Chem. Lett.* **2017**, *8* (12), 2565-2572.
- (215) Pu, Y.; Cai, F.; Wang, D.; Wang, J.-X.; Chen, J.-F. Colloidal synthesis of semiconductor quantum dots toward large-scale production: a review. *Ind Eng Chem Res* **2018**, *57* (6), 1790-1802.
- (216) Tang, H.; He, Y.; Li, B.; Jung, J.; Zhang, C.; Liu, X.; Lin, Z. Continuous crafting of uniform colloidal nanocrystals using an inert-gas-driven microflow reactor. *Nanoscale* **2015**, *7* (21), 9731-9737.
- (217) Liang, X.; Baker, R. W.; Wu, K.; Deng, W.; Ferdani, D.; Kubiak, P. S.; Marken, F.; Torrente-Murciano, L.; Cameron, P. J. Continuous low temperature synthesis of MAPbX₃ perovskite nanocrystals in a flow reactor. *React. Chem. Eng.* **2018**, *3* (5), 640-644.
- (218) Ma, K.; Du, X.-Y.; Zhang, Y.-W.; Chen, S. In situ fabrication of halide perovskite nanocrystals embedded in polymer composites via microfluidic spinning microreactors. *J. Mater. Chem. C* **2017**, *5* (36), 9398-9404.
- (219) Lignos, I.; Stavrakis, S.; Nedelcu, G.; Protesescu, L.; deMello, A. J.; Kovalenko, M. V. Synthesis of cesium lead halide perovskite nanocrystals in a droplet-based microfluidic platform: fast parametric space mapping. *Nano Lett.* **2016**, *16* (3), 1869-1877.
- (220) Maceiczky, R. M.; Dümbgen, K.; Lignos, I.; Protesescu, L.; Kovalenko, M. V.; deMello, A. J. Microfluidic reactors provide preparative and mechanistic insights into the

synthesis of formamidinium lead halide perovskite nanocrystals. *Chem. Mater.* **2017**, *29* (19), 8433-8439.

(221) Zhang, C.; Luan, W.; Yin, Y.; Yang, F. PTFE-based microreactor system for the continuous synthesis of full-visible-spectrum emitting cesium lead halide perovskite nanocrystals. *Beilstein J Nanotechnol* **2017**, *8* (1), 2521-2529.

(222) Li, C.; Ding, B.; Zhang, L.; Song, K.; Tao, S. 3D-printed continuous flow reactor for high yield synthesis of $\text{CH}_3\text{NH}_3\text{PbX}_3$ (X= Br, I) nanocrystals. *J Mater Chem C* **2019**, *7* (30), 9167-9174.

(223) Gao, X.; Shen, X.; Xue, D.; Li, X.; Lu, P.; Lu, M.; Li, C.; William, W. Y.; Bai, X. Dual-color emitting Mn²⁺ ion doped (PEA)₂PbBr₄ perovskite towards white light-emitting diodes. *Mater. Chem. Front.* **2021**, *5* (2), 937-943.

(224) Zeng, S.; Shi, S.; Wang, S.; Xiao, Y. Mixed-ligand engineering of quasi-2D perovskites for efficient sky-blue light-emitting diodes. *J Mater Chem C* **2020**, *8* (4), 1319-1325.

(225) Zhang, L.; Jiang, T.; Yi, C.; Wu, J.; Liu, X.-K.; He, Y.; Miao, Y.; Zhang, Y.; Zhang, H.; Xie, X. Bright Free Exciton Electroluminescence from Mn-Doped Two-Dimensional Layered Perovskites. *J Phys Chem Lett* **2019**, *10* (11), 3171-3175.

(226) Yang, S.; Niu, W.; Wang, A. L.; Fan, Z.; Chen, B.; Tan, C.; Lu, Q.; Zhang, H. Ultrathin two-dimensional organic–inorganic hybrid perovskite nanosheets with bright, tunable photoluminescence and high stability. *Angew. Chem. Int. Ed.* **2017**, *56* (15), 4252-4255.

(227) Reichardt, C.; Welton, T. *Solvents and solvent effects in organic chemistry*, John Wiley & Sons: 2011.

(228) Zhang, F.; Huang, S.; Wang, P.; Chen, X.; Zhao, S.; Dong, Y.; Zhong, H. Colloidal synthesis of air-stable CH₃NH₃PbI₃ quantum dots by gaining chemical insight into the solvent effects. *Chem. Mater.* **2017**, *29* (8), 3793-3799.

(229) Tang, Y.; Yan, N.; Wang, Z.; Yuan, H.; Xin, Y.; Yin, H. Precursor solution volume-dependent ligand-assisted synthesis of CH₃NH₃PbBr₃ perovskite nanocrystals. *J. Alloys Compd.* **2019**, *773*, 227-233.

(230) Kim, B. J.; Kim, D. H.; Kwon, S. L.; Park, S. Y.; Li, Z.; Zhu, K.; Jung, H. S. Selective dissolution of halide perovskites as a step towards recycling solar cells. *Nat Commun* **2016**, *7* (1), 1-9.

(231) Jeevarathinam, D.; Gupta, A.; Pitchumani, B.; Mohan, R. Effect of gas and liquid flowrates on the size distribution of barium sulfate nanoparticles precipitated in a two phase flow capillary microreactor. *Chem Eng J* **2011**, *173* (2), 607-611.

(232) Shibuya, K.; Koshimizu, M.; Nishikido, F.; Saito, H.; Kishimoto, S. Poly [bis (phenethylammonium)[dibromidoplumbate (II)]-di- μ -bromido]. *Acta Crystallogr Sect E Struct Rep Online* **2009**, *65* (11), m1323-m1324.

(233) Poglitsch, A.; Weber, D. Dynamic disorder in methylammoniumtrihalogenoplumbates (II) observed by millimeter-wave spectroscopy. *The Journal of chemical physics* **1987**, *87* (11), 6373-6378.

- (234) Yaffe, O.; Guo, Y.; Tan, L. Z.; Egger, D. A.; Hull, T.; Stoumpos, C. C.; Zheng, F.; Heinz, T. F.; Kronik, L.; Kanatzidis, M. G. Local polar fluctuations in lead halide perovskite crystals. *Phys. Rev. Lett.* **2017**, *118* (13), 136001.
- (235) Mao, L.; Stoumpos, C. C.; Kanatzidis, M. G. Two-dimensional hybrid halide perovskites: principles and promises. *J. Am. Chem. Soc.* **2018**, *141* (3), 1171-1190.
- (236) Even, J.; Pedesseau, L.; Katan, C. Analysis of multivalley and multibandgap absorption and enhancement of free carriers related to exciton screening in hybrid perovskites. *J. Phys. Chem. C* **2014**, *118* (22), 11566-11572.
- (237) Liu, M.; Johnston, M. B.; Snaith, H. J. Efficient planar heterojunction perovskite solar cells by vapour deposition. *Nature* **2013**, *501* (7467), 395-398.
- (238) Noh, J. H.; Im, S. H.; Heo, J. H.; Mandal, T. N.; Seok, S. I. Chemical management for colorful, efficient, and stable inorganic–organic hybrid nanostructured solar cells. *Nano Lett.* **2013**, *13* (4), 1764-1769.
- (239) Law, C.; Miseikis, L.; Dimitrov, S.; Shakya-Tuladhar, P.; Li, X.; Barnes, P. R.; Durrant, J.; O'Regan, B. C. Performance and stability of lead perovskite/TiO₂, polymer/PCBM, and dye sensitized solar cells at light intensities up to 70 suns. *Adv. Mater.* **2014**, *26* (36), 6268-6273.
- (240) Tan, K. W.; Moore, D. T.; Saliba, M.; Sai, H.; Estroff, L. A.; Hanrath, T.; Snaith, H. J.; Wiesner, U. Thermally induced structural evolution and performance of mesoporous block copolymer-directed alumina perovskite solar cells. *ACS Nano* **2014**, *8* (5), 4730-4739.

- (241) Zhang, T.; Yang, M.; Zhao, Y.; Zhu, K. Controllable sequential deposition of planar CH₃NH₃PbI₃ perovskite films via adjustable volume expansion. *Nano Lett.* **2015**, *15* (6), 3959-3963.
- (242) Xie, F. X.; Zhang, D.; Su, H.; Ren, X.; Wong, K. S.; Grätzel, M.; Choy, W. C. Vacuum-assisted thermal annealing of CH₃NH₃PbI₃ for highly stable and efficient perovskite solar cells. *ACS Nano* **2015**, *9* (1), 639-646.
- (243) Deng, Y.; Peng, E.; Shao, Y.; Xiao, Z.; Dong, Q.; Huang, J. Scalable fabrication of efficient organolead trihalide perovskite solar cells with doctor-bladed active layers. *Energy Environ. Sci.* **2015**, *8* (5), 1544-1550.
- (244) Luo, D.; Su, R.; Zhang, W.; Gong, Q.; Zhu, R. Minimizing non-radiative recombination losses in perovskite solar cells. *Nat. Rev. Mater.* **2019**, *5*, 44.
- (245) Shamsi, J.; Dang, Z.; Bianchini, P.; Canale, C.; Di Stasio, F.; Brescia, R.; Prato, M.; Manna, L. Colloidal synthesis of quantum confined single crystal CsPbBr₃ nanosheets with lateral size control up to the micrometer range. *J. Am. Chem. Soc.* **2016**, *138* (23), 7240-7243.
- (246) Zhang, D.; Eaton, S. W.; Yu, Y.; Dou, L.; Yang, P. Solution-phase synthesis of cesium lead halide perovskite nanowires. *J. Am. Chem. Soc.* **2015**, *137* (29), 9230-9233.
- (247) Akkerman, Q. A.; D'Innocenzo, V.; Accornero, S.; Scarpellini, A.; Petrozza, A.; Prato, M.; Manna, L. Tuning the optical properties of cesium lead halide perovskite nanocrystals by anion exchange reactions. *J. Am. Chem. Soc.* **2015**, *137* (32), 10276-10281.

- (248) Eperon, G. E.; Beck, C. E.; Snaith, H. J. Cation exchange for thin film lead iodide perovskite interconversion. *Mater. Horiz.* **2016**, *3* (1), 63-71.
- (249) Grancini, G.; Nazeeruddin, M. K. Dimensional tailoring of hybrid perovskites for photovoltaics. *Nat. Rev. Mater.* **2019**, *4* (1), 4-22.
- (250) Cao, D. H.; Stoumpos, C. C.; Farha, O. K.; Hupp, J. T.; Kanatzidis, M. G. 2D homologous perovskites as light-absorbing materials for solar cell applications. *J. Am. Chem. Soc.* **2015**, *137* (24), 7843-7850.
- (251) Pan, A.; Wang, J.; Jurow, M. J.; Jia, M.; Liu, Y.; Wu, Y.; Zhang, Y.; He, L.; Liu, Y. General strategy for the preparation of stable luminous nanocomposite inks using chemically addressable CsPbX₃ perovskite nanocrystals. *Chem. Mater.* **2018**, *30* (8), 2771-2780.
- (252) Tong, J.; Wu, J.; Shen, W.; Zhang, Y.; Liu, Y.; Zhang, T.; Nie, S.; Deng, Z. Direct Hot-Injection Synthesis of Lead Halide Perovskite Nanocubes in Acrylic Monomers for Ultrastable and Bright Nanocrystal–Polymer Composite Films. *ACS Appl. Mater. Interfaces* **2019**, *11* (9), 9317-9325.
- (253) Yang, W.; Fei, L.; Gao, F.; Liu, W.; Xu, H.; Yang, L.; Liu, Y. Thermal polymerization synthesis of CsPbBr₃ perovskite-quantum-dots@ copolymer composite: Towards long-term stability and optical phosphor application. *Chem. Eng. J.* **2020**, *387*, 124180.

(254) Kolb, H. C.; Finn, M.; Sharpless, K. B. Click chemistry: diverse chemical function from a few good reactions. *Angewandte Chemie International Edition* **2001**, *40* (11), 2004-2021.

(255) Hoyle, C. E.; Lee, T. Y.; Roper, T. Thiol–enes: Chemistry of the past with promise for the future. *Journal of Polymer Science Part A: Polymer Chemistry* **2004**, *42* (21), 5301-5338.

(256) Griesbaum, K. Probleme und Möglichkeiten der radikalischen Addition von Thiolen an ungesättigte Verbindungen. *Angewandte Chemie* **1970**, *82* (7), 276-290.

(257) Smith, M. J.; Malak, S. T.; Jung, J.; Yoon, Y. J.; Lin, C. H.; Kim, S.; Lee, K. M.; Ma, R.; White, T. J.; Bunning, T. J. Robust, uniform, and highly emissive quantum dot–polymer films and patterns using thiol–ene chemistry. *ACS applied materials & interfaces* **2017**, *9* (20), 17435-17448.

(258) Du, K.-z.; Tu, Q.; Zhang, X.; Han, Q.; Liu, J.; Zauscher, S.; Mitzi, D. B. Two-dimensional lead (II) halide-based hybrid perovskites templated by acene alkylamines: crystal structures, optical properties, and piezoelectricity. *Inorganic chemistry* **2017**, *56* (15), 9291-9302.

(259) Aharon, S.; Wierzbowska, M.; Etgar, L. The effect of the alkylammonium ligand's length on organic–inorganic perovskite nanoparticles. *ACS Energy Letters* **2018**, *3* (6), 1387-1393.

(260) Byun, J.; Satheeshkumar, C.; Lee, G. Y.; Oh, J.; Jung, D. H.; Seo, M.; Kim, S. O. Air-Stable Perovskite Nanostructures with Dimensional Tunability by Polymerizable

Structure-Directing Ligands. *ACS Applied Materials & Interfaces* **2020**, *12* (28), 31770-31775.

(261) Proppe, A. H.; Wei, M.; Chen, B.; Quintero-Bermudez, R.; Kelley, S. O.; Sargent, E. H. Photochemically cross-linked quantum well ligands for 2D/3D perovskite photovoltaics with improved photovoltage and stability. *J Am Chem Soc* **2019**, *141* (36), 14180-14189.

(262) Zuo, Y.; Cao, J.; Feng, S. Sunlight-Induced Cross-Linked Luminescent Films Based on Polysiloxanes and d-Limonene via Thiol-ene “Click” Chemistry. *Advanced Functional Materials* **2015**, *25* (18), 2754-2762.

(263) Guo, M.; Huang, Y.; Cao, J.; Xu, Y.; Lu, S.; Feng, S. Luminescent and Robust Perovskite-Silicone Elastomers Prepared by Light Induced Thiol-Ene Reaction. *Macromolecular Rapid Communications* **2021**, *42* (5), 2000606.

(264) Wang, S.; Du, L.; Jin, Z.; Xin, Y.; Mattoussi, H. Enhanced Stabilization and Easy Phase Transfer of CsPbBr₃ Perovskite Quantum Dots Promoted by High Affinity Polyzwitterionic Ligands. *J. Am. Chem. Soc.* **2020**, *142* (29), 12669-12680.

(265) Jang, J.; Kim, Y.-H.; Park, S.; Yoo, D.; Cho, H.; Jang, J.; Jeong, H. B.; Lee, H.; Yuk, J. M.; Park, C. B.; Jeon, D. Y.; Kim, Y.-H.; Bae, B.-S.; Lee, T.-W. Extremely Stable Luminescent Crosslinked Perovskite Nanoparticles under Harsh Environments over 1.5 Years. *Adv. Mater.* **2021**, *33* (3), 2005255, DOI: <https://doi.org/10.1002/adma.202005255>.

(266) Wei, Y.; Deng, X.; Xie, Z.; Cai, X.; Liang, S.; Ma, P. a.; Hou, Z.; Cheng, Z.; Lin, J. Enhancing the stability of perovskite quantum dots by encapsulation in crosslinked

polystyrene beads via a swelling–shrinking strategy toward superior water resistance. *Adv. Funct. Mater.* **2017**, *27* (39), 1703535.

(267) Li, H.; Liu, X.; Ying, Q.; Wang, C.; Jia, W.; Xing, X.; Yin, L.; Lu, Z.; Zhang, K.; Pan, Y.; Shi, Z.; Huang, L.; Jia, D. Self-Assembly of Perovskite CsPbBr₃ Quantum Dots Driven by a Photo-Induced Alkynyl Homocoupling Reaction. *Angew. Chem. Int. Ed.* **2020**, *59* (39), 17207-17213, DOI: <https://doi.org/10.1002/anie.202004947>.

(268) He, H.; Feng, M.; Chen, Q.; Zhang, X.; Zhan, H. Light-Induced Reversible Self-Assembly of Gold Nanoparticles Surface-Immobilized with Coumarin Ligands. *Angewandte Chemie International Edition* **2016**, *55* (3), 936-940.

(269) Huang, J.; Su, J.-H.; Tian, H. The development of anthracene derivatives for organic light-emitting diodes. *Journal of Materials Chemistry* **2012**, *22* (22), 10977-10989.

(270) Du, C.; Ye, S.; Liu, Y.; Guo, Y.; Wu, T.; Liu, H.; Zheng, J.; Cheng, C.; Zhu, M.; Yu, G. Fused-seven-ring anthracene derivative with two sulfur bridges for high performance red organic light-emitting diodes. *Chemical communications* **2010**, *46* (45), 8573-8575.

(271) Liang, S.; Zhang, M.; Biesold, G. M.; Choi, W.; He, Y.; Li, Z.; Shen, D.; Lin, Z. Recent Advances in Synthesis, Properties, and Applications of Metal Halide Perovskite Nanocrystals/Polymer Nanocomposites. *Adv. Mater.* **2021**, *33* (50), 2005888.

(272) Shamsi, J.; Urban, A. S.; Imran, M.; De Trizio, L.; Manna, L. Metal halide perovskite nanocrystals: synthesis, post-synthesis modifications, and their optical properties. *Chem. Rev.* **2019**, *119* (5), 3296-3348.

(273) Luo, Z.; Marson, D.; Ong, Q. K.; Loiudice, A.; Kohlbrecher, J.; Radulescu, A.; Krause-Heuer, A.; Darwish, T.; Balog, S.; Buonsanti, R. Quantitative 3D determination of self-assembled structures on nanoparticles using small angle neutron scattering. *Nat. Commun.* **2018**, *9* (1), 1-10.

(274) Yarita, N.; Tahara, H.; Ihara, T.; Kawawaki, T.; Sato, R.; Saruyama, M.; Teranishi, T.; Kanemitsu, Y. Dynamics of charged excitons and biexcitons in CsPbBr₃ perovskite nanocrystals revealed by femtosecond transient-absorption and single-dot luminescence spectroscopy. *J. Phys. Chem. Lett.* **2017**, *8* (7), 1413-1418.

(275) Yettapu, G. R.; Talukdar, D.; Sarkar, S.; Swarnkar, A.; Nag, A.; Ghosh, P.; Mandal, P. Terahertz conductivity within colloidal CsPbBr₃ perovskite nanocrystals: remarkably high carrier mobilities and large diffusion lengths. *Nano Lett.* **2016**, *16* (8), 4838-4848.